AD A066093
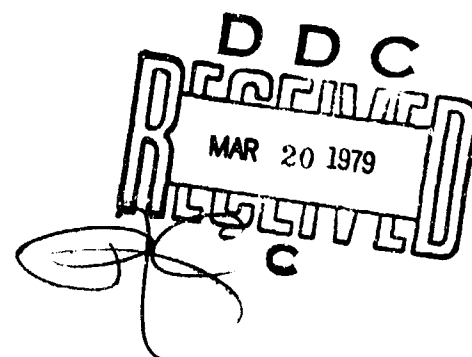
USARTL-TR-79-2

LEVEL

ENGINE ROTOR DYNAMICS, SYNCHRONOUS AND NONSYNCHRONOUS WHIRL CONTROL

Ronald A. Marmol
PRATT & WHITNEY AIRCRAFT GROUP
Government Products Division
P.O. Box 2691
West Palm Beach, Fla. 33402

February 1979

Final Report

DDC
MAR 20 1979
C

Approved for public release;
distribution unlimited.

Prepared for

APPLIED TECHNOLOGY LABORATORY
U. S. ARMY RESEARCH AND TECHNOLOGY LABORATORIES (AVRADCOM)
Fort Eustis, Va. 23604

APPLIED TECHNOLOGY LABORATORY POSITION STATEMENT

With the trend toward higher shaft speeds to increase airflow and power output without increasing physical size, there have developed rotor dynamic requirements peculiar to the class of small turboshaft engines being developed for the Army; e.g., the short blades require extremely small tip-to-housing clearances to maintain high aerodynamic efficiency. This in turn requires very small rotor shaft excursions, to avoid blade-housing interferences, which is incompatible with low dynamic bearing loads at high speeds. As shaft speeds increase it becomes more difficult to keep critical speeds (synchronous whirl) out of the operating range. In order to operate safely through or near the flexural critical speeds, a rotor shaft must either be well balanced, highly damped, or both. Nonsynchronous whirl induced by internal friction is probably the most common type of self-excited whirl in turboshaft engines. The destabilizing forces generated by shaft splines appear to be one of the most common causes of this type of response.

This report provides the details of a program designed to improve the analytical techniques currently available to Government and industry for the design and analysis of rotor systems incorporating squeeze film bearing dampers and flexible bearing supports to control synchronous and nonsynchronous whirl. One product is a squeeze film bearing damper analysis, "Damper Analysis by Numerical Differentiation and Integration" (DANDI), capable of predicting pressures and response of all known damper configurations under normal and abusive unbalance conditions and under nonsynchronous response conditions; another is a spline coupling analysis program that predicts the destabilizing forces of commonly used spline configurations with and without lubrication; and a third is validation testing results showing that existing beam formulas for calculating the stiffness of flexible bearing supports have satisfactory accuracy for estimating support performance as part of an overall rotor system dynamic analysis.

Mr. Allen C. Royal, Propulsion Technical Area, Aeronautical Technology Division, served as Project Engineer for this project.

SECURITY CLASSIFICATION OF THIS PAGE (When Data Entered)

REPORT DOCUMENTATION PAGE	READ INSTRUCTIONS BEFORE COMPLETING FORM

1. REPORT NUMBER	2. GOVT ACCESSION NO.	3. RECIPIENT'S CATALOG NUMBER
USARTL-TR-79-2		

4. TITLE (and Subtitle)	5. TYPE OF REPORT & PERIOD COVERED
ENGINE ROTOR DYNAMICS, SYNCHRONOUS AND NONSYNCHRONOUS WHIRL CONTROL.	Final Technical Report
	6. PERFORMING ORG. REPORT NUMBER
	FR-10632

7. AUTHOR(s)	8. CONTRACT OR GRANT NUMBER(s)
Ronald A. Marmol	Contract DAAJ02-76-C-0011

9. PERFORMING ORGANIZATION NAME AND ADDRESS	10. PROGRAM ELEMENT, PROJECT, TASK AREA & WORK UNIT NUMBERS
Pratt & Whitney Aircraft Group Government Products Division P.O. Box 2691 West Palm Beach, Florida 33402	62209A 1F262209 AH76 00 144 EK

11. CONTROLLING OFFICE NAME AND ADDRESS	12. REPORT DATE
Applied Technology Laboratory U. S. Army Research and Technology Laboratories (AVRADCOM) Fort Eustis, VA 23604	February 1979
	13. NUMBER OF PAGES
	148

14. MONITORING AGENCY NAME & ADDRESS(if different from Controlling Office)	15. SECURITY CLASS. (of this report)
1F262209AH76	UNCLASSIFIED
	15a. DECLASSIFICATION/DOWNGRADING SCHEDULE

16. DISTRIBUTION STATEMENT (of this Report)

Approved for public release; distribution unlimited.

17. DISTRIBUTION STATEMENT (of the abstract entered in Block 20, if different from Report)

18. SUPPLEMENTARY NOTES

19. KEY WORDS (Continue on reverse side if necessary and identify by block number)

Rotor Dynamics	Blade Loss Response	Supercritical Shaft
Squeeze Film	Spline Coupling	Flexible Supports
Damper	Stability	Nonsynchronous Whirl
Critical Speed	Subcritical Shaft	Synchronous Whirl

20. ABSTRACT (Continue on reverse side if necessary and identify by block number)

A combined analytical and test program has been performed to develop a method of designing high-speed power turbine rotors to (1) minimize rotor-induced dynamic loads under normal operating conditions, (2) minimize rotor tip-to-shroud clearance to maintain high flow-path efficiency, and (3) minimize rotor deflections due to sudden abusive imbalance loads associated with blade loss. A design/prediction system was established for both synchronous and nonsynchronous rotor whirl and the best compromise design for a rotor subjected to these excitations.

DD FORM 1473   EDITION OF 1 NOV 65 IS OBSOLETE

SECURITY CLASSIFICATION OF THIS PAGE (When Data Entered)

Two mathematical models were developed in the course of the program. First, a squeeze film damper model and subsequent computer program were developed to quantify the effects of end-seal leakage and inlet feedback on damper performance. Secondly, a spline coupling friction mathematical model and computer program were developed to predict the destabilizing forces which excite rotor nonsynchronous whirl.

To verify the accuracy of the analytical models developed in the program and other existing rotor dynamic models, a comprehensive test program was run. This program included: (1) a high speed squeeze film damper test rig, (2) bearing flexible support testing, (3) a synchronous response rotor rig, and (4) a nonsynchronous response rotor rig. Using the results of the analytical models and experimental tests, a method of design optimization was developed to obtain the best trade-off between all the rotor design variables considered in this program.

PREFACE

This report covers the development of a design/prediction system for optimizing the design of high-speed turboshaft engines. The 36-month Engine Rotor Dynamics Program was performed under Contract DAAJ02-76-C-0011 with the Applied Technology Laboratory, U. S. Army Research and Technology Laboratories (AVRADCOM), Ft. Eustis, Virginia. The program was performed under the technical cognizance of Mr. A. Royal of the Propulsion Group, Technology Applications Division, Applied Technology Laboratory. The results of the program were culminated in a method of design optimization for power turbine rotor dynamics.

The program was conducted by United Technologies Corporation, Pratt & Whitney Aircraft Group Government Products Division, West Palm Beach, Florida with the subcontracted assistance of Pratt & Whitney Aircraft of Canada LTD., Longueuil, Quebec; Mechanical Technology Incorporated, Latham, New York; and Dr. J. M. Vance, formerly Associate Professor of the Department of Mechanical Engineering, University of Florida, Gainesville, Florida.

TABLE OF CONTENTS

LIST OF ILLUSTRATIONS

LIST OF ILLUSTRATIONS (Continued)

LIST OF ILLUSTRATIONS (Continued)

LIST OF ILLUSTRATIONS (Continued)

LIST OF TABLES

SECTION I

INTRODUCTION

Recent trends in aircraft gas turbine engine design have been directed toward lightweight, flexible rotor and case systems in the interest of increased horsepower/thrust-to-weight ratios. Without precise control of rotor and case system dynamic deflections, severe performance deterioration will occur as a result of blade tip-to-shroud rubs. As much as 1% loss in efficiency due to a surge-induced rotor tip rub can occur in a multistage compressor. More than 3% engine performance deterioration can result from a combination of severe compressor and turbine rotor tip-to-shroud rubs.

The rotor system dynamic design analyses must also address sudden, large-scale rotor imbalance. For example, the loss of an engine and possibly a catastrophic loss of an aircraft could occur as the result of inadvertent blade loss, if the rotor/support system is too sensitive to imbalance.

The Applied Technology Laboratory recognized the requirement for improved analytical design and prediction techniques in the area of engine rotor dynamics and contracted with Pratt & Whitney Aircraft to conduct this comprehensive development program. The improvement of engine rotor dynamics design tools in this program has three major objectives: (1) to minimize rotor-induced dynamic loads under normal operating conditions; (2) to minimize achievable rotor tip-to-shroud clearance to maintain high flowpath efficiency; and (3) to minimize rotor deflections due to sudden abnormal imbalance loads associated with blade loss and/or engine surge.

The 36-month program is organized into 10 tasks (Figure 1). The first seven tasks are concerned with establishing a design/prediction system for synchronous whirl situations. The last three tasks are directed toward nonsynchronous whirl and the best compromise design for a rotor system subjected to both types of excitation.

Tasks I, II, and III established the operating characteristics of an oil film damper. Task IV established the design characteristics of flexible bearing supports. The combination of oil film and support structure characteristics provided the basis for a design/prediction system for oil-damped rotor systems. Task I, Analytical Prediction, consisted of the formulation of an analytical model of a squeeze film damper. This model included the Tondl and the Lund coefficients. A viscous damper rig, which has the capability to provide all the experimental data needed to determine the Tondl and Lund coefficients, was designed in Task II, Conceptual and Detail Design. In Task III, Fabrication and Test, bearing damper pressures and shaft motion were measured over a range of design parameters that permitted data comparison with current bearing theories. These data fully characterized viscous damper behavior under synchronous loading conditions. In Task IV, establishment of the operating characteristics (static and dynamic stiffness and structural damping) of three different types of bearing supports was accomplished.

11

Task I - Analytical Prediction
- Formulate Analytical Model of Squeeze Film Damper

Task II - Conceptual and Detail Design
- Modify Existing Damper Rig to Provide Data Needed for Analytical Model

Task III - Fabrication and Test
- Modify Damper Rig
- Generate Required Data
- Analyze Data

Task IV - Support Stiffness
- Measure Static and Dynamic Stiffness of 3 Types of Bearing Supports, Over Range of Support Design Variables. Modify Stiffness Analysis as Required

Task V - Analytical Prediction
- Use Task I-IV Results to Predict Dynamic Bearing Forces and Rotor-Shroud Deflection as Function of Six Variables. For Subcritical and Supercritical Operation

Task VI - Measurement Capability
- Modify Existing Rig to Provide Optimum Damper-Support Configuration for Synchronous Whirl

Task VII - Fabrication and Test
- Fabricate Synchronous Rig
- Measure Bearing Forces, Rotor-Shroud Deflections
- Refine Analysis as Required

Task VIII - Nonsynchronous Whirl
- Develop Spline Model
- Modify Existing Rig to Simulate Power Turbine Shaft Characteristics

Task IX - Fabrication and Test
- Fabricate Nonsynchronous Rig
- Generate Test Data for 3 Spline Parameters, Pertinent Damper Parameters
- Determine Optimum Oil Damper - Flexible Support for Nonsynchronous Whirl

Task X - Optimization
- Conduct Trade Study to Determine Best Compromise Damper-Support Design for Power Turbine Shaft Systems

Viscous Damper Characterization

Bearing Support Characterization

Synchronous Whirl

Nonsynchronous Whirl

Design Analysis Formulation (Synchronous)

Design Analysis Verification (Synchronous)

Design Analysis Formulation (Nonsynchronous)

Figure 1. Rotor Dynamics Program Overview

The validity of this square film damper design system was demonstrated in an existing controlled test rig in Tasks V, VI, and VII, which involved the prediction and subsequent measurement of bearing forces and rotor-to-shroud deflection. In Task V, Analytical Prediction, the Task I design system was used to define an optimum damped bearing configuration. Predictions were made for dynamic bearing forces and rotor-to-shroud displacement as a function of six variables: (1) rotor unbalance, (2) rotor shaft speed, (3) rotor-to-shroud clearance, (4) bumper clearance, (5) bearing damper support flexibility, and (6) the most important oil film variables established during the viscous damper characterization. These predictions were made for both subcritical and supercritical shaft speeds. In Task VI, Measurement Capability, an experimental rig was designed to provide the capability to simultaneously measure dynamic bearing loads and rotor/shroud relative deflections. The experimental rig was fabricated and tested in Task VII, Fabrication and Test, using the capability designed in Task VI to measure rotor dynamic response as a function of the variables specified in Task V. The test results show that rotor/shroud deflection can be minimized by either a small clearance or large clearance damper. However, the small clearance damper produces high bearing loads; therefore the large clearance damper and bumper combination showed the best overall dynamic performance. The test program also demonstrated the survivability of a supercritical rotor by simulating a blade loss at a speed 20% above the shaft bending critical speed and decelerating back again through the critical speed with the abusive blade loss imbalance without damage to the rig.

In Tasks VIII and IX the effectiveness of the optimum damper system in suppressing nonsynchronous excitations such as those typically encountered in power turbine rotor systems of turboshaft engines was determined. Task VIII, Nonsynchronous Whirl, dealt with the problem of predicting spline-coupling-induced nonsynchronous rotor whirl and the design of a test rig which had the capability to experimentally demonstrate and measure nonsynchronous whirl and the threshold speed of instability. A rotor rig that would demonstrate nonsynchronous whirl as a function of the following four variables was fabricated and tested under Task IX, Fabrication and Test: (1) spline type, (2) spline clearance fit, (3) spline lubricant supply, and (4) damper lubricant supply. The test results showed that squeeze film damping and spline lubrication act to suppress spline-coupling-induced rotor instability. On all occasions the test rig could be stabilized by simply lubricating the spline teeth contact surfaces.

In the final task, Task X, a trade study was conducted to determine the best compromise damper support design for power turbine shafts, considering both synchronous and non-synchronous whirl. Using the results of tasks VI through IX, a method of design optimization for the best trade-off between all the rotor design variables considered in this program was developed. Because of the vast number of mission requirements for gas turbine engines, each engine must be evaluated by the criteria dictated by its individual mission. However, a fast iterative procedure has been developed which will allow rotor dynamic optimization in the early stages of engine development.

SECTION II

VISCOUS DAMPER CHARACTERIZATION (TASKS I, II, AND III)

A. GENERAL DISCUSSION

A mathematical model for squeeze film dampers was developed, and the solution results were compared with data from four different test rigs. A special feature of the analysis was the treatment of several different types of end seals and inlets, with inlet feedback included. A finite difference method was used to solve the Reynolds equation, with a banded matrix inversion routine. The test data were taken from a high-speed free-rotor rig and from three previously tested controlled-orbit rigs.

Squeeze film dampers have been used for many years to minimize rotor vibrations in gas turbine engines. The success rate of these dampers has been sporadic, primarily due to the lack of adequate analytical modeling. Until recently, damper analyses were based on a journal bearing theory that restricted the damper to centralized circular whirl orbits and simplified end flow conditions. The damper model presented in this report treats noncircular orbits, end seal effects, and inlet feedback effects.

In 1886 Reynolds derived his famous lubrication equation based on the theory that the resultant pressure profile was due to hydrodynamic action in the fluid and was dependent upon the viscosity of the lubricant being used. The Reynolds equation was derived from Navier-Stokes general flow equations with assumptions such as thin film, laminar flow, no surface slippage, etc. Several authors such as Hori (Reference 1) and Tondl (Reference 2) analytically solved the Reynolds equation by assuming a "long bearing" (no lubricant end flow) for studying journal bearing performance. The film circumferential end conditions imposed by these authors apply to journal bearings and also to dampers with centralized circular whirl orbits.

The computer program described in this report considers general damper orbits including nonzero radial velocities and the effects of lubricant flow out of the end seals and through the inlet. Piston ring and O-ring type end seals are modeled to create continuity in flow throughout the damper, and the resulting equations are written in finite difference form. Multiple hole and circumferential groove inlets are modeled, and the total pressure distribution is solved simultaneously by use of a banded matrix inversion technique.

The analytical model was verified by examining the pressure data measured in four squeeze film damper rigs with speeds ranging to 50,000 rpm. Three of the rigs were previously reported in References 3, 4, and 5. These three rigs were run at low speeds, to 3,000 rpm, and had controlled orbits that precisely defined the motion of the damper. The high speed data to be described herein were measured on the fourth rig in which the damper had unconstrained orbits (free rotor). The four rigs have a wide variety of damper sizes and inlet and seal configurations.

1 Hori, Y., "A Theory of Oil Whip," Journal of Applied Mechanics, Trans. ASME, June 1959.

2 Tondl, A.,"Some Problems in Rotor Dynamics,"Chapman and Hall Limited, London, England, 1965, pp. 122-130.

3 Feder, E., Bansal P. N. and Blanco, A., "Investigation of Squeeze Film Damper Forces Produced by Circular Centered Orbits," presented at the Gas Turbine Conference, Philadelphia, Pa., March 27-31, 1977, ASME Paper No. 77-GT-27

4 Vance, J. M., and Kirton, A. J. "Preliminary Investigation of the Dynamic Force Response Coefficients for Squeeze Film Bearing Dampers," U.S. Army Research Office, Grant Number DAHC04-74-6-0048, November 1974.

5 Jones, M. G., "An Experimental Investigation of Squeeze Film Hydrodynamics," Report No. R. 320, National Gas Turbine Establishment, Ministry of Defense (England), January 1973.

B. ANALYTICAL MODEL

1. Description

The problem is that of calculating the distribution of film pressure in a squeeze film bearing damper, given the journal position and velocity.

The approach is to calculate the elements of the matrix and right side vector that result from a finite difference formulation of the Reynolds equation and the boundary conditions. The matrix and right side vector define the set of algebraic equations linear in the pressures at the nodes of the finite difference grid.

A special feature of the model is the treatment of several realistic boundary conditions describing the inlet flow through any number of holes or a groove, and the leakage flow through several kinds of end seals presently used in dampers for turbomachinery. The types of end seals treated are:

Piston ring
Radial O-ring (around OD of journal at the ends)
Side or axial O-ring (against the end face of the journal)
No end seal.

Since the finite difference method of solution requires no simplifying assumptions, the damper geometry is not restricted; i.e., "short bearing" or "long bearing" assumptions are not required.

The solution efficiency is maintained by using a banded matrix inversion routine (Reference 6) to solve the system of simultaneous pressure equations resulting from the finite difference breakups. The resulting damper forces are calculated by numerically integrating the pressure profile.

2. Method of Solution

The squeeze film damper is considered to be an oil film journal bearing with a nonrotating journal. Thus, all of the surface velocity at the film boundary is the result of shaft translation (radial and tangential) allowed by the damper clearance. Classical hydrodynamic bearing theory shows that the distribution of film pressure is given by the solution of the Reynolds equation, subject to the appropriate boundary conditions.

Using the notation and geometry from Figures 2 and 3, the Reynolds equation is

$$\frac{1}{6\mu} \left[\frac{\partial}{\partial X} \left(h^3 \frac{\partial p}{\partial X} \right) + \frac{\partial}{\partial Z} \left(h^3 \frac{\partial p}{\partial Z} \right) \right]$$

$$= h \frac{\partial U_1}{\partial X} - U_1 \frac{\partial h}{\partial X} + 2 U_2. \tag{1}$$

---

6   King, H. H., "A Poisson Equation Solver for Rectangular or Annular Regions," International Journal for Numerical Methods in Engineering, Vol. 10, 1976, pp. 799-807.

$$R_b = \overline{BQ}$$
$$R_j = \overline{JP}$$

$$(R_b-h)^2 = e^2 + R_j^2 - 2e\,R_j\cos\theta$$

$$h = C + R_j\left[1 - \sqrt{1 + \left(\frac{e}{R_j}\right)^2 - 2\frac{e}{R_j}\cos\theta}\right]$$

Figure 3. Bearing Geometry

Figure 2. Bearing Notation and Coordinate System
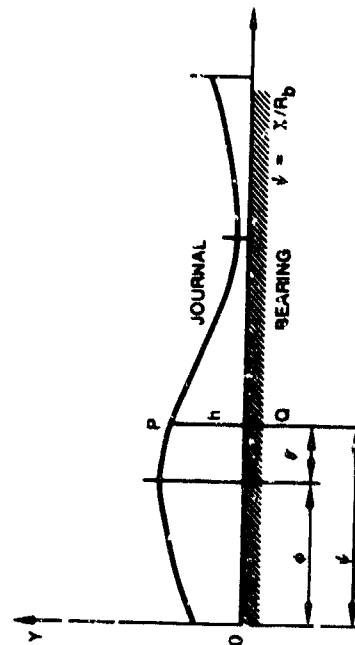
16
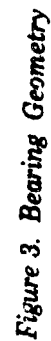
Equation (1) is taken from equation (83) of Reference 7, with the velocity U_2 taken as zero (at the stationary bearing surface). The equation is made dimensionless by substitution of the following dimensionless parameters:

$$\psi = \frac{X}{R_b} \ , \ Z = \frac{Z}{R_b}$$

$$P = \frac{pC^2}{6\mu \ R_b^2 \ \omega} \ , \ H = \frac{h}{C}$$

$$U_1 = \frac{U_1}{\omega R_b} \ , \ U_2 = \frac{U_2}{\omega C}$$

The derivatives of H, H^2, and U_1 with respect to ψ are evaluated in functional form. Equation (1) then becomes

$$\frac{\partial^2 P}{\partial Z^2} + \frac{\partial^2 P}{\partial \psi^2} + f_1 \ (\psi, \ \phi, \ \epsilon) \ \frac{\partial P}{\partial \psi} = f_3 \ (\psi, \ \phi, \ \epsilon) \ \frac{d\phi}{dT} + f_4 \ (\psi, \ \phi, \ \epsilon)\frac{d\epsilon}{dT} \ , \tag{2}$$

where

$$f_1 = \frac{3}{H} \left\{ - \epsilon \sin (\psi - \phi) + \left(\frac{C}{R_j} \right) \ \epsilon^2 \ \frac{\sin (\psi - \phi) \ \cos (\psi - \phi)}{\cos \alpha} \right\} \ ,$$

$$f_3 = \frac{1}{H^3} \left\{ \epsilon \left[2 + \frac{C}{R_b} \ H \right] \sin (\psi - \phi) \right.$$

$$- \epsilon^2 \ \frac{C}{R_b} \sin (\psi - \phi) \ \cos (\psi - \phi)$$

$$\left. + \epsilon^3 \ \frac{C}{R_b} \left(\frac{C}{R_j} \right)^2 \ \frac{\sin (\psi - \phi) \ \cos (\psi - \phi)}{\cos \alpha} \right\} \ ,$$

$$f_4 = \frac{1}{H^3} \left\{ \left[2 + \frac{C}{R_b} \ H \right] \cos (\psi - \phi) \right.$$

$$+ \epsilon \ \frac{C}{R_b} \sin^2 (\psi - \phi)$$

$$\left. - \epsilon^4 \left[\frac{C}{R_b} \left(\frac{C}{R_j} \right)^2 \ \frac{1}{\cos \alpha} \right] \sin^2 (\psi - \phi) \cos (\psi - \phi) \right\} \ ,$$

$$H = \frac{h}{C} = 1 + \epsilon \cos(\psi - \phi) + \frac{R_j}{C} [1 - \cos \alpha] \ ,$$

$$\cos \alpha = \sqrt{ 1 - \left(\frac{C}{R_j} \right)^2 \ \epsilon^2 \sin^2 (\psi - \phi) }$$

---

7 Trumpler, P. R."Design of Film Bearings," MacMillan Co., New York, 1966, p. 30.

and

$$T = \omega t, \quad t = \text{time (sec)}.$$

The damper pressure distribution is the solution to equation (2), subject to the boundary conditions as determined by the inlet and by the seals.

3. End Seal and Inlet Boundary Conditions

Piston Ring Seal. Figure 4 shows the configuration of this seal.
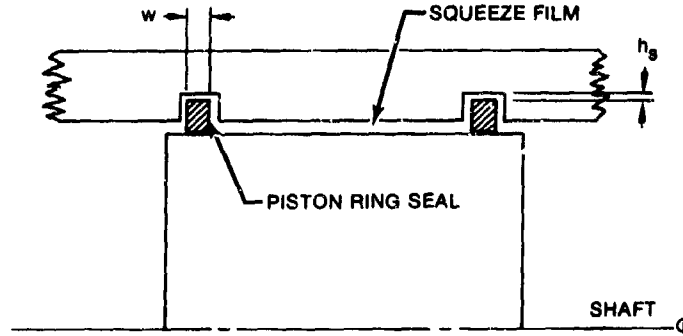
Figure 4. Piston Ring Seal Configuration

The axial flow balance across any unit circumferential length around the seal is given by

$$-\frac{h^3}{12\mu} \frac{\partial p}{\partial Z} = C_p \frac{(p-p_e)h_s^3}{12\mu w} \quad \text{in.}^3/\text{sec/in.} \tag{3}$$

where p and $\partial p/\partial Z$ are the pressure gradient at the inside face of the seal (any X, Z = L); p_e is the pressure outside the seal.

In dimensionless form, this boundary condition is written

$$-\frac{\partial P}{\partial Z} \left(\psi, \frac{L}{R_b} \right) = C_p' \left[P \left(\psi, \frac{L}{R_b} \right) - P_e \right].$$

where

$$C_p' = C_p \frac{R_b h_s^3}{w h^3} \tag{4}$$

Note that C_p' varies around the seal with $1/h^3$.

Radial O-ring seal. Figure 5 shows this seal configuration.

Since the O-ring is flexible, it deforms in response to the local film pressure. A traveling wave of axial deflection follows the rotating pressure distribution and accommodates axial flow from the film, even if no leakage occurs (Figure 6).

18
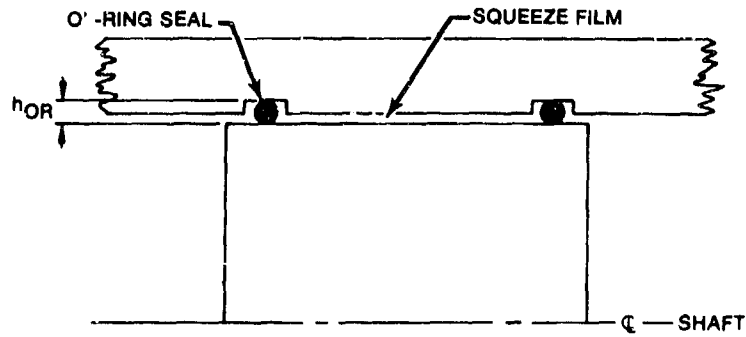
Figure 5. Radial O-Ring Seal Configuration
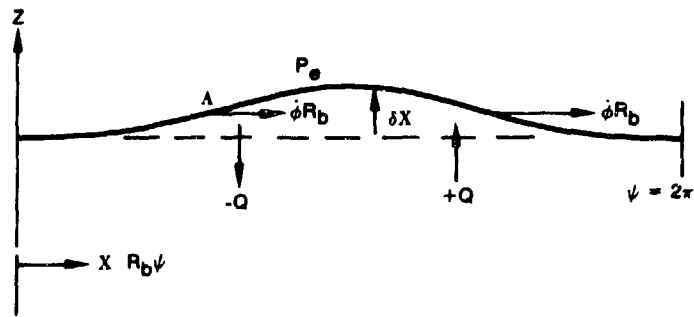
(A) TRAVELLING WAVE
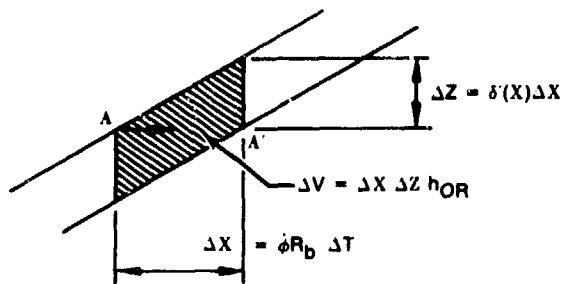
$$\Delta Q = \frac{\Delta V}{\Delta t} = h_{OR} \, \delta'(X) \, \dot{\phi} R_b \, \Delta X$$

$$\delta(X) = K_{OR} \, p(X)$$

$$\delta'(X) = K_{OR} \frac{\partial p}{\partial X}$$

(B) VOLUME DISPLACED AT POINT A IN TIME ΔT

Figure 6. Traveling Wave Around Radial O-Ring

19

Including leakage, the axial flow balance across any unit circumferential length around the seal is

$$- h_{OR} \, K_{OR} \, \dot{\phi} \, R_b \, \frac{\partial p}{\partial X} \, (X, L) - \frac{h^3}{12\mu} \, \frac{\partial p}{\partial Z} \, (X, L)$$

$$= C_{OR} \, [p \, (X, L) - p_e] \, . \tag{5}$$

In dimensionless form, this boundary condition is written

$$- C_R' \left[P \left(\psi, \frac{L}{R_b} \right) - P_e \right] - K_R' \frac{\partial P}{\partial \psi} \left(\psi, \frac{L}{R_b} \right) \tag{6}$$

$$- \frac{\partial P}{\partial Z} \left(\psi, \frac{L}{R_b} \right) = 0 \, ,$$

where

$$C_R' = \frac{12\mu \, R_b}{h^3} \, C_{OR} \, ,$$

and

$$K_R' = \frac{12\mu \, R_b \, H_{OR} \, \dot{\phi}}{h^3} \, K_{OR}$$

Note that C_R' and K_R' vary around the seal with $1/h^3$ and that K_R' varies with the instantaneous orbit velocity $\dot{\phi}$.

Side O-ring seal. Figure 7 shows this type of seal. Notice that the dimensions h_2 and "a" form a circumferential cavity at the end $(Z = L)$ of the film.
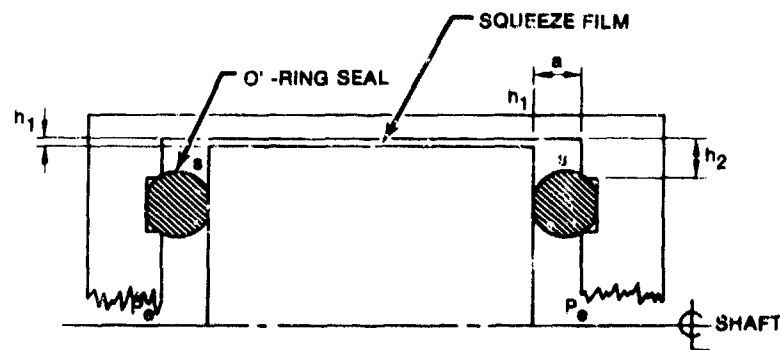
Figure 7. Side O-Ring Seal Configuration

This boundary condition requires that the flow out of the cavity (across the O-ring) must equal the integral around the circumference of the axial flow from the film at $Z = L$. Since $h_s \gg h_1$, there is no circumferential pressure gradient around the cavity. The flow balance is

$$- \int_0^{2\pi} \frac{h^3}{12\mu} \frac{\partial p}{\partial Z} (X, L) R_b \, dX = C_c [p_c - p_e], \tag{7}$$

with

$$p (X, L) = p_c ,$$

where p and $\partial p/\partial Z$ are the pressure and axial pressure gradient at

$$Z = L, \left(\frac{\partial p}{\partial X} = 0 \text{ at } Z = L \right).$$

In dimensionless form, this boundary condition becomes

$$- \int_0^{2\pi} H^3 \frac{\partial P}{\partial Z} \left(\psi, \frac{L}{R_b} \right) d\psi = C_c' [P_c - P_e] \tag{8}$$

with

$$P \left(\psi, \frac{L}{R_b} \right) = P_c, \text{ all } \psi,$$

where

$$C_c' = \frac{12\mu}{c^3} C_c .$$

No end seal. If the damper end is open, the boundary condition is

$$p (X, L) = p_e . \tag{9}$$

In dimensionless form, this becomes

$$P \left(\phi, \frac{L}{R_b} \right) = P_e . \tag{10}$$

Single hole with backflow.

The flow balance is

$$Q_1 = Q_2 \text{ in}^3/\text{sec},$$

where

Q_i = flow into film from inlet,
Q_a = flow away from inlet location.

In terms of pressures and gradients, this boundary condition is

$$Q_i = C_i \left[p_s - p\left(X_i, Z_i \right) \right]$$

$$= Q_a = \frac{h^3}{12\mu} \left[\frac{\partial p}{\partial X} \left(X_i - \frac{d_i}{2}, Z_i \right) \right.$$

$$\left. - \frac{\partial p}{\partial Z} \left(X_i + \frac{d_i}{2}, Z_i \right) \right] dZ$$

$$+ \frac{h^3}{12\mu} \left[\frac{\partial p}{\partial Z} \left(X_i, Z_i - \frac{d_i}{2} \right) \right.$$

$$\left. - \frac{\partial p}{\partial Z} \left(X_i, Z_i + \frac{d_i}{2} \right) \right] dZ \tag{11}$$

In dimensionless form, with $d_i < \Delta$, this becomes

$$\frac{\partial P}{\partial \psi} \left(\psi_i -, \hat{Z}_i \right) \bar{\Delta}_z - \frac{\partial P}{\partial \psi} \left(\psi_i +, \hat{Z}_i \right) \bar{\Delta}_z$$

$$+ \frac{\partial P}{\partial \hat{Z}} \left(\psi_i, \hat{Z}_i - \right) \bar{\Delta}_\psi - \frac{\partial P}{\partial \hat{Z}} \left(\psi_i, \hat{Z}_i + \right) \bar{\Delta}_\psi$$

$$= C_i' \left[P_s - P(\psi_i, \hat{Z}_i) \right] \tag{12}$$

where

$$C_i' = \frac{12\mu}{h^3} C_i \,,$$

Equation (12) applies at each inlet hole location.

Circumferential inlet groove (360°). The boundary condition is

$$p\left(X, Z_i \right) = p_s \,. \tag{13}$$

In dimensionless form, this becomes

$$P\left(\psi, \hat{Z}_i \right) = P_s \,. \tag{14}$$

C. COMPUTER PROGRAM

1. Finite Difference Form

The computer program calculates the elements of the matrix and right side vector from three sources:

1. The dimensionless Reynolds equation (2), converted to finite difference form.

2. One of the dimensionless boundary conditions (4, 6, 8, or 10) for the chosen type of end seal (for each of the two damper ends), converted to finite difference form.

3. One of the dimensionless boundary conditions (12 or 14) for the chosen type of inlet, converted to finite difference form.

The equations indicated above are converted to finite difference form by substitution of the following difference expressions for the derivatives:

$$\left(\frac{\partial P}{\partial \psi} \right)_{j,k} = \frac{P_{j,k} - P_{j-1,k}}{\bar{\Delta}_\psi}, \tag{15}$$

$$\left(\frac{\partial P}{\partial Z} \right)_{j,k} = \frac{P_{j,k} - P_{j,k-1}}{\bar{\Delta}_z}, \tag{16}$$

$$\left(\frac{\partial^2 P}{\partial \psi^2} \right)_{j,k} = \frac{P_{j-1,k} - 2P_{j,k} + P_{j+1,k}}{\bar{\Delta}_\psi^2}, \tag{17}$$

and

$$\left(\frac{\partial^2 P}{\partial Z^2} \right)_{j,k} = \frac{P_{j,k-1} - 2P_{j,k} + P_{j,k+1}}{\bar{\Delta}_z^2}, \tag{18}$$

where $P_{j,k}$ is the dimensionless pressure at the node j,k of the finite difference grid, $\psi = (j-1)\bar{\Delta}_\psi$, $Z = (k-1)\bar{\Delta}_z$, and $\bar{\Delta}$ is the grid size.

The grid size is determined by choosing the number of points M, N to be defined on the damper circumference and length, respectively.

$$\bar{\Delta}_\phi = \frac{2\pi}{M-1}, \quad \bar{\Delta}_z = \frac{L}{N-1} \quad \frac{1}{R_o} \tag{19}$$

A concise description of the finite-difference method as applied to hydrodynamic bearing theory can be found in Reference 8.

---

8 Pinkus, O., and Sternlicht, B., "Theory of Hydrodynamic Lubrication," McGraw-Hill, Inc., New York, 1961, pp. 80-81.

The resulting finite-difference equations are as follows:

Main Program

$$\frac{\bar{\Delta}_\psi}{\bar{\Delta}_z^2} \; P_{j,k-1} + \left[1 - \frac{\bar{\Delta}_\psi}{2} \; f_{1_{j,k}} \right] P_{j-1,k} - 2 \left[\frac{\bar{\Delta}_\psi}{\bar{\Delta}_z^2} + 1 \right] P_{j,k}$$

$$+ \frac{\bar{\Delta}_\psi}{\bar{\Delta}_z^2} \; P_{j,k+1} + \left[1 + \frac{\bar{\Delta}_\psi}{2} \; f_{1_{j,k}} \right] P_{j+1,k} = \bar{\Delta}_\psi R_{j,k} \tag{20}$$

where

$$R_{j,k} = f_{3_{j,k}} \; \frac{d\phi}{dT} + f_{4_{j,k}} \; \frac{d\epsilon}{dT} \; ,$$

and

$$f_{3_{j,k}} \; , \; f_{4_{j,k}}$$

are the functions associated with equation (2), evaluated at the point j,k.

Subroutine Piston (Piston ring seal)

$$P_{j,N} \left[1 + \bar{\Delta}_z C_p' \right] - P_{j,N-1} = \bar{\Delta}_z C_p' P_e \; , \tag{21}$$

where

$$N = \frac{L}{R_b \bar{\Delta}_z} + 1.$$

Subroutine Rador (Radial O-ring seal)

$$P_{j,N} \left[\bar{\Delta}_\psi C_R' + K_R' + \frac{\bar{\Delta}_\psi}{\bar{\Delta}_z} \right] - K_R' P_{j-1,N}$$

$$- \frac{\bar{\Delta}_\psi}{\bar{\Delta}_z} \; P_{j,N-1} = \bar{\Delta}_\psi \; C_r' p_e \; , \tag{22}$$

where

$$N = \frac{L}{R_b \bar{\Delta}_z} + 1.$$

Subroutine Sidor (Side O-ring seal)

$$\sum_{j-1}^{M} \{H^3_{j,N-1} (P_c - P_{j,N-1})\} \ \frac{\bar{\Delta}_\psi}{\bar{\Delta}_z} + C_c' P_c = C_c' P_e , \tag{23}$$

with

$$P_{j,N} = P_c , \tag{24}$$

where

$$N = \frac{L}{R_b \bar{\Delta}_z} + 1.$$

Subroutine Noseal (No end seal)

$$P_{j,N} = P_e , \tag{25}$$

where

$$N = \frac{L}{R_b \bar{\Delta}_z} + 1.$$

Subroutine Holes (Inlet holes with backflow)

$$P_{J_i,N1} \left[2 + 2 \frac{\bar{\Delta}_\psi^2}{\bar{\Delta}_z^2} + \frac{\bar{\Delta}_\psi}{\bar{\Delta}_z} C_i' \right] - P_{J_i-1,N1} - P_{J_i+1,N1}$$

$$- \frac{\bar{\Delta}_\psi^2}{\bar{\Delta}_z^2} P_{J_i,N1-1} - \frac{\bar{\Delta}_\psi^2}{\bar{\Delta}_z^2} P_{J_i,N1+1} = \frac{\bar{\Delta}_\psi}{\bar{\Delta}_z} C_i' P_s , \tag{26}$$

where

$$C_i' = \frac{12\mu}{h^3} C_i ,$$

$j = J_i$ defines the circumferential location of the ith inlet hole.

$k = Ni$ defines the axial location of all the inlet holes.

The elements of the coefficient matrix A, the vector RHS, and the solution vector P are shown in equation (27). The banding of the coefficient matrix is accomplished by numbering the grid points of the finite difference grid in an alternating fashion around the circumference of the damper.

MATRIX EQUATION FOR M=6, N=4

$$[A]|P| = |RHS|$$

(27)

(Matrix coefficients are numbered as single array)

2. Solution of Pressure Matrix

The solution algorithm is a Gaussian elimination of the elements below the diagonal and a back substitution of unknowns in the reverse order. Integration of the pressure profile to get damper forces is done by Simpson's Rule for an even number of finite strips.

Pressures that fall below the damper cavitation pressure are set equal to the cavitation pressure for calculating the damper forces. Film cavitation is not well defined; however, test results show that cavitation pressure is approximately −14.7 psig (Reference 3).

The numerical accuracy of the above procedure was verified by comparing the predicted pressures with known "long bearing" and "short bearing" solutions to within 2%. The finite difference model had a grid of 6 × 40 and was analyzed in double precision arithmetic on an IBM 370 Model 168 computer. The average computation run time for this size model is approximately 0.1 sec.

26

A description of the complete computer program (Report No. FR-10732) was provided to the Applied Technology Laboratory in October 1978. A users manual for this program appears in Appendix A and B.

D. EXPERIMENTAL RIG DESIGN

The objective of the high-speed squeeze film damper test was to measure bearing damper forces and pressures over a range of design variables to enable comparison of the data with existing theories for predicting damper performance. The test rig duplicated the dynamics of existing engine squeeze film dampers, including the case of nonzero radial velocities.

1. Damper Design

The squeeze film damper rig configuration is shown in Figure 8. Design modifications incorporated into the existing damper rig (Reference 9) are summarized in Table 1. These modifications permitted the measurement of damper squeeze film pressures as a function of shaft position and velocity, and offset the shaft orbit to produce nonzero radial velocities.

The test rig consists of two accurately balanced disks joined together by a hollow shaft supported at the middle by a double row ball bearing. This mounts to the inner damper ring. The disk assembly is driven by a 2-in. air turbine via a quill shaft with a spline fitting on the driving end. To induce motion into the damper, the disks are unbalanced by a known amount. The damper force, pressure, and displacement measurements are then taken at various rotational speeds while the disks spin in an evacuated chamber.

The outer race of the duplex ball bearing is shrunk-fit inside the damper journal which is held in the damper bearing by a retaining ring and has complete lateral freedom of movement. The damper journal has a nominal outside diameter of 7.6 cm (2.99 in.). The damper has a length of 2.5 cm (0.98 in.) divided equally between the top and the bottom bands with a central oil-groove of about 1.25 cm (0.49 in.) width. This rather wide groove was required to fit the off-centered oil supply holes while retaining a symmetric damper. The oil film is limited in length at each damper end by a steel piston seal ring.

A radial spring arrangement is provided to simulate the gravity effect that exists in a horizontal rotor. The side load on the journal can be controlled by adjusting the length of the radial springs to produce a resultant pull of 5.6 kg (12.4) on the damper, equal to the wei   of the rotating parts.

The clearance space between the damper sleeve and the bearing housing is filled with the damping fluid which is pressure fed into the central circumferential groove.

The rotor is mounted vertically in a containment casting that is evacuated to 60 Torricil. The rotor is driven by a commercial 5-cm (2-in.) air turbine via a quill shaft. The rotor can be driven over a wide speed range. The maximum speed is limited by the bearing temperature and did not exceed 50,000 rpm during the tests. The excitation force is provided by two equal weights attached to the top and bottom disks in the same vertical plane.

---

9 Botman, M., "Experiments on Oil-Film Dampers for Turbomachinery," Journal of Engineering for Power, Trans. ASME, Series A, Vol. 98, July 1976, pp. 393-399.
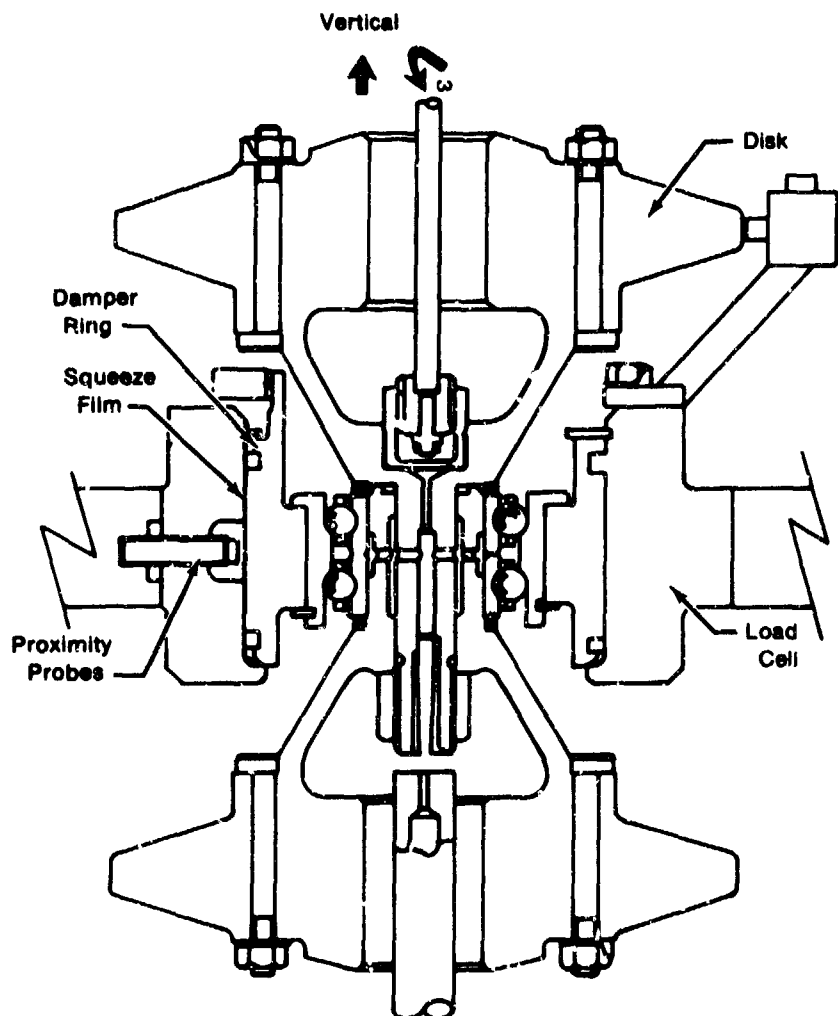
Figure 8. Squeeze Film Damper Rig

2. Instrumentation

The oil supply line to the damper is equipped with a regulator valve, a pressure gage, and a flowmeter. The inlet oil pressure can be adjusted in the range of 5 to 100 psig. The oil coming out of the damper passes through another flowmeter. The two flowmeters provide information on the flowrate within the damper as well as the leakage from its seals.

The oil film and the bearing temperatures are monitored by two copper-con thermocouples mounted flush with the damper journal.

The transmitted load is measured by the two strain gage bridges placed at right angles to each other on the curved spokes of the load cell. The load cell was calibrated statically to measure radial loads in two directions. It has a radial stiffness of 243×10^6 N/m (1.39×10^6 lb/in.). The output signal from the strain gages is amplified and recorded on an FM magnetic tape.

TABLE 1
DAMPER RIG MODIFICATIONS

Item	Revision
Damper Sleeve	Provision was made for offset orbits and circumferential oil groove.
Pressure Probe Bushing	Will now accept dynamic (Kistler) and static (Statham) pressure probes.
Load Cell	Additional pressure probe taps were included.
Load Cell Support	Additional holes for securing spring device which produces off-set orbits.
Retainer Ring	Ring material was changed from steel to Teflon to reduce friction.
Damper Seals	Seal material was changed from Teflon to steel to be more representative of typical damper designs.

The displacement of the damper sleeve at the oil film is measured by two inductance type proximity probes mounted in the load cell at the midplane of the top land, displaced 90 deg from each other. Both ac and dc components of these probes can be monitored.

Eight holes with a diameter of 0.125 cm (0.050 in.) were drilled 45 deg apart in the midplane of the bottom land of the damper. These holes are connected to the Kistler and the Statham type pressure transducers. The Kistler transducers are used to measure the dynamic pressure, and the Statham transducers the static oil-film pressures. Thus, the instantaneous fluid-film pressure distribution, which is rotating with the speed of the rotor, is measured in the midplane. Because of space limitations, only four holes were drilled in the top land of the damper for pressure measurements. The output signals from the pressure transducers are recorded on magnetic tape.

The inertia effects of the support mass are measured by means of two B&K accelerometers mounted orthogonally at the load cell. The accelerometer output is also recorded on the magnetic tape via charge amplifiers.

The amplitudes of the lower and the upper disks are measured by two inductance type displacement probes. The reference signal from a marker on the rotor is used to measure the phase angles between different signals. A magnetic probe is used for this purpose. Another magnetic probe is used for monitoring the speed of the rotor.

The damper proximity probes were calibrated before each build to study the drift in the calibration constants from build to build. No significant drift was observed.

The damper oil used is a synthetic oil MIL-L-23699 whose viscosity and specific gravity varies as a function of its temperature. In the tests, the temperatures varied from 27°to 93°C (80° to 200°F) with the corresponding variation in absolute viscosity from 37.85 × 10⁻³ N-sec/m² (5.47 × 10⁻⁷ lb sec/in.²) to 5.05 × 10⁻³ N-sec/m² (0.73 × 10⁻⁶ lb sec/in.²).

The basic damper instrumentation is shown in Figure 9.
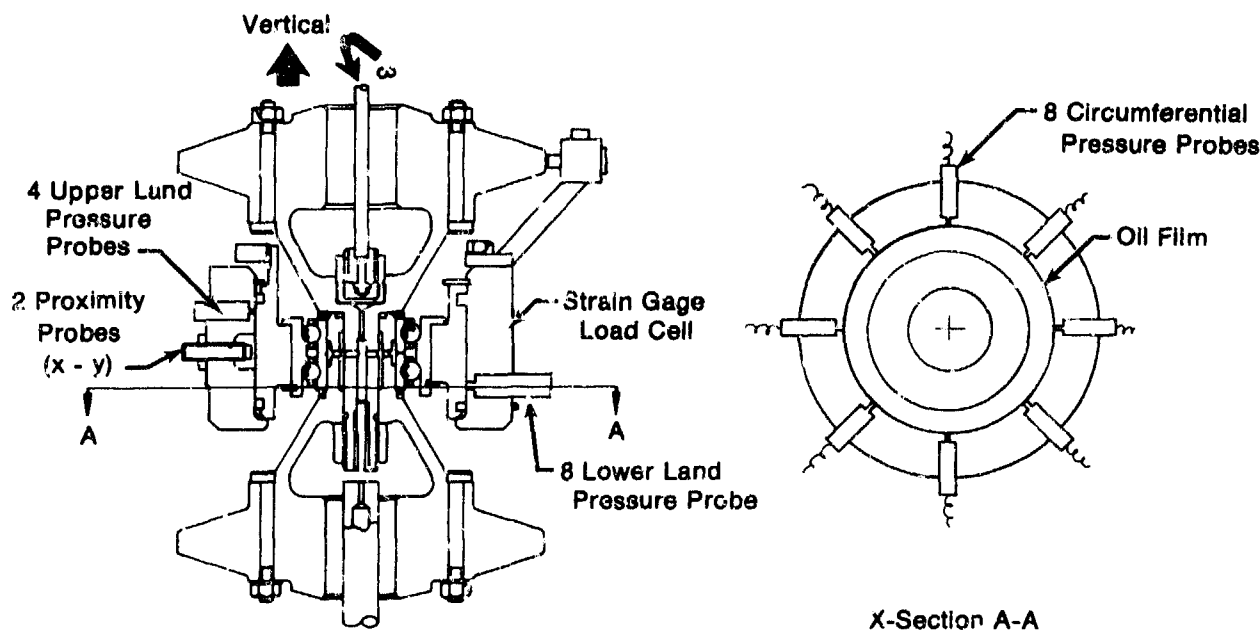
Figure 9. Damper Rig Instrumentation

E. RIG TEST AND RESULTS

1. Test Program

Tests were performed for three values of radial clearance and three values of imbalance for both concentric and eccentric orbits. Table 2 summarizes the parameter combinations for the various runs. The effect of inlet oil pressure was also studied at three different values of the pressure.

The rotor was run over a wide speed range and measurements were taken at selected constant speeds at intervals of 5000 rpm up to a maximum speed of 50,000 rpm. At each speed, measurements were taken of the damper sleeve deflections, transmitted loads, support accelerations, instantaneous oil-film pressures and the associated phase angles The oil flow and bearing temperatures were recorded manually at each of these speeds.

The damper sleeves had a circumferential oil inlet groove and piston ring end seals which simulated a typical high-speed engine damper configuration. The damper radial clearances were 0.005, 0.010, and 0.015 in., typical of current damper designs.

30

TABLE 2
THE PARAMETER COMBINATIONS FOR VARIOUS RUNS

Run No.	Orbit	Inlet Oil Pressure (psig)	Imbalance (gm cm)	Radial Clearance (mm)	Imbalance Phase Relative to Marker (deg)
1.1	Concentric	30	0	0.127	15 lag
1.2	Concentric	30	27.4	0.127	15 lag
1.3	Concentric	30	13.7	0.127	15 lag
1.4	Eccentric	30	13.7	0.127	15 lag
1.5	Eccentric	30	27.4	0.127	15 lag
1.6	Eccentric	30	0	0.127	15 lag
1.7	Concentric	30	0	0.127	15 lag
2.1	Concentric	30	0	0.254	15 lead
2.2	Concentric	30	13.7	0.254	15 lead
2.3	Concentric	30	27.4	0.254	15 lead
2.4	Eccentric	30	27.4	0.254	15 lead
2.5	Eccentric	30	0	0.254	15 lead
2.6	Eccentric	30	13.7	0.254	15 lead
2.7	Eccentric	60	13.7	0.254	15 lead
2.8	Eccentric	100	13.7	0.254	15 lead
3.1	Concentric	30	0	0.381	15 lead
3.2	Concentric	30	13.7	0.381	15 lead
3.3	Concentric	30	27.4	0.381	15 lead
3.4	Eccentric	30	27.4	0.381	15 lead
3.5	Eccentric	30	0	0.381	15 lead
3.6	Eccentric	30	13.7	0.381	15 lead
3.7	Eccentric	5	13.7	0.381	15 lead

2. Test Results

Some of the results obtained from the tests are presented in Figures 10 through 16. Figure 10 shows the variation of the bearing and oil-film temperatures with speed. The influence of the unbalance on the bearing temperatures was found to be marginal, the temperatures being slightly higher for higher unbalances. The oil leakage through the piston rings is plotted in Figure 11. It is suspected that most of the oil leakage occurred through the location where the piston ring ends butt together.

The damper orbits remained nearly circular and the pressure profile nearly sinusoidal up to a certain speed range. As the speed was further increased, the pressure profile exhibited a flat portion indicating a region with zero pressure. This is referred to as onset of cavitation. When the speed was further increased, the orbits became irregular, indicating nonsynchronous whirl.

31
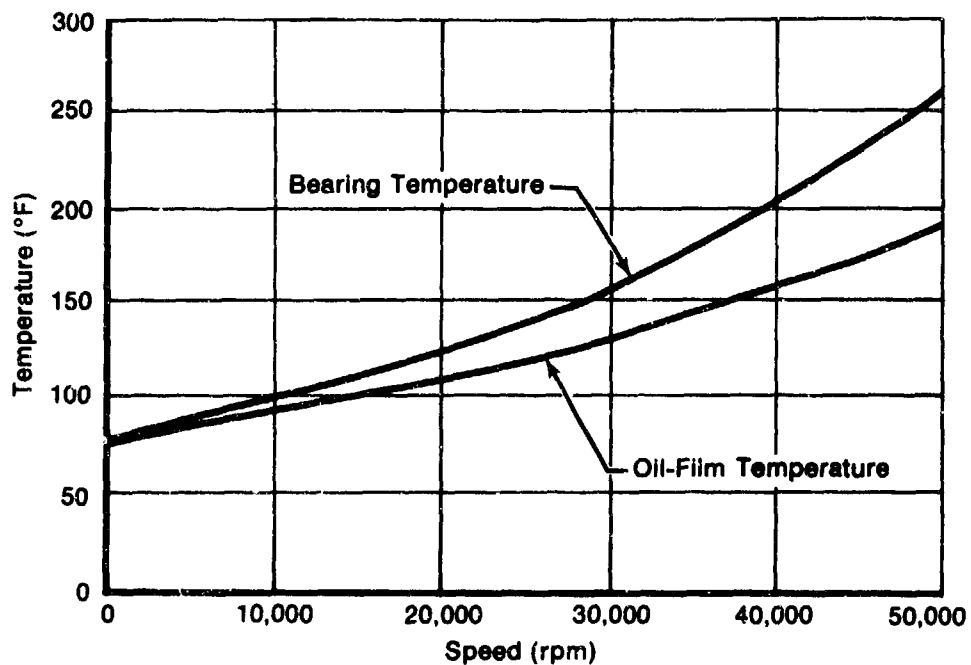
Figure 10. Temperature vs Speed Curve for Bearing and Oil Film
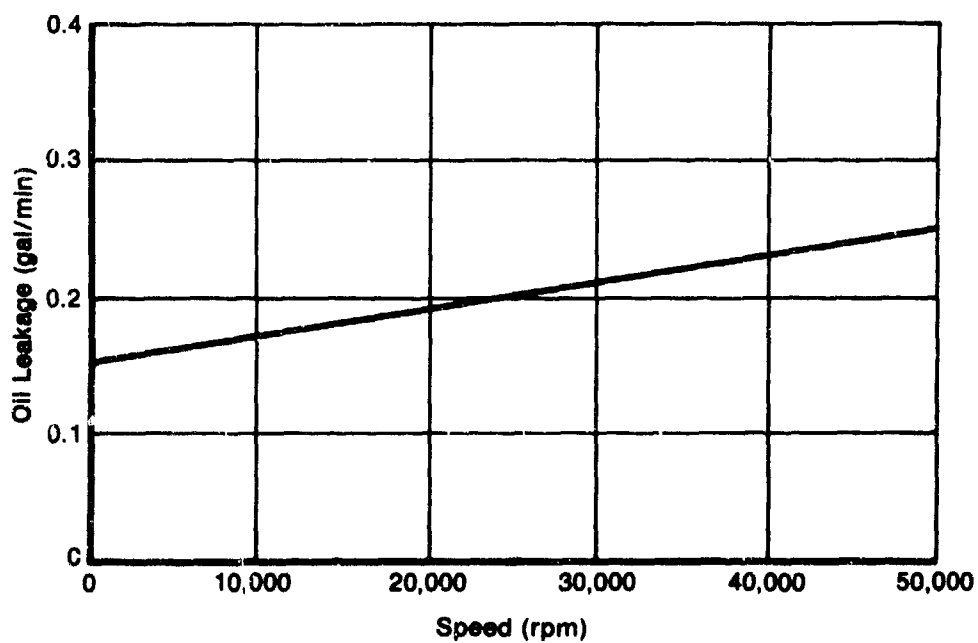
Figure 11. Oil Leakage

32
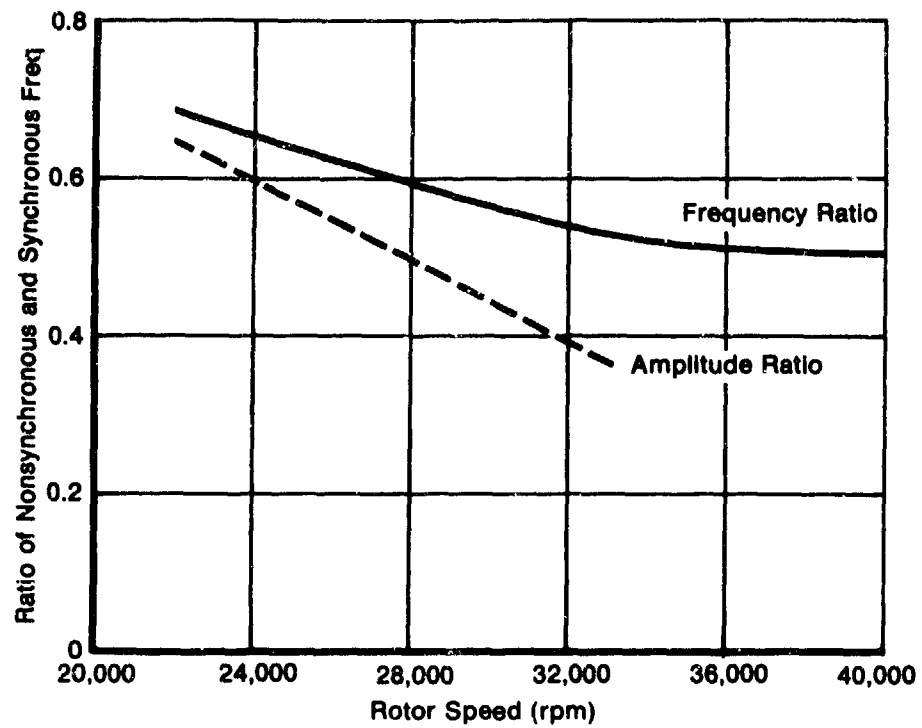
Figure 12. Fractional Frequency Components
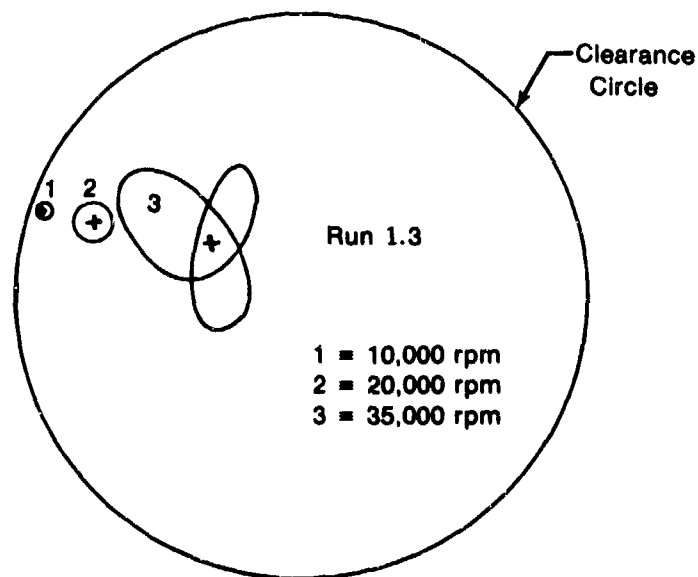
Figure 13. Damper Orbits Without Radial Springs
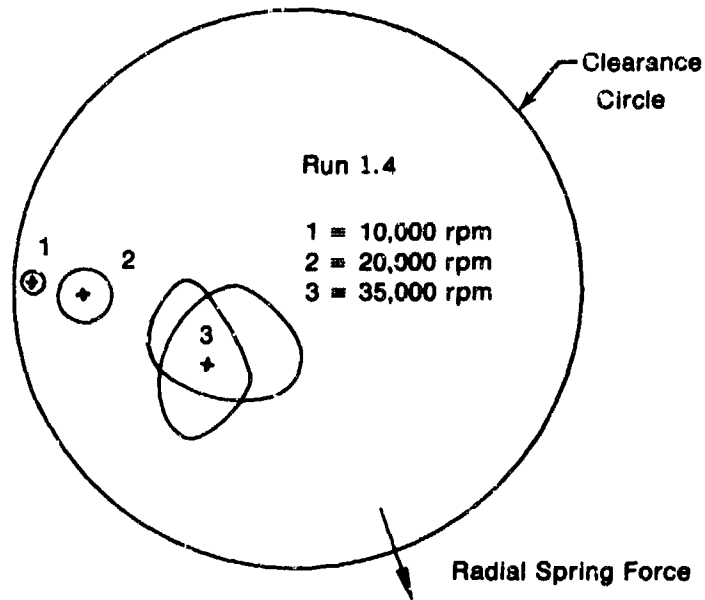
Figure 14. Damper Orbits With Radial Springs
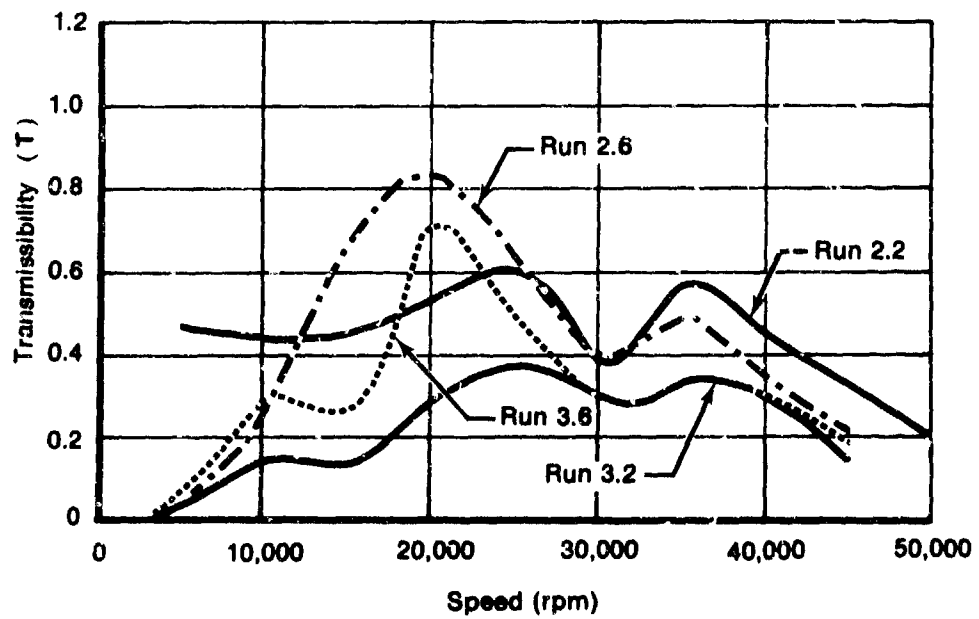
Figure 15. Transmissibility Curves
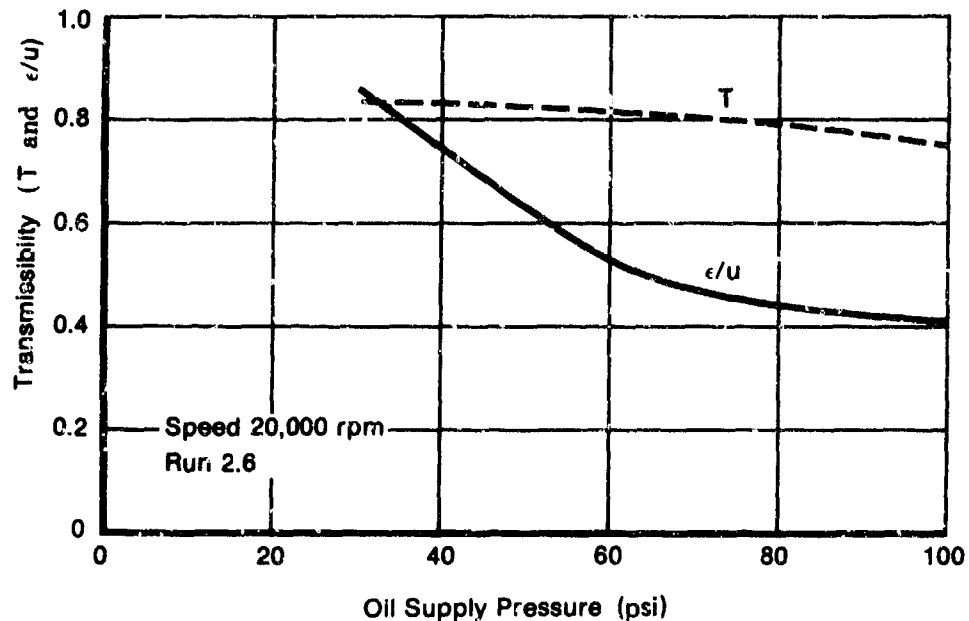
Figure 16. Effect of Oil Supply Pressure on Transmissibility and Damper Deflections

The cavitation was observed to progress rapidly and was followed by multi-loop orbits. At the onset of multi-loop orbits, the film extent was generally found to be less than 180 deg. The multi-loop orbits show up as a fractional frequency component. Spectrum analysis of the signals indicated this fractional frequency to be centered around 270 ± 25 Hz. This is shown in Figure 12, where frequency of the nonsynchronous component is plotted as a percentage of synchronous frequency. After the onset of this instability, the fractional frequency remained practically constant until it reached half the rotor speed. At higher speeds, this frequency then remained at half the rotor speed with substantially reduced associated amplitudes. The ratio of nonsynchronous vibration amplitude to the synchronous vibration amplitude is also shown in Figure 12. It decreased with increased speeds.

With a balanced rotor, no fractional frequency whirl was observed. With a moderate amount of imbalance, the fractional frequency whirl disappeared beyond a certain speed range. For all runs with an unbalance of 13.7 gm cm (0.19 oz in.), the fractional frequency component disappeared at rotor speeds exceeding 43,000 rpm. The orbits became circular again when the fractional frequency component disappeared at higher speeds.

Figures 13 and 14 show the size and the location of the damper orbit within the clearance circle for runs 1.3 and 1.4, respectively, at different speeds. With increasing speeds and unbalances, the orbit size grew and the journal center moved toward the bearing center. The orbits tended to be concentric at higher speeds and higher unbalances. The orbit size and shape for the rotor with radial springs were similar to those without radial springs except that the journal center was displaced toward the radial spring force for eccentric orbits. At low speeds, the journal was displaced on one side by the impact of the inlet oil jet.

The transmissibility, as defined by the ratio of the load transmitted to the load cell to the unbalance force, is shown in Figure 16. It is seen to be lower for dampers with larger clearances

36

and slightly higher for eccentric orbits up to the speeds where the oil film forces were greater than radial spring forces.

The effect of inlet oil pressure on the transmissibility and the damper deflections is shown in Figure 16. The high inlet oil pressure reduced both the damper deflections and transmitted loads in the synchronous operating range of the damper as shown in the figure.

F. DATA CORRELATION WITH ANALYTICAL MODEL

The objective of the data correlation was to verify the ability of the computer analysis model to predict the forces and pressures that occur in damper designs commonly used in gas turbine engines.

The test data were taken from the high-speed free-rotor rig test (Section II.D) plus three previously reported low-speed controlled-orbit rig tests (References 3, 4, and 5). The free-rotor damper rig attained speeds of 50,000 rpm, while the maximum speed of the other three rigs (Figure 17) was 3000 rpm. These rigs represented a good cross section of dampers commonly used in the gas turbine engine industry by exhibiting a variety of damper sizes and end-seal configurations. The results of the computer analysis described above agree closely with the data from the three controlled-orbit rigs.

1. High-Speed Rig

Figure 18 shows the squeeze film pressure correlation with the high-speed free-rotor rig. The damper speed is 20,000 rpm and the radial clearance is 5 mils. The data correlation shown is typical of all rig speeds and clearance. The eight measured data points were recorded at an instant in time by the eight equally spaced pressure transducers placed around the circumference of the damper. The corresponding predicted pressures were calculated for the same instant of time. The triangle symbols represent the pressures predicted by modeling the piston ring seals with a radial gap of 1 mil. These pressures were always predicted higher than the measured values, which suggests that this type of seal may leak more than had been anticipated. If the piston ring end seals are modeled as being totally ineffective (unrestricted end leakage), the predicted and measured pressure compare very closely. The unrestricted leakage assumption is supported by the relatively high leakage rate of 0.3 gal/min measured at this test point.

2. Low-Speed Rigs

Figures 19 through 21 show the comparison of measured and analytically predicted squeeze film pressures. These figures also show the predictions of two currently used analytical models, based on simplified assumptions.

Note that, although the "long bearing" theory is in reasonable agreement with one rig and the "short bearing" theory with another, the finite difference model is in good agreement for all three controlled-orbit rigs.

36
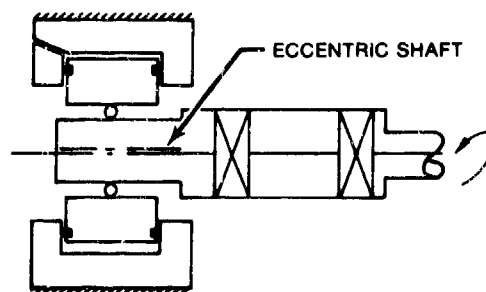
A. REF 3 RIG-SINGLE HOLE INLET, AXIAL O-RING SEALS
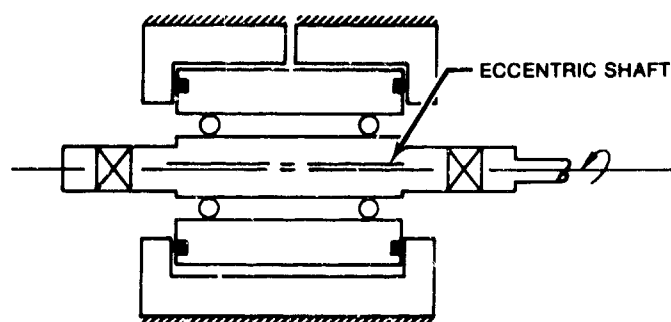
B. REF 4 RIG-SINGLE HOLE INLET, AXIAL O-RING SEALS
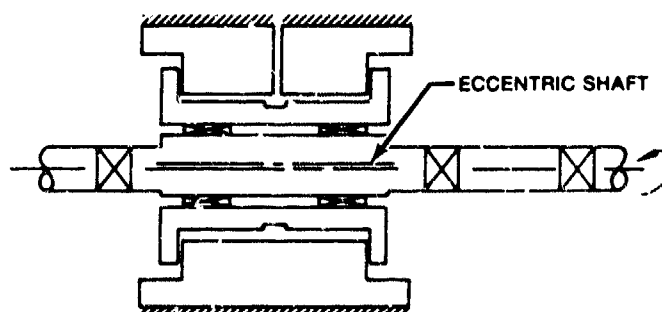
C. REF 5 RIG-CIRCUMFERENTIAL GROOVE INLET,
SMALL CLEARANCE SEAL

Figure 17. Low-Speed, Controlled-Orbit Damper Rigs

37

RADIAL VELOCITY = -0.931 in./sec

TANGENTIAL VELOCITY = 0.778 in./sec

Damper (Fig 7)
RADIUS = 1.5 in. (3.81 cm)
LENGTH = 1.0 in. (2.54 cm)
CLEARANCE = 0.0052 in. (0.0132 cm)
ECCENTRICITY = 0.0031 in. (0.0079 cm)
SUPPLY PRESS = 30 psig
SPEED = 20,000 rpm
VISCOSITY = 3.3X10^{-6} lb-sec/in.^{2} (reyn)
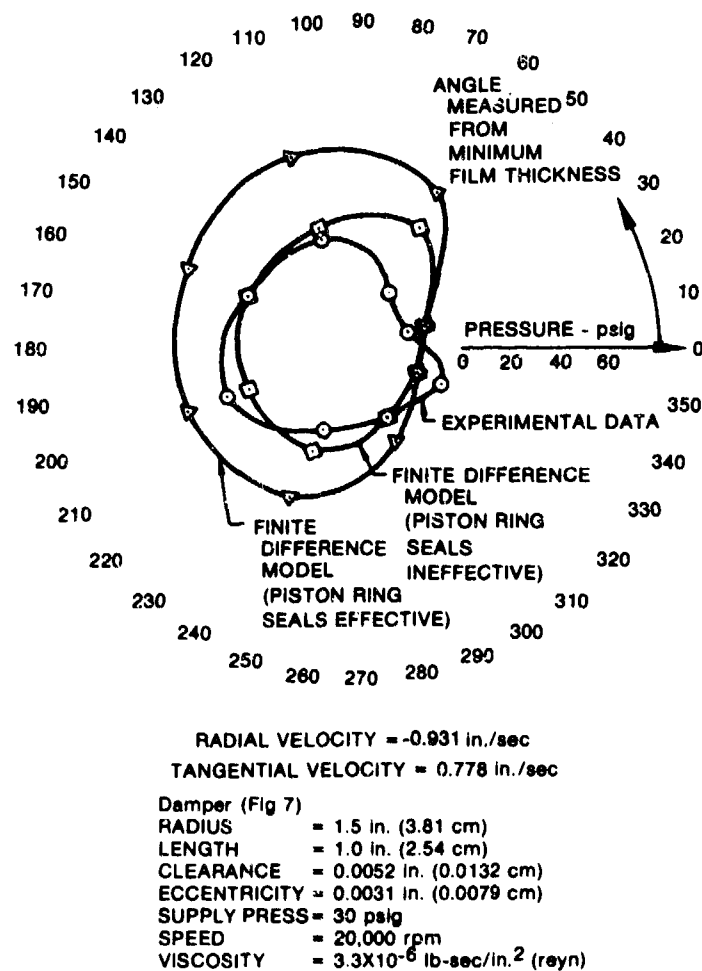
Figure 18. Free-Rotor Rig Data Correlation

The controlled-orbit rig reported by Feder (Reference 3) had O-ring side seals that allowed very little leakage. Therefore, the "long bearing" approximation to the lubrication theory shows nearly as good a comparison with the experimental data as the finite difference analysis (Figure 19). The rig used by Vance and Kirton (Reference 4) also had very effective end seals and had a single hole inlet, so it also is approximated fairly well by the "long bearing" model as shown in Figure 20. However, the predicted peak pressure deviates from the measured amplitude by a factor of two, a deviation which is significantly reduced by the predictions of the finite difference model.

At the other extreme, the rig used by Jones (Reference 5) had a circumferential oil feed and end seals which allowed considerable leakage. As shown in Figure 21, the "long bearing" approximation is completely inappropriate for this configuration. The "short bearing" model is a closer approximation but does not fit the data as well as the finite-difference model that includes both the effects of the end leakage and the inlet flow.

38
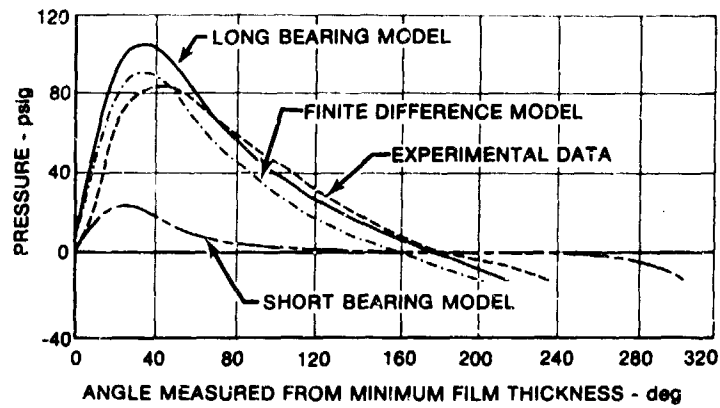
DAMPER 1 (Fig 8a)
RADIUS   = 3.22 in. (8.18 cm)
LENGTH   = 2.0 in. (5.08 cm)
CLEARANCE   = 0.020 in. (0.0508 cm)
ECCENTRICITY = 0.014 in. (0.0356 cm)
SUPPLY PRESS = 30 psig
SPEED   = 1000 rpm
VISCOSITY   = 2.62X10^{-6} lb-sec/in.^{2} (reyn)

Figure 19. Controlled-Orbit Rig Data (Ref 3) Correlation
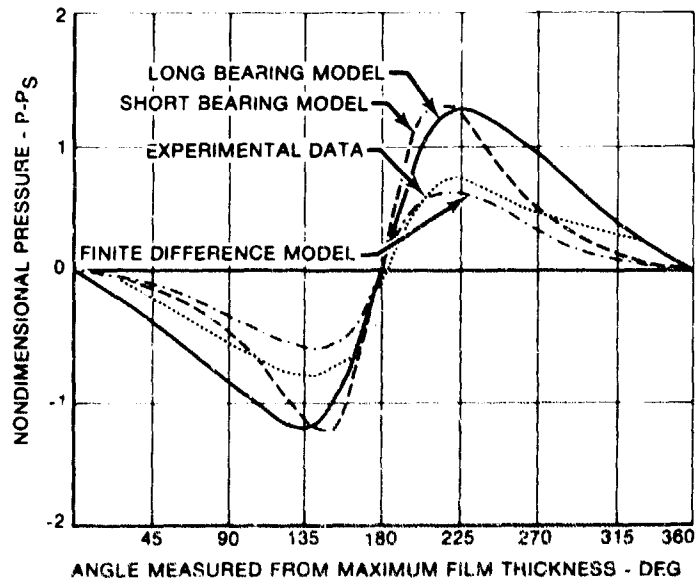
DAMPER 2 (Fig 8b)
RADIUS   = 2.5 in (6.35 cm)
LENGTH   = 4.813 in. (12.23 cm)
CLEARANCE   = 0.062 in. (0.157 cm)
ECCENTRICITY   = 0.031 in. (0.0787 cm)
SUPPLY PRESSURE = 60 psig
SPEED   = 1766 rpm
VISCOSITY   = 27.4X10^{-6} lb-sec/in.^{2} (reyn)

Figure 20. Controlled-Orbit Rig Data (Ref 4) Correlation
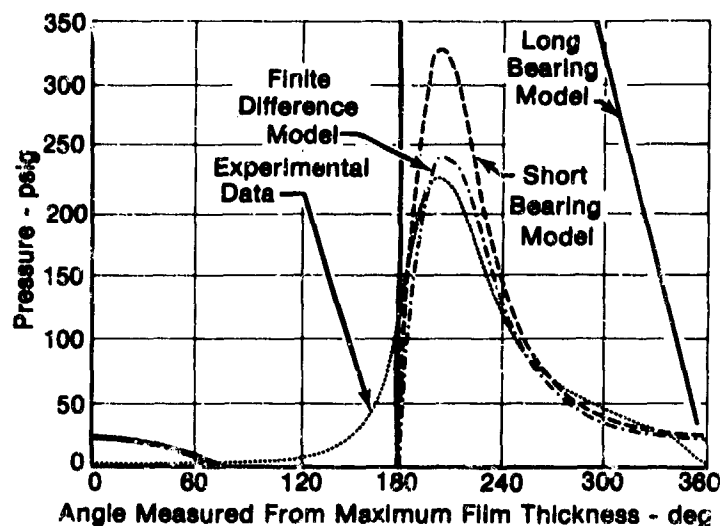
Damper (Figure 17, Part C)

Radius	= 1.5 in. (3.81 cm)
Length	= 2.0 in. (5.08 cm)
Clearance	= 0.010 in. (0.254 cm)
Eccentricty	= 0.0068 in. (0.0173 cm)
Supply Press	= 10 psig
Speed	= 3000 rpm
Viscosity	= 12.3 x 10^{-6} lb-sec/in.^{2} (reyn)

Figure 21. Controlled-Orbit Rig Data (Ref 5) Correlation

In summary, the predictions of the computer analysis model are in close agreement with experimental data taken from the three controlled-orbit rigs, and are in fair agreement with data from the high-speed free-rotor rig. Measurements taken from the latter type rig are inherently less precise,* although they simulate actual gas turbine conditions much more closely. Overall, the data correlations demonstrate a high order of accuracy and versatility for the finite difference model described previously.

―――――――

*There are more variables to be measured in this type rig, under more difficult conditions.

SECTION III

BEARING SUPPORT CHARACTERIZATION (TASK IV)

Impedance tests, using a shaker apparatus, were used to determine the stiffnesses, damping values, and natural frequencies of nine flexible bearing supports of three different designs: round rod supports, squirrel cage supports, and curved beam supports. Three variations of each support type were tested. The round rod and squirrel cage designs were chosen because of their widespread use in turboshaft engines; the curved beam supports, an innovative new design, were chosen because of their compactness, low stress levels under loading, and the high amount of damping they provide. The main purpose of the experiment was to test the validity of current analytical techniques used in predicting support stiffness; the predicted and experimental stiffness data correlated well. A formula based on beam theory was used in predicting the stiffness of the round rod and squirrel cage supports, and Castigliano's Theorem was combined with Curved Beam Theory to yield the stiffness of the curved beam supports. The experimental results and the analytical formulae are contained in this report.

A. TEST CONFIGURATION

Figures 22 and 23 illustrate the test configurations for the round rod and curved beam supports. (The configuration for the squirrel cage supports is similar to that of the round rod supports.) These fixtures simulate the mounting of the supports in an actual engine installation. Massive "plugs" were mounted inside the ID of the round rod and squirrel cage supports when necessary to simulate the bearing outer races and to prevent ovalization of the support during testing. Support fixtures were bolted to a massive steel table to assure end rigidity. Figures 24 and 25 are photographs of the squirrel cage and curved beam support test rigs, respectively.
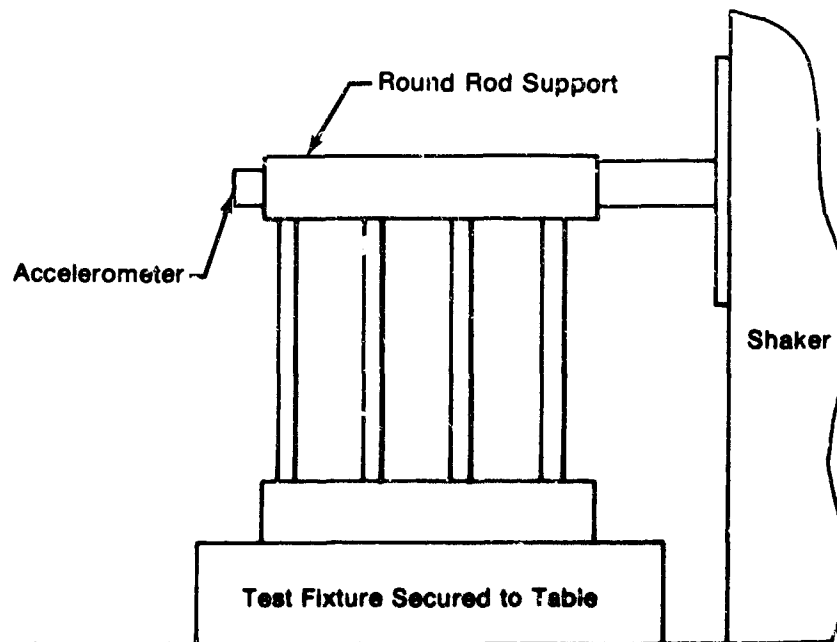
Figure 22. Side View of Round Rod Support Test Configuration
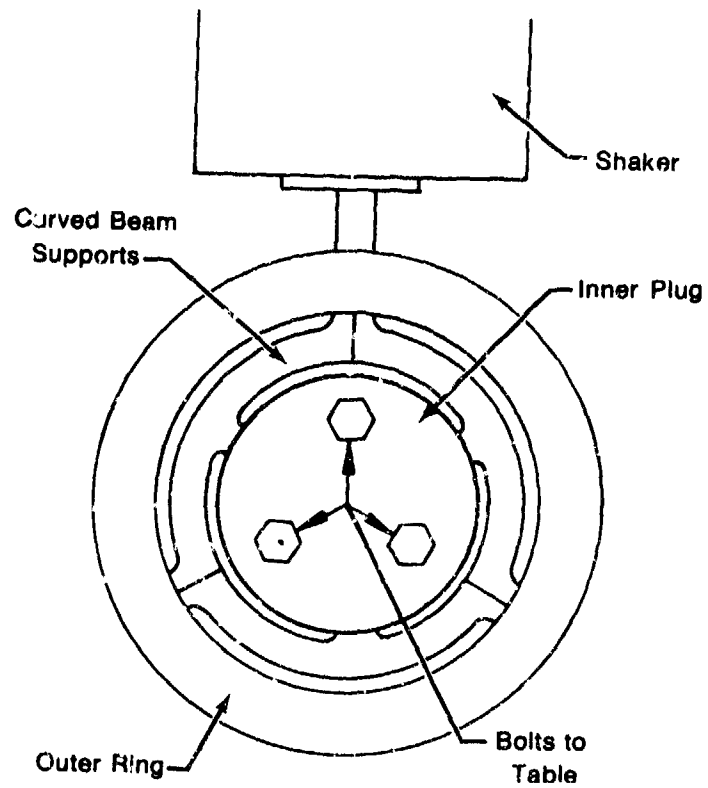
Figure 23. Top View of Test Configuration OFR Curved Beam
Supports
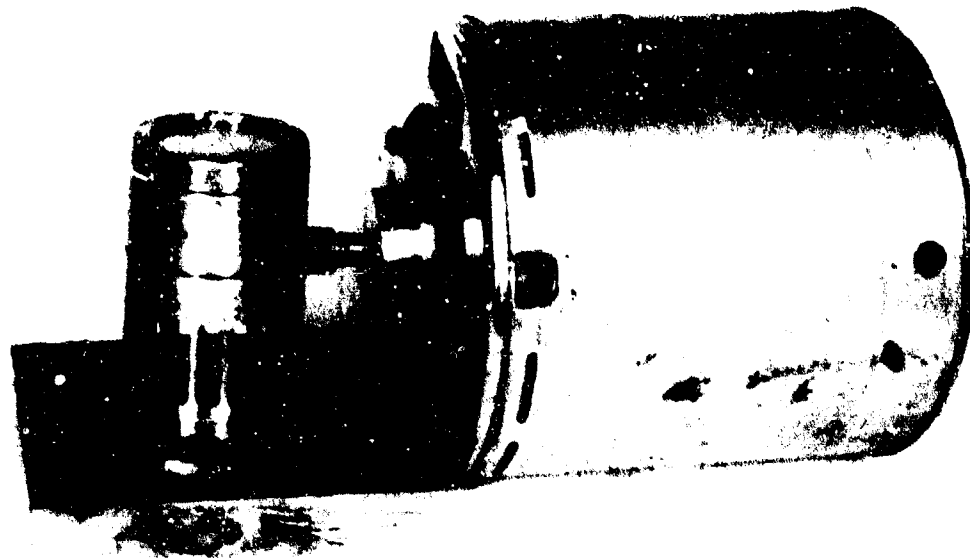
Figure 24. Squirrel Cage Test Rig

Figure 25. Curved Beam Support Test Rig

A force applied to the flexible support using an electromechanical shaker was measured by the attached load cell and signal amplifier over a frequency range of 10 to 2,000 Hz; the response was measured by an accelerometer mounted directly opposite the shaker. Plots were then made of mechanical impedance versus frequency; the stiffness and damping values were then directly extracted from the impedance plots. For a vibrating spring-mass-damper system being excited by a sinusoidal force at a force at a frequency less than one-half the natural frequency, the primary resistance force is due to the spring force. At the natural frequency the resistance force is due to damper. Taking advantage of these characteristics of a dynamic system, the spring and damping rates of the bearing supports were determined from the mechanical impedance plots. These values were designated as the experimental dynamic stiffness and damping terms.

B. RESULTS

1. For the squirrel cage supports, the variation between the experimental dynamic stiffness and the calculated static stiffness ranged from −6% to +8%.

2. For the round rod supports, the variation between the experimental dynamic stiffness and the calculated static stiffness ranged from −15% to −51%.

3. For the curved beam supports, the variation between the experimental dynamic stiffness and the calculated static stiffness ranged from +5% to +27%.

43

4. The damping from the squirrel cage and round rod supports was negligible.

5. The damping from the curved beam supports was significant, ranging from 4.1 to 10.0 ib-sec/in.

Note that in Results 1, 2, and 3 the experimental *dynamic* stiffness was compared to the calculated *static* stiffness. This is because the static stiffness measured at low frequencies was found to equal the dynamic stiffness.

A summary of the experimental and analytical results is provided in Table 3.

The experimental values shown for structural damping are fairly consistent. Yet the minimum and maximum damping values for the round rod supports differ by a factor of ten. Following is a possible explanation: Inside each of the round rod supports is a sleeve up n which the piston rigs are mounted. In the assembly process, it is possible that the sleeve may have been brazed off-center such that rubbing occurred between the sleeve and the inner surface of the main body of the support. This would explain both the large variation in structural damping and the large amount of damping that two of the round rod supports had when compared with the squirrel cage supports.

Note the high amount of damping that the curved beam supports exhibited. This was due to the following: As the beam was deflected by the load in the y direction, the chord AB changed in length (Figure 26). As the chord changed in length, the supporting ends of the beam moved circumferentially along the supporting surface, causing frictional damping.

C. SUPPORT STIFFNESS FORMULA

For round rod supports, the following formula should be used to predict the static stiffness:

$$K = \frac{12 \, NE \, \pi \, d^4}{64L^3 + 112.32d^2L}$$

For squirrel cage supports:

$$K = \frac{NEbt}{2} \left(\frac{1}{L^3/t^2 + 13L/6} + \frac{1}{L^3/b^2 + 13L/6} \right)$$

Here

K is the stiffness
b is the leg width
t is the leg thickness
L is the length of the leg (see Figure 27)

Castigliano's Theorem and Curved Beam Theory yield the following equations for calculating the support stiffness of a 3-beam support:

$$K = 0.331 \, \frac{Et^3h}{r^3_{av}}, \text{ where } r_{av} = \frac{r_1 + r_2}{2}, \, t = r_2 - r_1$$

44

TABLE 3
SUMMARY OF RESULTS FOR ROUND ROD, SQUIRREL CAGE, AND CURVED BEAM SUPPORTS

Support	Type	Average Leg Length (in.)	Average Leg Thickness (in.)	Average Leg Width (in.)	Average Leg Diameter (in.)	Number of Legs	W_c (HZ) Measured	K_s (lb/in.) Measured	K_s (lb/in.) Predicted	Old Design K_s	K_s (lb/in.) Measured	Damping (lb-sec/in.) Measured	Material
216779	Sq. Cage	1.305	0.125	1.146	—	18	444	100,531	93,500	129,779	92,000	0.68	AMS 641
GKJ 5184	Sq. Cage	2.080	0.081	0.321	—	16	377	50,265	54,812	74,735	52,000	0.105	AMS 641
GKJ 5187	Sq. Cage	1.000*	0.102*	0.102*	—	22	402	43,364	70,331	99,203	80,000	0.1	AMS 561
GKJ 4683-1	Round Rod	1.83*	—	—	0.125*	16	129	13,195	11,298	—	14,000	0.08	AMS 630
GKJ 4683-2	Round Rod	1.83*	—	—	0.1875*	16	425	125,000	64,850	—	120,000	0.8	AMS 630
GKJ 4683-3	Round Rod	1.65*	—	—	0.1875*	16	290	67,858	82,080	—	70,000	0.9	AMS 630

*Nominal values assumed because measurements were not taken.

Support	Type	R (in.)	r_0 (in.)	W_c (HZ) Measured	K_s (lb/in.) Measured	K_s (lb/in.) Measured	K_{si} (lb/in.) Predicted	Damping (lb-sec/in.) Measured	Material
GKJ 5188	Curved Beam	1.4825	1.7635	150	41,720	63-51,000	66,345	10.0	AMS 347
GKJ 5189	Curved Beam	1.5325	1.7635	180	24,630	25-29,000	27,729	10.0	AMS 347
GKJ 5270	Curved Beam	1.5725	1.7635	130	12,568	12-13,000	15,076	4.1	AMS 347

Note: The experimental values for the static stiffness K_s was determined by multiplying the impedance (corresponding to the lowest frequency for which good data existed) times the corresponding frequency.
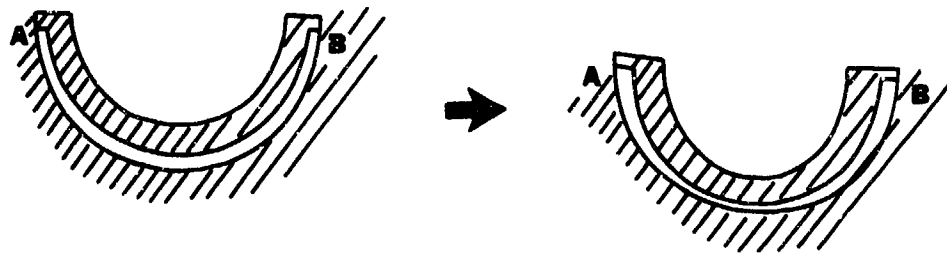
Figure 26. Curved Beam Geometry

Squirrel Cage

Round Rod
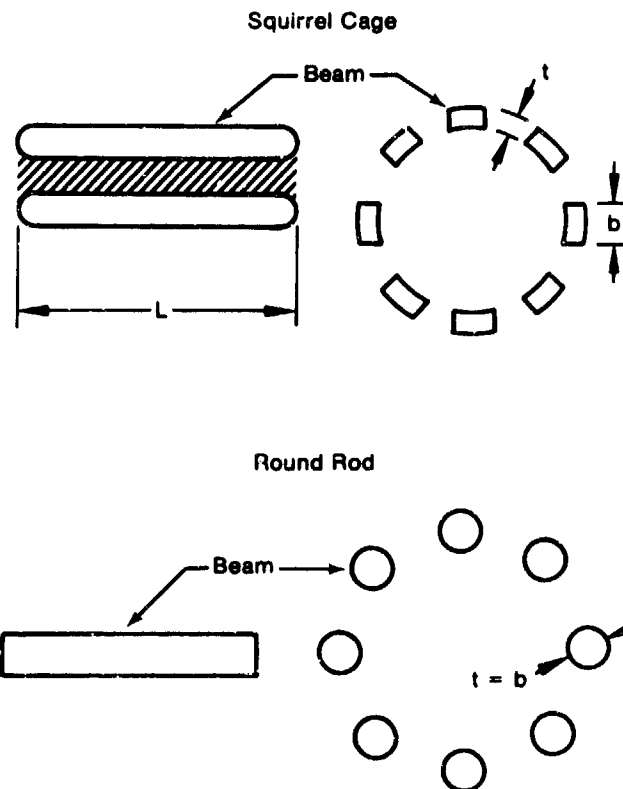
Figure 27. Beam Dimensions

Here K is the support stiffness, and E is the material modulus of elasticity. The support dimensions are shown in Figure 28.

NOTE: This formula becomes increasingly inaccurate as r_{av}/t becomes less than 10.
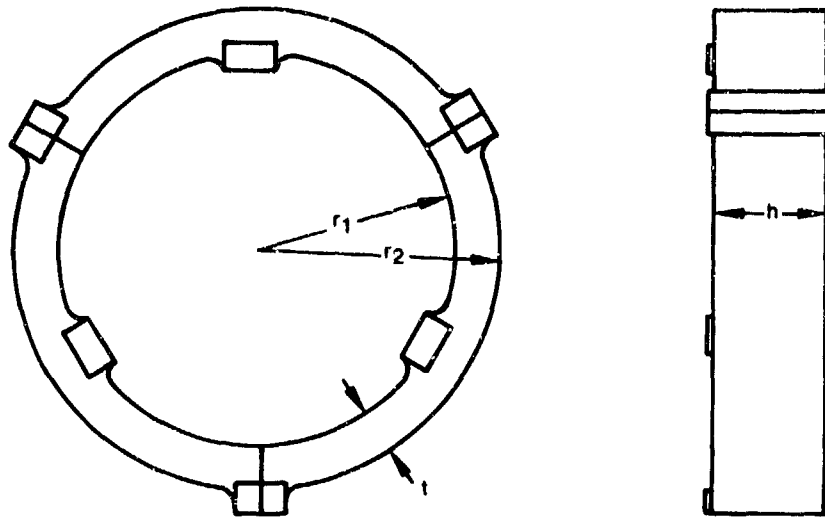
Figure 28. Curved Beam Support Dimensions

D. CONCLUSIONS

Existing beam formulas for calculating the stiffness of flexible bearing supports have satisfactory accuracy for estimating support performance. If a maximum error of about 20% cannot be tolerated, then a more precise modeling technique such as a finite element method should be used.

SYNCHRONOUS WHIRL RIG — ANALYSIS VERIFICATION (TASKS V, VI, AND VII)

A comprehensive program was conducted to both analytically predict and experimentally verify the dynamic response of a viscous-damped flexible rotor system subjected to both normal and abnormal imbalance conditions. The test model simulated future front-drive power turbine configurations; i.e., it consisted of a long slender shaft with flexible, viscous damped bearing supports and an overhung drive turbine.

This program was designed to determine, by parametric testing, the optimum combination of stiffness and damping for subcritical and supercritical shafting. The optimum design is defined as one which simultaneously limits bearing loads to low levels, controls rotor motion to prevent shroud contact, and absorbs large, suddenly applied imbalance without failure.

Analytical predictions employed were made using the viscous damper analysis methods substantiated in Task III.

A. EXPERIMENTAL RIG DESIGN

The synchronous reponse rig (Figures 29 through 31) consists of a main shaft with two disks mounted near one end to simulate a front-drive power turbine rotor. The shaft is provided with five balance planes. This allows for multiplane balance of the rig as well as provides controlled imbalance. The shaft measures 14.2 in from bearing to bearing with a diameter of 0.9 in. and a weight of 20.5 lb. The front end of the shaft incorporates a preloaded duplex bearing and viscous damper. However, this damper was inactive during the test to isolate the effects of the turbine and damper being studied. The aft end of the shaft is supported by a roller bearing. The roller bearing is also equipped with a viscous damper. The damper length and diameter are 1.2 in. and 4.0 in. respectively. Damper parameters, such as oil-film thickness, bumper clearance, and bearing support spring rate, were varied during test.
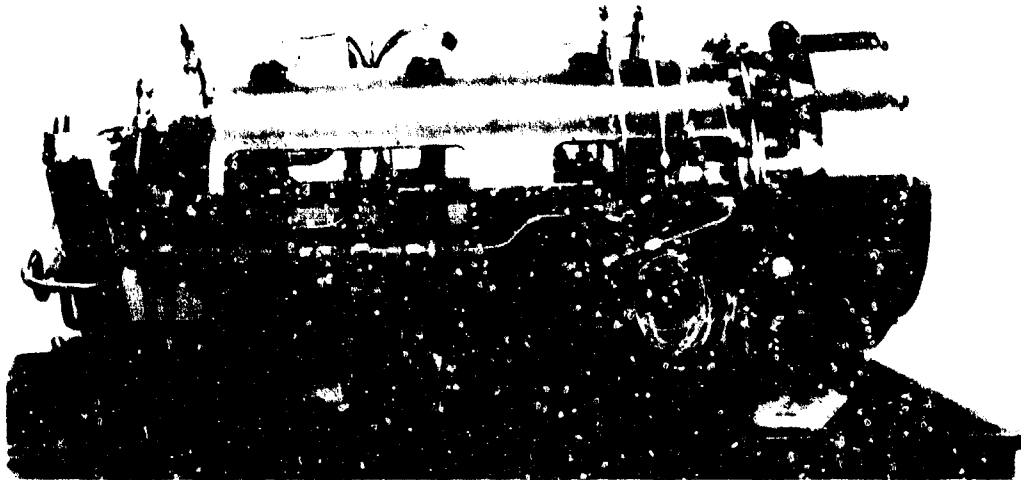
Figure 29. Synchronous Response Rig, Side View
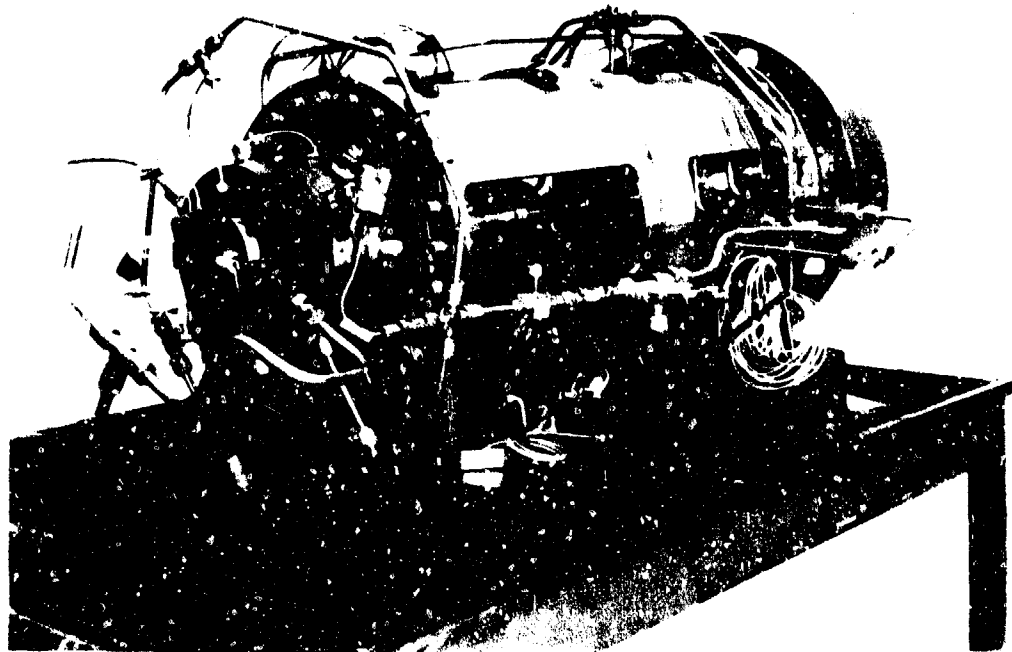
Figure 30. Synchronous Response Rig, Three-Quarter Rear View
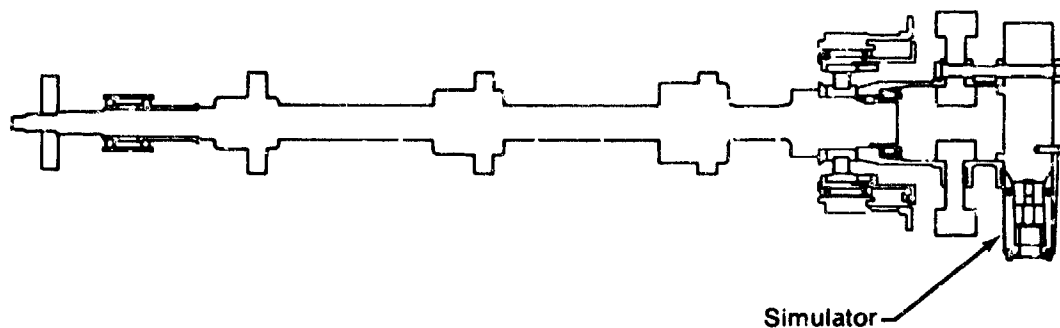
Simulator—

Figure 31. Synchronous Response Rig Schematic Diagram

Cantilevered from the roller bearing is the drive turbine from which the blade loss simulator disk is mounted, as shown in Figures 31 and 32. The blade loss mechanism consists of two release arms pivoted on a clevis. The arms were tied together holding the 1/3-oz in. weights which were released. The weights were released by cutting the tie string via a blade attached to a pneumatic actuator (Figure 33).

Figure 32. Synchronous Response Rig Showing Blade Loss Simulator Disk

B. RIG TEST

1. Test Program

The test instrumentation is depicted in Figure 34. It consisted of six pairs of proximity probes to determine whirl orbit at selected shaft locations. In addition, a set of accelerometers and proximity probes were used to measure the response of the viscous damper itself.

A strain gage located on the outer damper housing measured the load transmitted through the damper. The accelerometers placed on the calibrated squirrel cage bearing support allowed for the force measurement at the bearing support. The resultant force determined the magnitude of the bearing load.

All data was monitored via oscilloscope and recorded on magnetic tape for subsequent data reduction. A photograph of the test stand controls and instrumentation is shown in Figure 35.

The test program is outlined in Figure 36. An initial balance of the rig was followed by running the rig using three predetermined imbalances. For the three imbalances there were two changes in the viscous damper film thickness followed by one change in bearing support spring rate and a change-back to the initial film thickness. This series was followed by two supercritical and two subcritical blade loss simulations, incorporating two different bumper configurations.

50
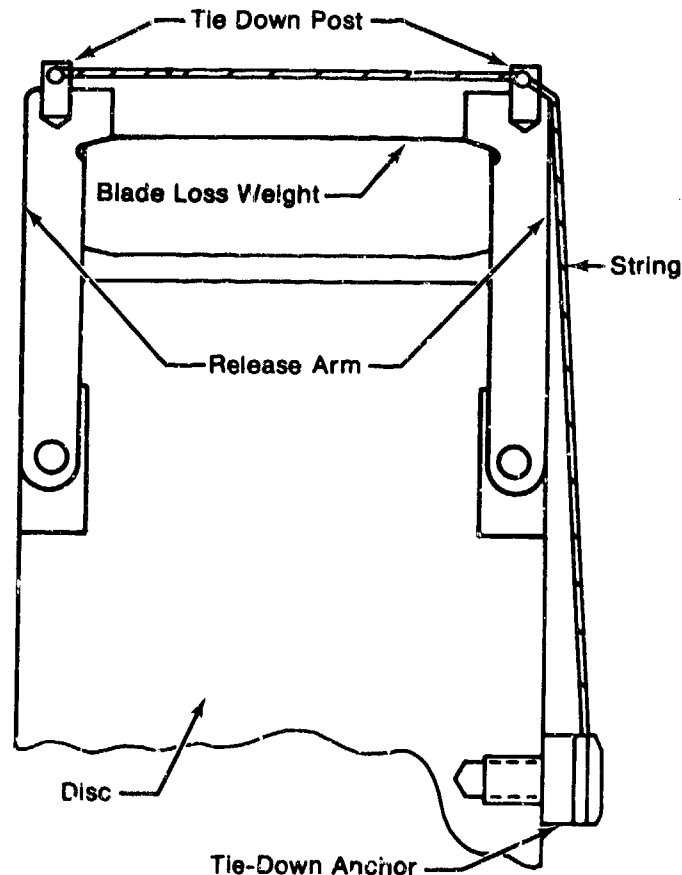
Figure 33. Blade Loss Release Mechanism

2. Test Results

The objective of the synchronous response rig test was to generate parametric experimental data to optimize the dynamic response of the rotor system under normal and abusive imbalance conditions such as the loss of a blade. Parameters such as bearing load and rotor displacement were measured as a function of imbalance, shaft speed, rotor-to-shroud clearance, bearing damper support flexibility, and damper clearance. Analytical correlation of these parameters with the experimental data is also shown.

The results of the parametric rig tests, builds 1 through 7, are presented in three categories: effect of imbalance and damper clearance, effect of bearing support stiffness and damper clearance, and effect of bumper clearance. The dynamic responses of four key rotor parameters are presented as a function of these three categories. The key parameters consist of the maximum dynamic response at the critical speed of the midspan shaft deflection, turbine-shroud relative deflection, bearing flexible support load, and damper load.
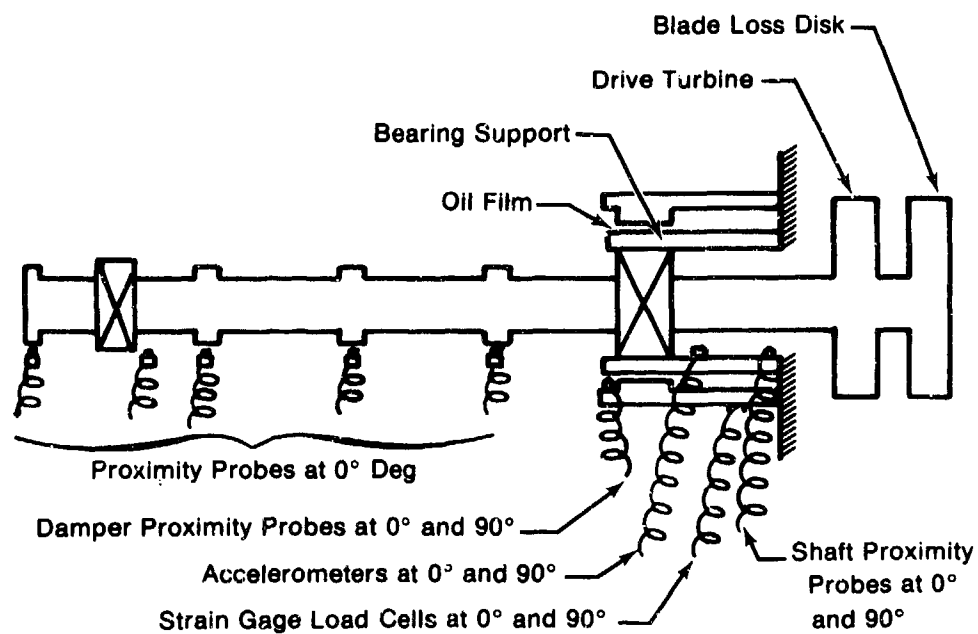
Figure 34. Synchronous Rig Instrumentation

Blade Loss Disk

Drive Turbine

Bearing Support

Oil Film

Proximity Probes at 0° Deg

Damper Proximity Probes at 0° and 90°

Accelerometers at 0° and 90°

Strain Gage Load Cells at 0° and 90°

Shaft Proximity Probes at 0° and 90°

Figure 35. Rig Test Stand Controls and Instrumentation

Turbine

Bumper Clearances A, B

Oil Film Thicknesses A, B, C

Bearing Support Springs A, B

RAD Clearance

4-in. Dia Damper	A = 0.006 in.
	B = 0.008 in.
	C = 0.010 in.
Bumper	A = 0.004 in.
	B = 0.006 in.
Support Stiffness	A = 85K lb/in.
	B = 42K lb/in.
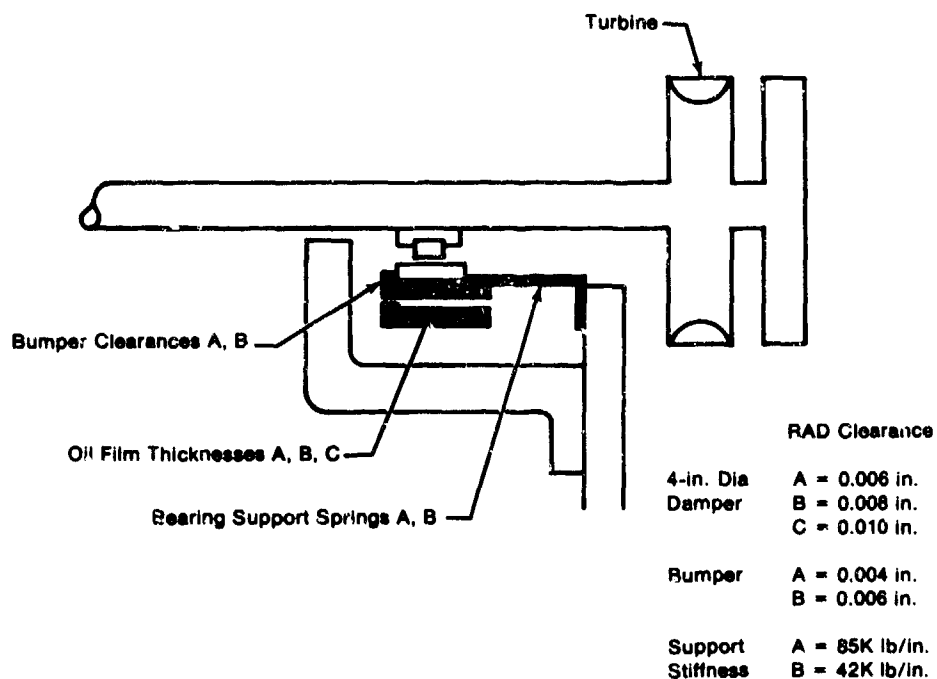
Build Number	Configuration			Run Description	Minimum Number of Runs
	Bumper	Film	Spring		
1	A	A	A	Balance	5
	A	A	A	Baseline, Unbalance A, B, C	4
2	A	B	A	Baseline, Unbalance A, B, C	4
3	A	C	A	Baseline, Unbalance A, B, C	4
4	A	C	B	Baseline, Unbalance A, B, C	4
5	A	B	B	Baseline, Unbalance A, B, C	4
6	B	B	B	Baseline, Unbalance A, B, C	4
	B	B	B	Subcritical Blade Loss	1
	B	B	B	Supercritical Blade Loss	1
7	A	B	B	Subcritical Blade Loss	1
	A	B	B	Supercritical Blade Loss	1

Figure 36. Task VII Test Program

The effects of imbalance and damper clearance on rotor dynamic response are shown in Figure 37, which summarizes the results of rig builds 1, 2, and 3. As expected, the rotor-bearing response increased with increased imbalance; however, the response was minimized with the largest damper clearance. This indicates that the higher damper forces generated with the lower clearances tend to limit the orbital motion in the damper, thus forcing more strain energy in the whirling shaft and reducing the effective damping. Although both the bearing loading loads and midshaft deflections increase with decreased clearance, the turbine shroud deflection was reduced slightly with the 0.006-in. clearance damper because the turbine is located near the damper where the orbital motion is forced to be limited. However, the 0.010-in. clearance damper reduced dynamic response of all four key rotor parameters. It should be noted that as the imbalance increases, the damper load increases at a faster rate than the hairpin load. This is an indication of the characteristic nonlinear force effects of the squeeze film damper. As the bearing deflection amplitude increases, the damper transmits more and more of the bearing load, reducing the load transmitted through the hairpin.

The effects of bearing support (hairpin) stiffness and damper clearance on rotor dynamic response are shown in Figure 38, which summarizes the results of rig builds 2, 3, 4, and 5. The most obvious result is that rotor response is reduced by reducing the bearing support (hairpin) stiffness. Reducing the stiffness allows an increase in orbital motion in the squeeze film damper, which increases effective damping and reduces vibration. The increase in damper load with decreased hairpin stiffness also indicates the increased damper motion. Again the minimum rotor response is observed when the largest damper clearance (0.010 in.) is used. These data clearly indicate that soft bearing supports in conjunction with wide damper clearances are a good combination for this flexible rotor rig.

The effects of bearing bumper clearance on the dynamics of a flexible rotor under transient blade loss conditions for both subcritical and supercritical speeds are shown in Figure 39. These plots are slightly different from the previous ones in that the peak transient response is displayed, as opposed to the peak steady-state response on the previous plots. The most significant result of the blade loss simulations is that the peak rotor transient response is reduced with increased bumper clearance. This indicates that as the bearing support strikes the bumper, high loads are transferred to the rotor and at this point the effectiveness of the damper is truncated because no further excursion into the damper film is permitted by the bumper. When the larger bumper clearance is used, more effective squeeze film damping is achieved and the bumper contact loads are reduced. This is also indicated by the decreasing hairpin load with decreased bumper clearance, because once the bumper is struck, the hairpin is relieved of an additional load and further load is transmitted through the damper support. Note the increased damper support load with decreased bumper clearance. Another observation of the blade-loss test results is that the rotor response amplitudes are always higher for supercritical rotor operation than for subcritical operation.

The scope of the test program was slightly expanded in order to investigate the effects of decelerating a supercritical rotor through its critical speed after a blade loss. The test was performed at the request of the Army Program Manager to verify that no severe damage would occur to an engine with supercritical speed shafting under blade loss conditions. This test differed from the previous supercritical blade loss test in that the rotor was not rebalanced by jettisoning a second balance weight before deceleration. Figure 40 shows the midshaft vibration amplitude of the rotor acceleration through the critical speed with only residual imbalance, then sudden blade loss and the deceleration back through the critical speed with the blade loss imbalance. Although the rotor rubbed bearing compartment seals, no structural damage to the rig was incurred.
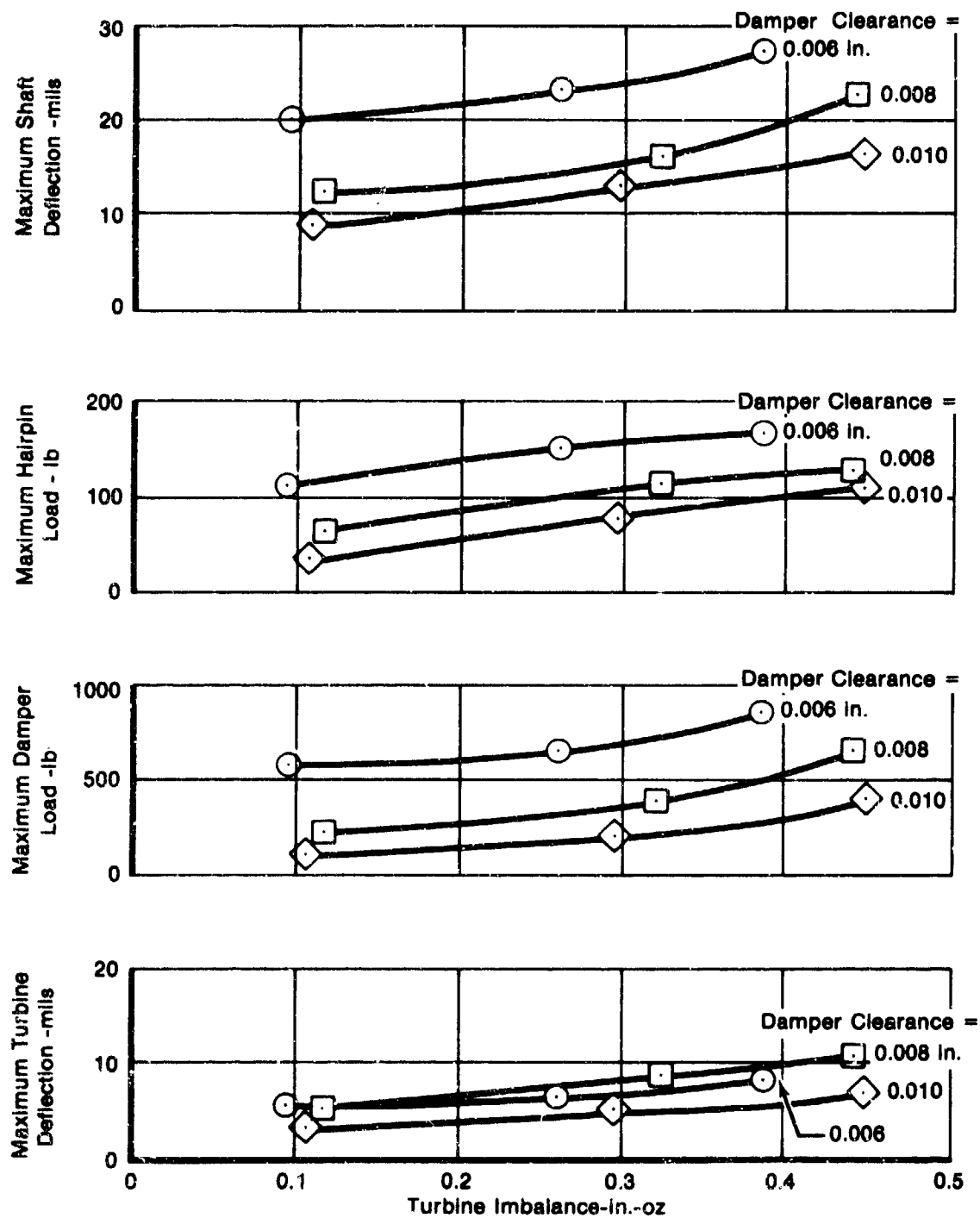
Figure 37. *Effect of Imbalance and Damper Clearance on Rotor Dynamic Response*
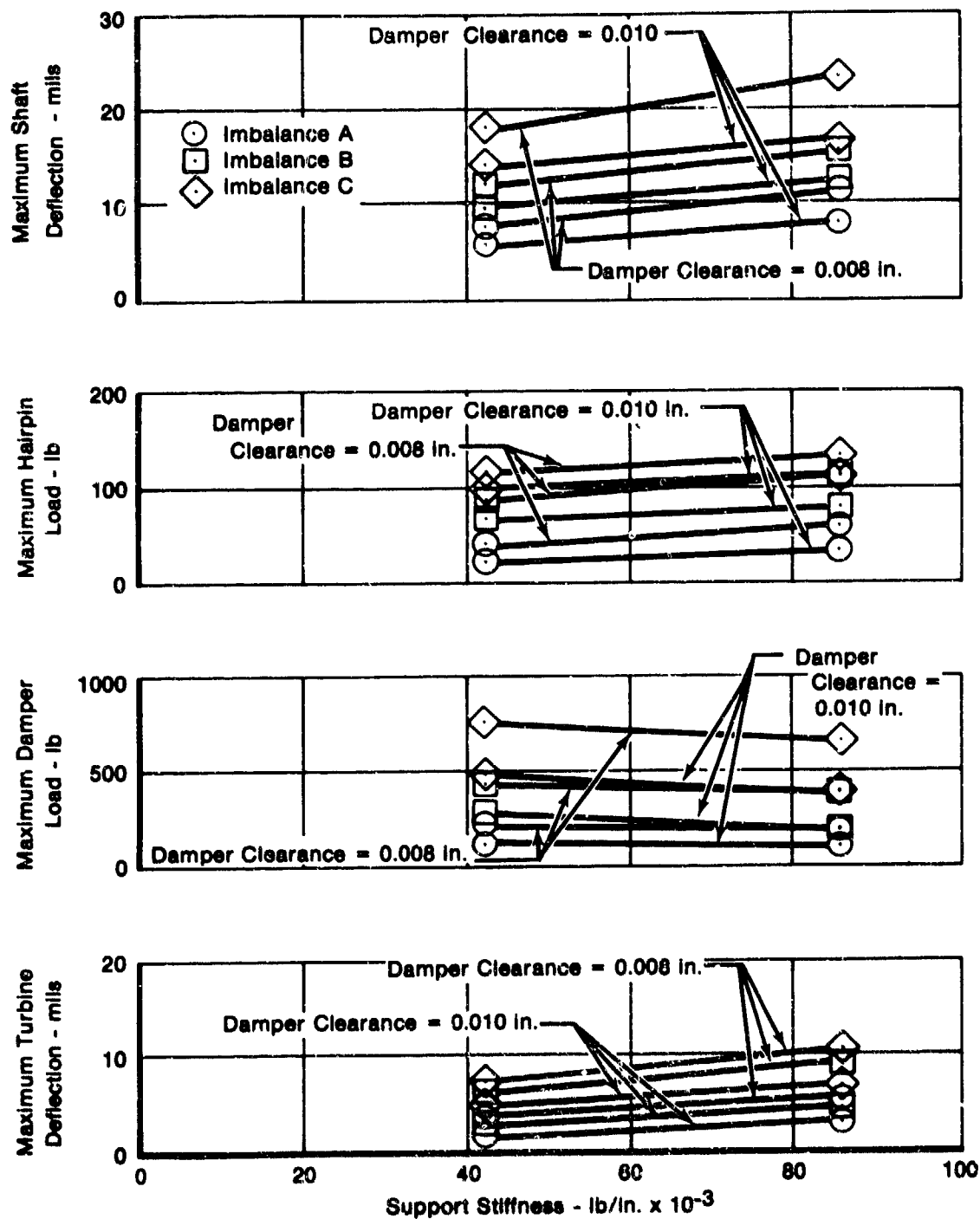
Figure 38. Effect of Bearing Support Stiffness and Damper Clearance on Rotor Dynamic Response
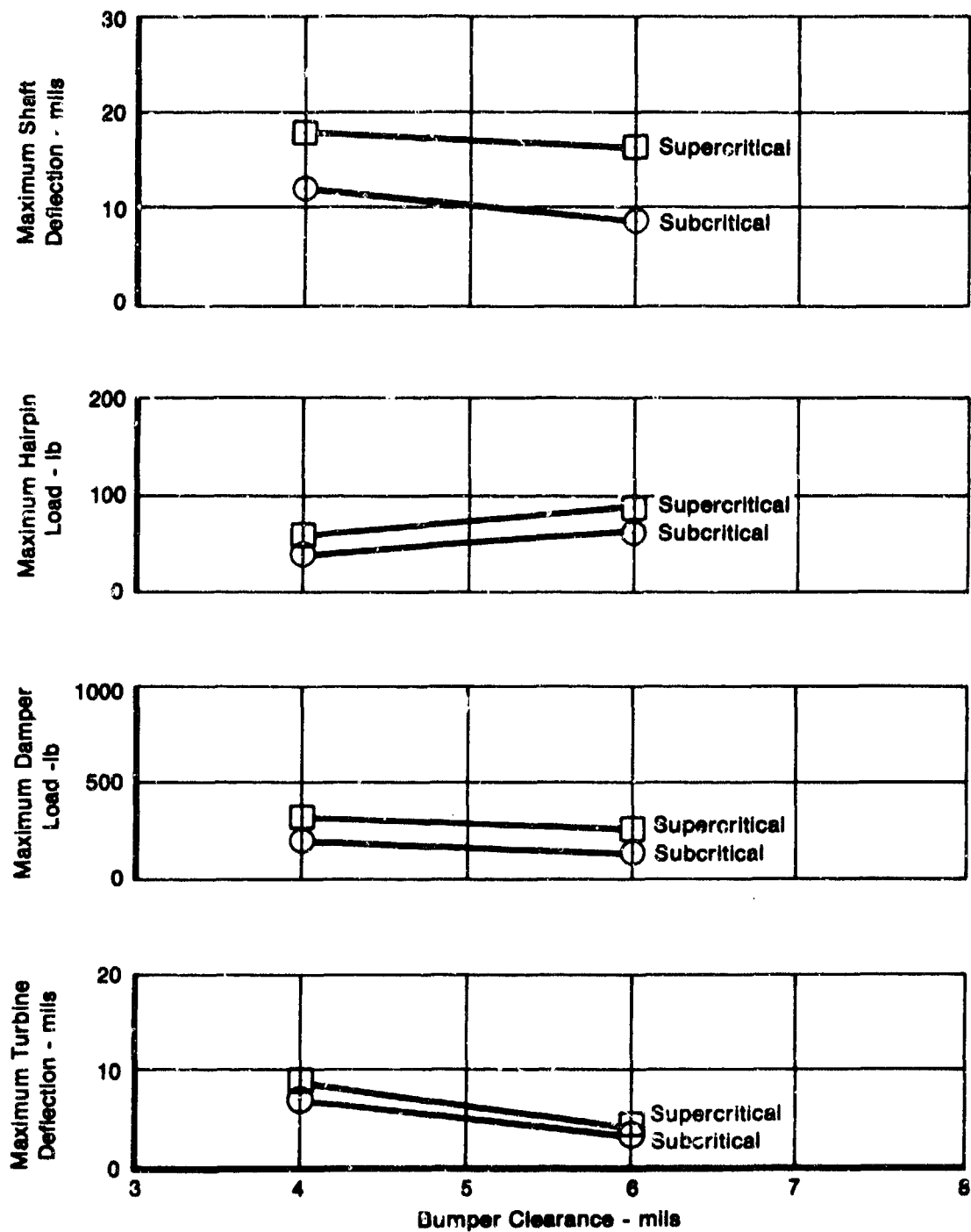
Figure 39. Effect of Bearing Bumper Clearance on Blade Loss Rotor Dynamic Response
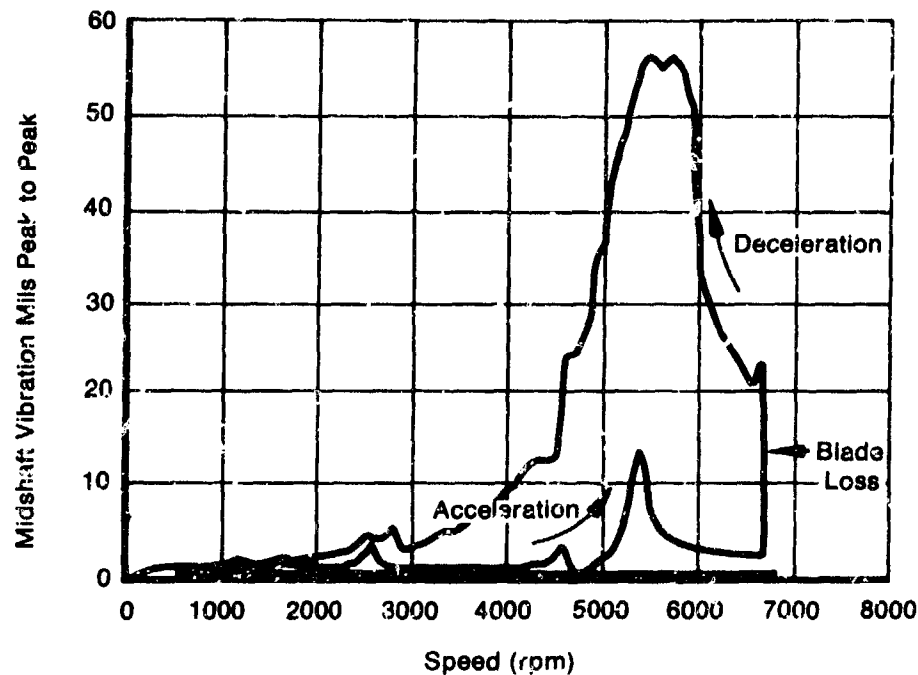
Figure 40. Midshaft Vibration Amplitude vs Speed

In summary, the parametric test program has been successful in giving a much better understanding of how variations in the most significant of rotor design parameters affect rotor response to synchronous dynamic excitation. The main results were that increased damper and bumper clearance, and decreased support (hairpin) stiffness, minimized the dyna· ·esponse of the flexible shaft rig. In engine applications, however, things such as maneuve: ompressor surge load deflections limit how "soft" the bearing support can be and how la. ᵗhe bumper clearance can be. The best combination of these parameters for optimum rotor performance is a function of the particular engine durability and efficiency requirements. Accurate analytical models of the rotor system are the most viable means of determining the best trade-off of all variables. The next section contains the comparison of analytical predictions of commonly used rotor dynamics computer programs with the flexible rotor rig test data.

C. DATA CORRELATION WITH ANALYTICAL MODEL

Two basic types of rotor dynamic response models were used to predict the dynamic response of the synchronous whirl rig. The first model was used to predict the rotor dynamic response to normal steady-state imbalance loads as were used in builds 1 through 6 of the test program. This model is the commonly used transfer matrix forced response computer program similar to that of Reference 10. The second model was used to predict the transient blade loss dynamics of the synchronous rig, builds 6 and 7 of this test program. This computer program used the well-known modal technique for calculating the transient response of large dynamic systems and is similar to that of Reference 11. Each of these mathematical models used the squeeze film damper mathematical model developed in Task I of this contract to predict the damper forces.

10 Lund, J. W., and Orcutt, F. K., "Calculations and Experiments on the Unbalance Response of a Flexible Rotor." ASME Paper No. 67-Vibr-27.

11 Dennis, A. J., Eriksson. R. H., and Seitelman, L. H., "Transient Response Analysis of Damped Rotor Systems by the Normal Mode Method," ASME Paper No. 75-GT-58.

The first step in predicting the dynamic response of a rotor system is to calculate the critical speed. The critical speed prediction aided in determining the severity of a natural rotor mode and the particular speed to concentrate on in predicting the steady-state forced response of the rotor. Calculation of the critical speed is also necessary because the predicted mode shapes and natural frequencies are used by the transient response model to predict the rotor deflections and forces due to transient loadings such as blade loss. Figure 41 shows the cross section of synchronous response rig and the corresponding beam model which was used to predict the critical speeds of the rig. The first three rig critical speeds are shown in Figure 42 along with the corresponding relative mode shapes and rotor strain energies. The 5000-rpm critical speed is the rotor mode that is being investigated throughout this test program. The 91% rotor strain energy in this mode indicates a very severe critical speed, because very little effective damping can be produced by the squeeze film damper when so little of the vibratory energy exists in the support system. Compared to current small engine standards, this program is an aggressive step forward in supercritical speed rotor development.

The next step in predicting the dynamic performance of a rotor system is to calculate the system response amplitude vs speed as a function of the applied load. The applied load for builds 1 through 5 of the synchronous whirl rig test program was an imbalance placed at the blade loss disk. A representative comparison of the predicted rig response to the measured response is shown in Figures 43 through 46. Shaft vibration sensitivity and bearing load sensitivity were chosen because of their influence on engine performance degradation and durability. The speed at which the peak amplitude of response occurred was predicted with good accuracy, and the average deviation of measured and predicted peak amplitudes was about 17%. Considering a combination of measurement and computation error, steady-state test data are in good agreement with prediction.

Computation error is calculated in terms of system energy error. This error is a function of the number of significant digits that can be maintained in a computer, and this numerical error can accumulate in some programs to the point where the predictions have considerable deviation from the exact values. The transfer matrix numerical method used in this report and in most steady-state rotor dynamic response programs is susceptible to accumulative round-off error. To assess the amount of numerical error that has been accumulated, comparison is made between the energy input to the dynamic system through the imbalance load and the energy dissipated out through the dampers. Ideally, these two quantities are equal. The percent difference between the energy "in" and the energy "out" is a good measure of the numerical error accumulated in predicting the system dynamic response. An average energy error of 1-3% was observed for the synchronous whirl rig imbalance response predictions. Energy errors of this magnitude are usually incurred when predicting the response of a very flexible rotor such as the one being studied, and the resulting prediction errors can be of significant magnitude. Therefore, numerical methods that eliminate the accumulation of round-off error should be applied to flexible rotor dynamic predictions.
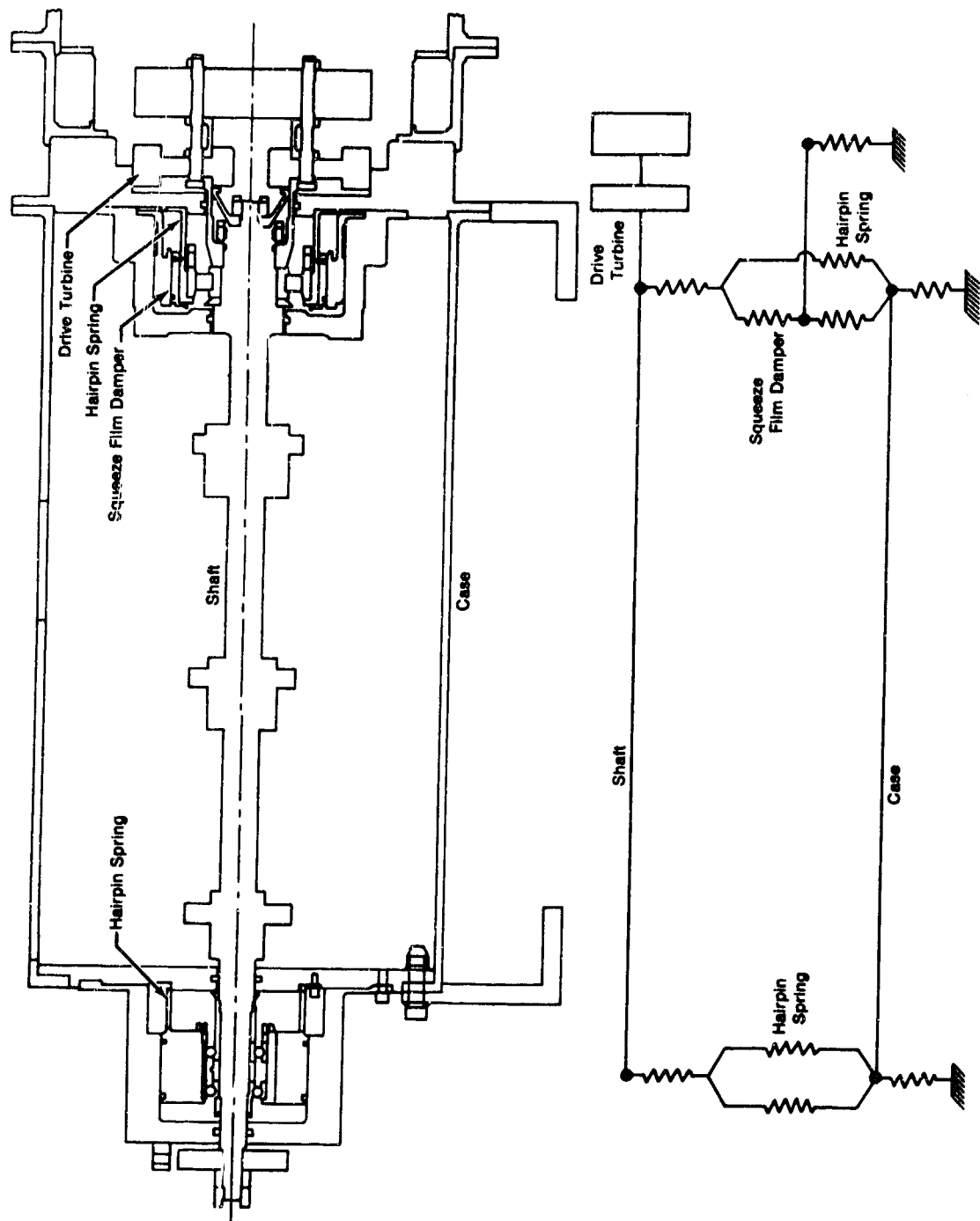
Figure 41. Synchronous Whirl Rig Model

5,032 rpm
91% Rotor Strain Energy

0

12,316 rpm
50% Rotor Strain Energy

0

20,146 rpm
9% Rotor Strain Energy

0
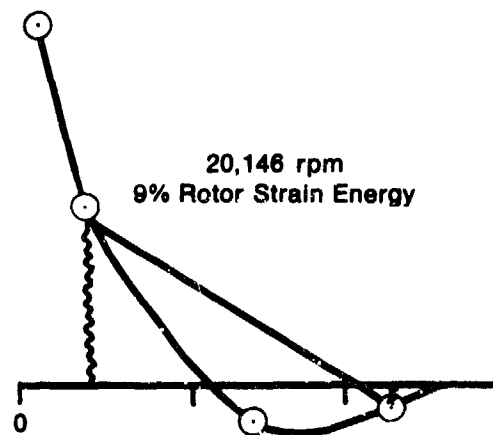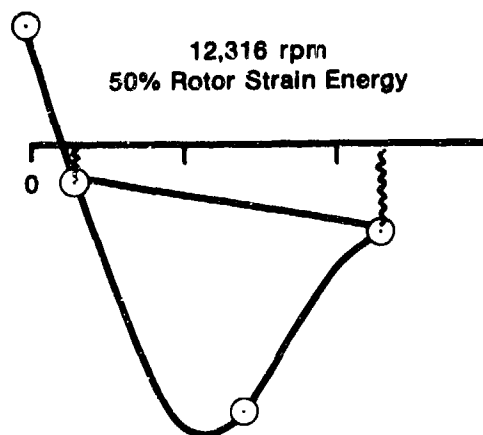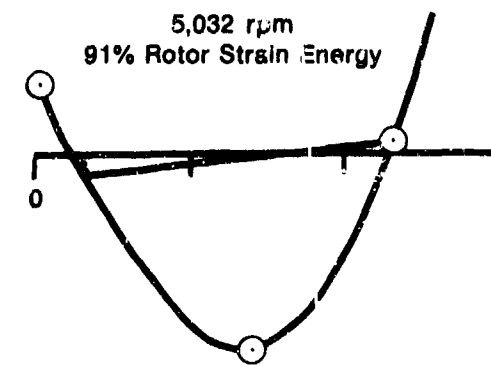
Figure 42. Synchronous Whirl Rig Critical Speeds and Mode Shapes
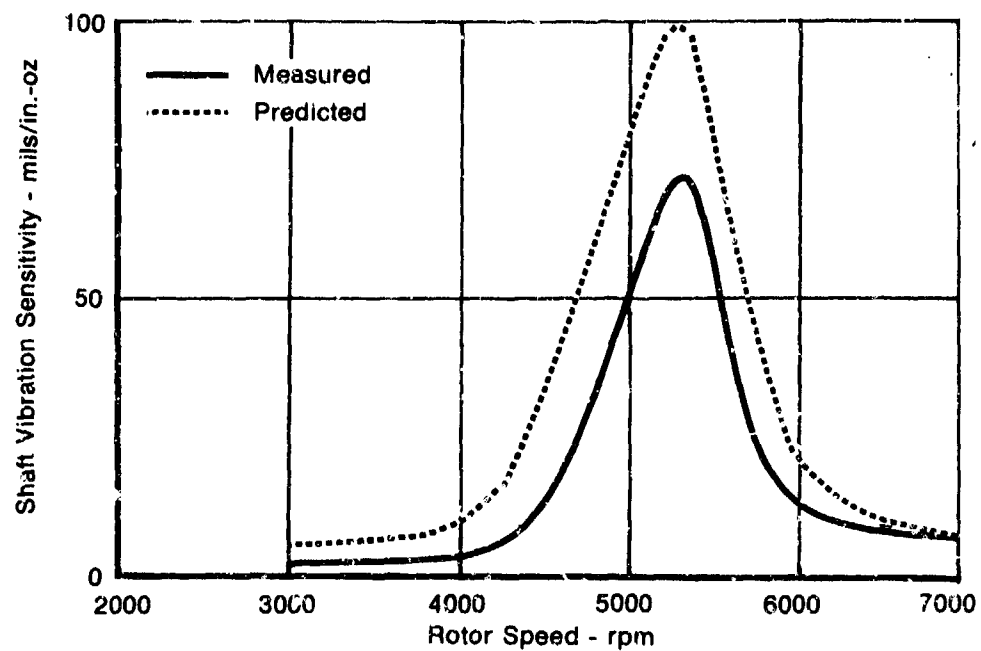
Figure 43. Shaft Sensitivity With Stiff Bearing Support (Build 3)
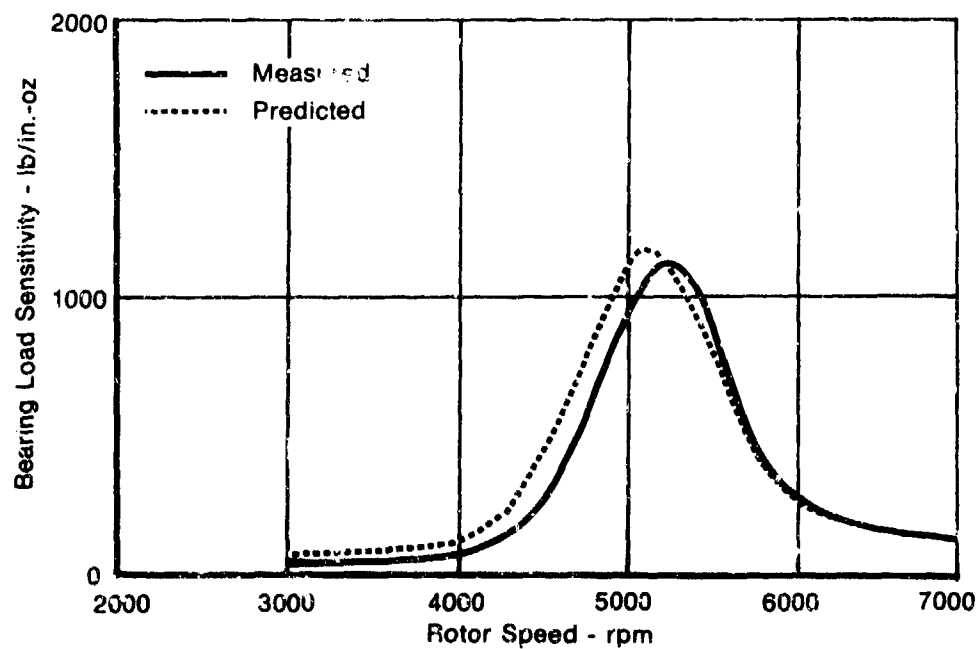
Figure 44. Bearing Load Sensitivity With Stiff Bearing Support (Build 3)
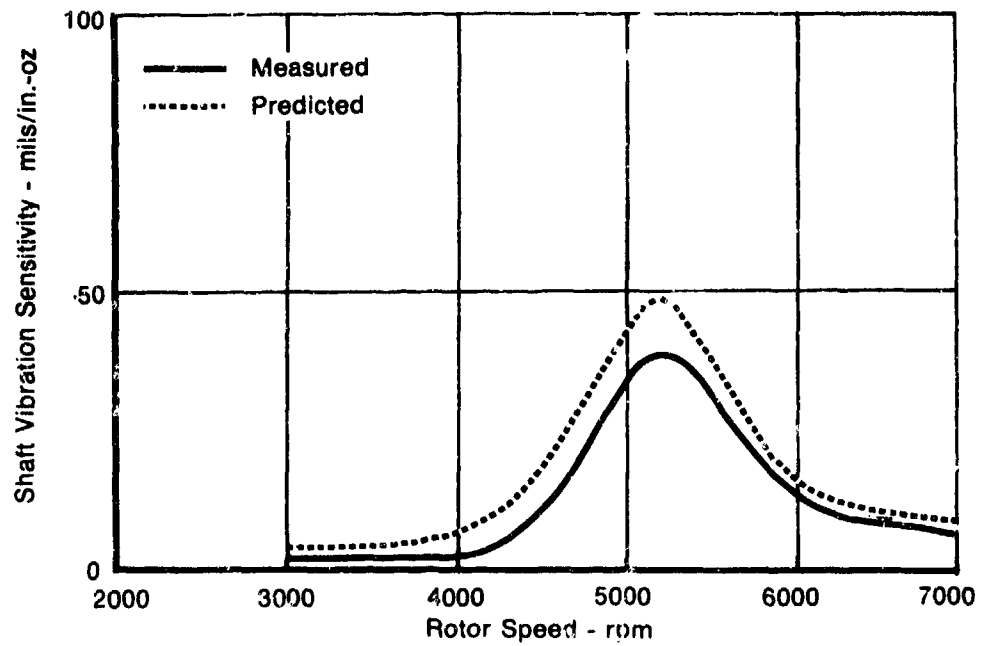
Figure 45. Shaft Sensitivity With Soft Bearing Support (Build 4)
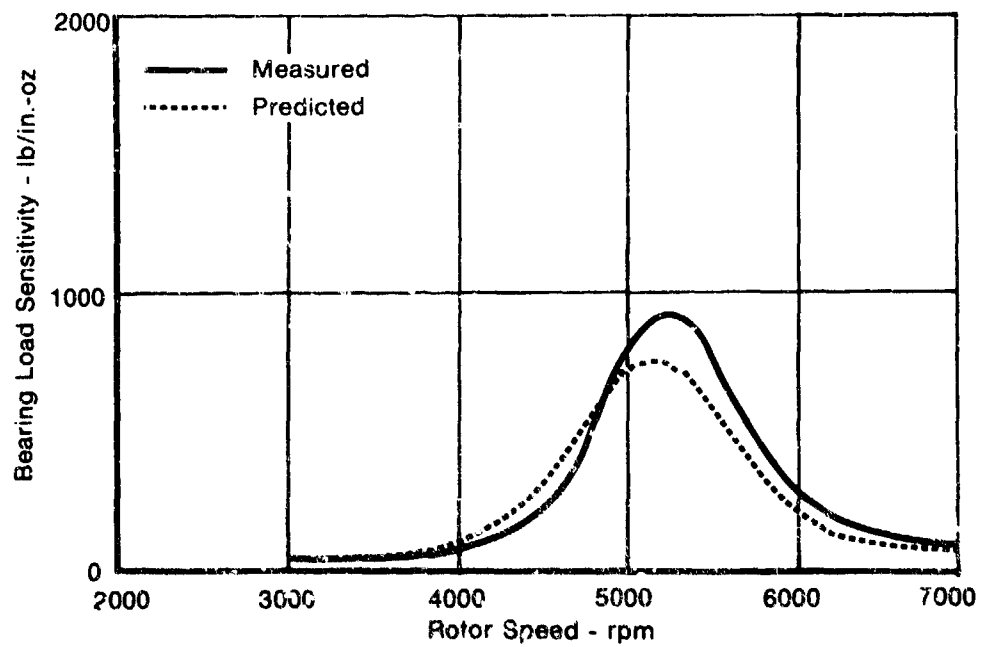
Figure 46. Bearing Load Sensitivity With Soft Bearing Support (Build 4)

63

The final two tests of this seven-part test program covered transient blade loss simulation at both subcritical and supercritical speeds. The measured data and predicted response of the build 6 run with the large bumper clearance are shown in Figures 47 and 48, the first figure showing the subcritical blade loss results and the latter figure the supercritical results. Figures 49 and 50 show the corresponding blade loss response plots with a small bumper clearance. All the responses are plotted vs time from the point of blade loss to steady state. The measured data are shown as a complete time trace, and the predicted results are shown as an envelope of peaks and are superimposed on the measured data. Note that both the measured and predicted curves show the beat frequency of excitation beating with the natural frequency of the rotor. The measured and predicted curves are similar in character, but in all cases the measured response is slightly higher than the predicted. Here again, normal measurement error and computational error can easily combine to give the differences shown.
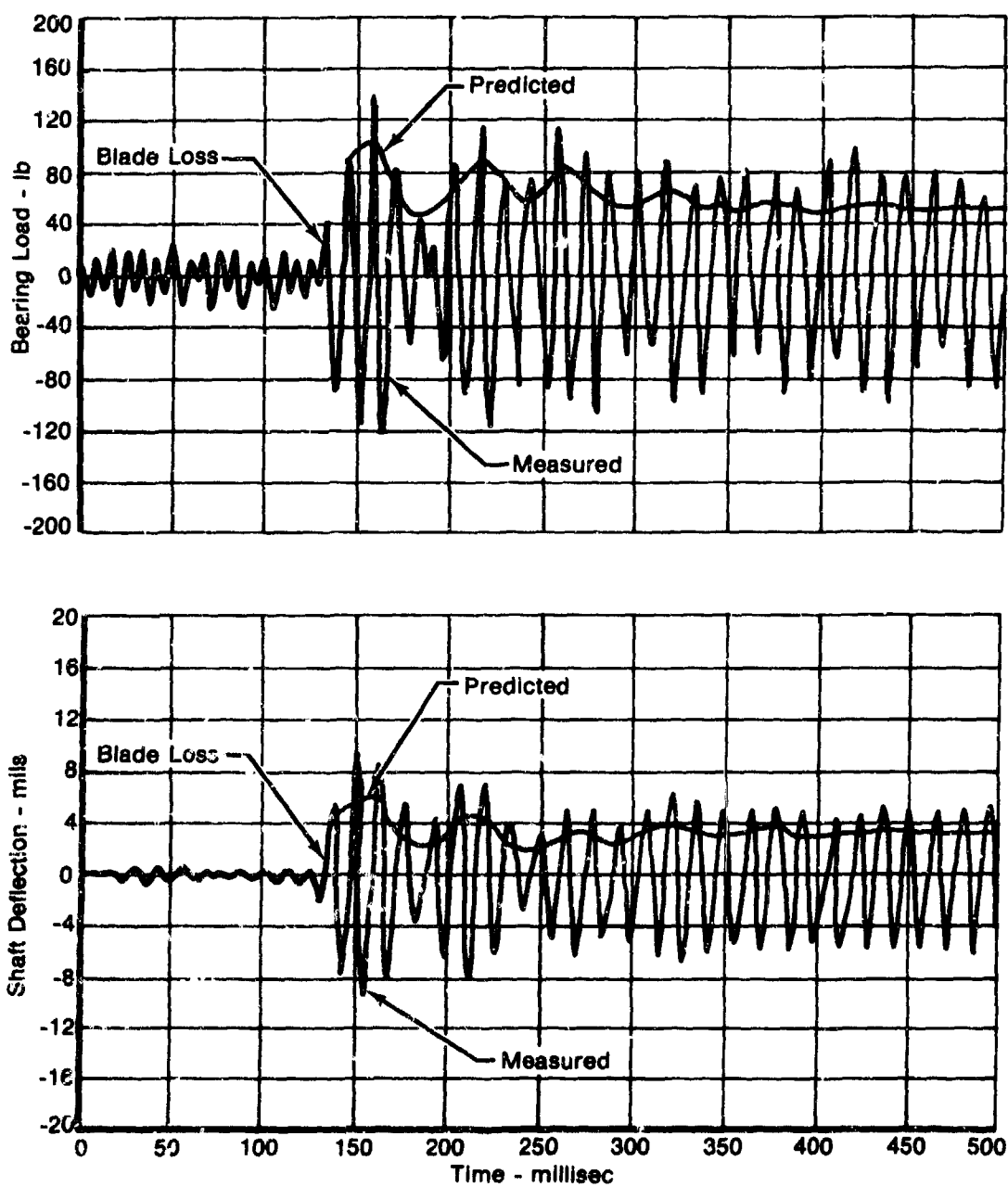
Figure 47. Subcritical Blade Loss Response (Large Bumper Clearance)
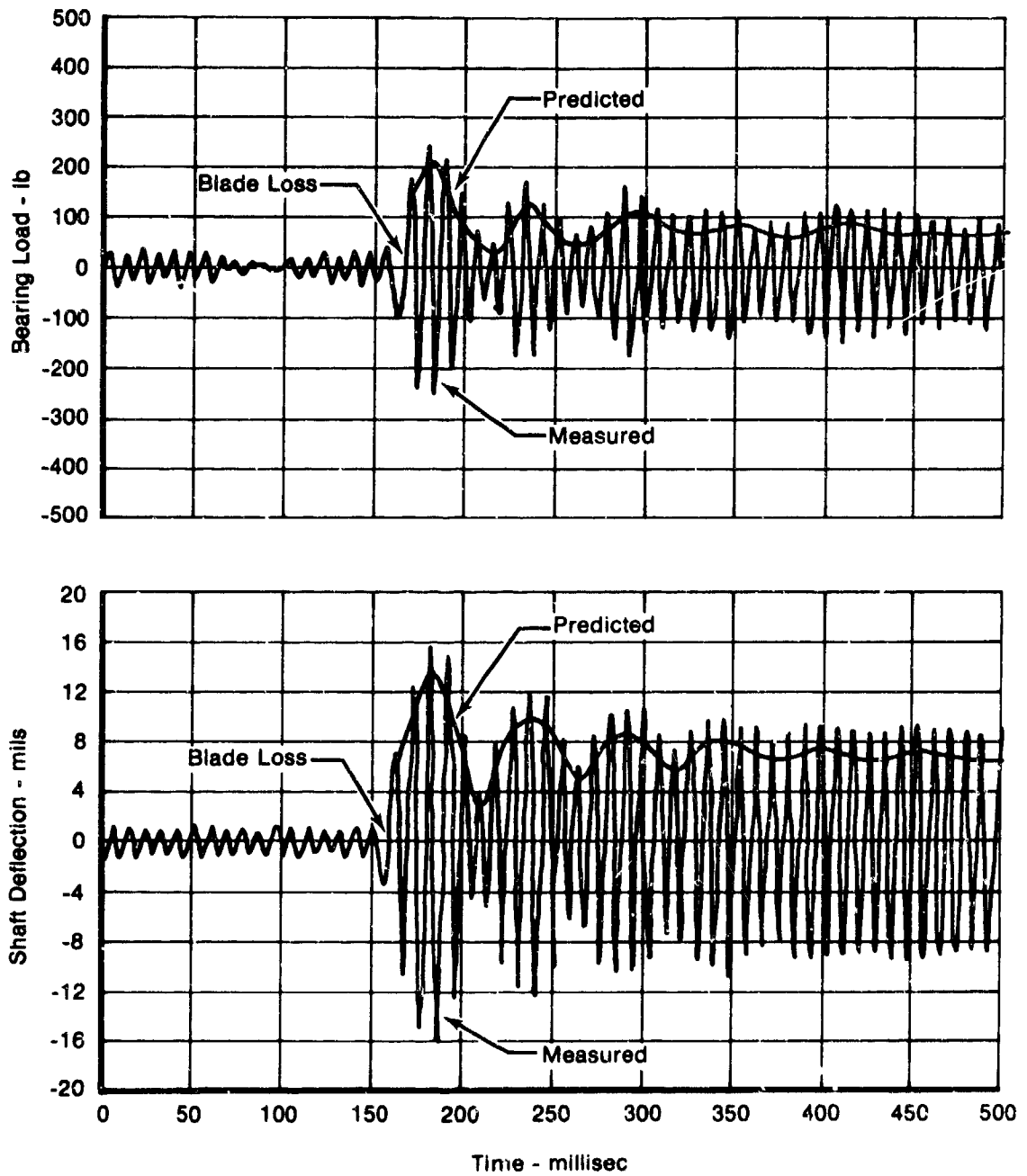
Figure 48. Supercritical Blade Loss Response (Large Bumper Clearance)
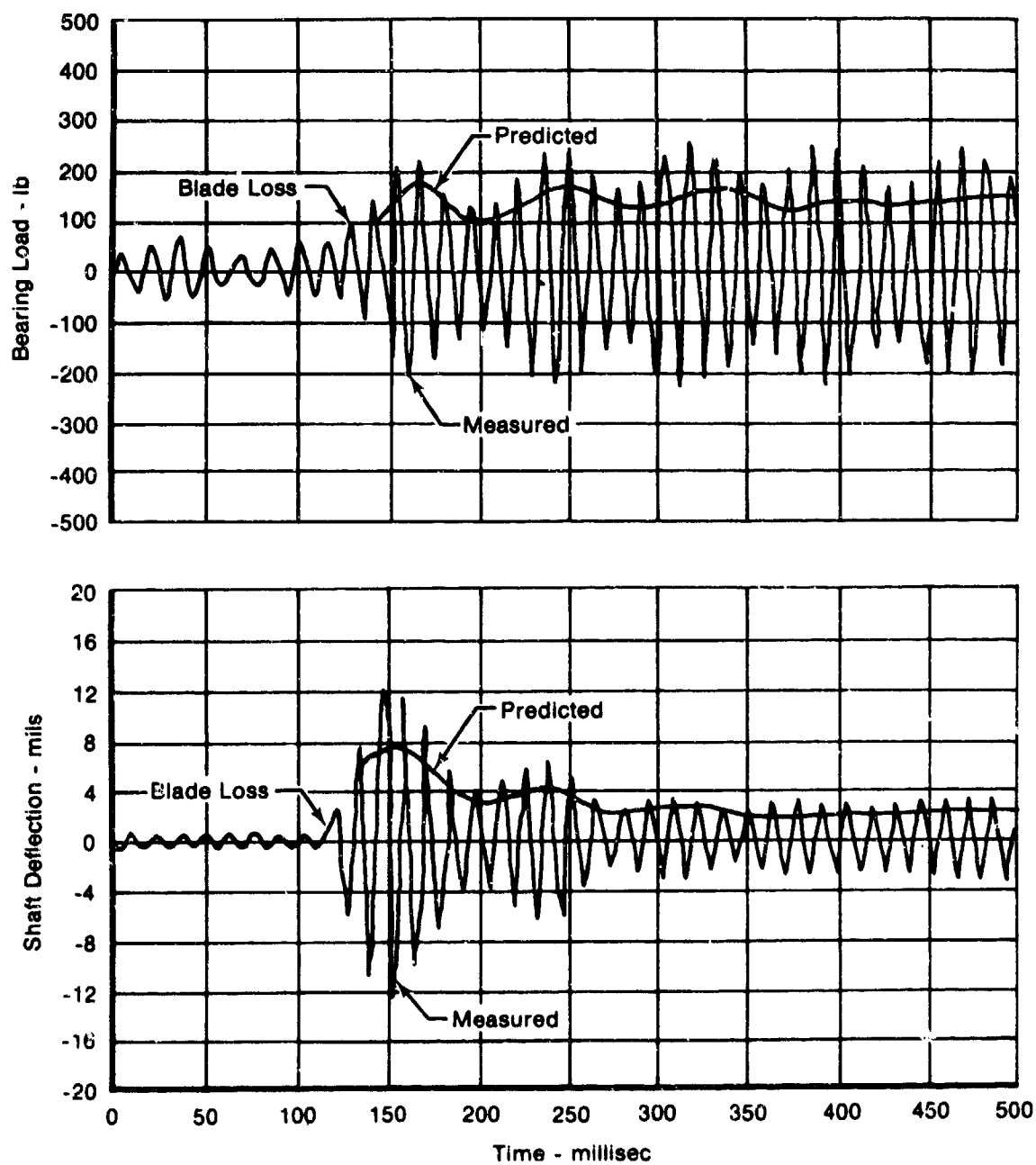
Figure 49. Subcritical Blade Loss Response (Small Bumper Clearance)
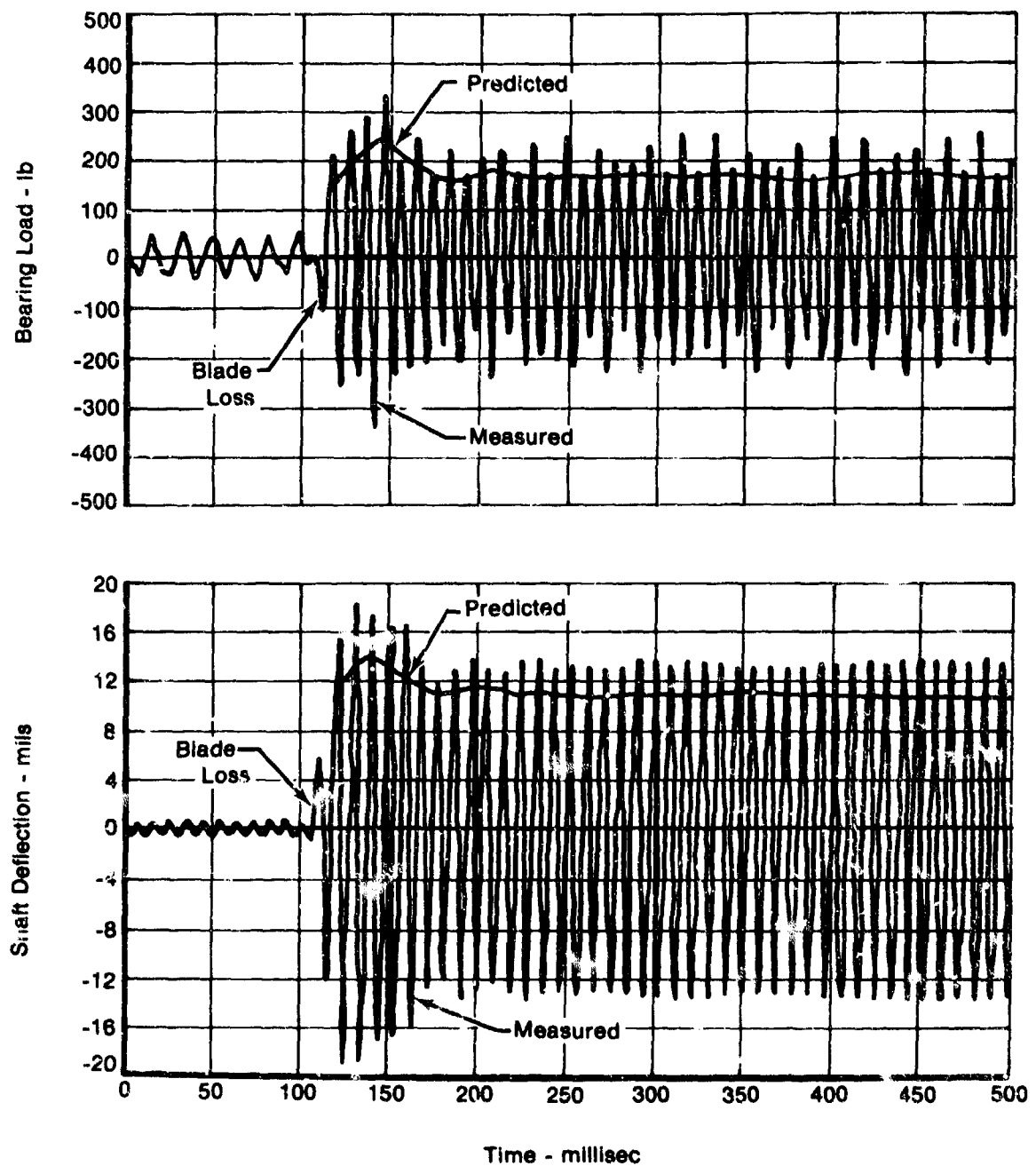
Figure 50. Supercritical Blade Loss Response (Small Bumper Clearance)

NONSYNCHRONOUS WHIRL RIG — ANALYSIS
FORMULATION AND VERIFICATION (TASKS VIII AND IX)

A. ANALYTICAL MODEL

1. Description

Spline couplings are commonly used in high speed rotating machinery to transfer power between adjacent shafts or within what is nominally one shaft for ease of assembly/disassembly. Normally, the two halves of these couplings are rigidly aligned and fixed with respect to each other by means of a pilot so that no relative motion is possible between adjacent spline teeth except that due to elastic deflection resulting from transmitted torque. This is not necessarily the case for unpiloted spline couplings. For this class of couplings, alignment in both radial and angular directions is provided solely by coupling geometry and close tolerances on the mating parts. In addition, no axial restraint exists. A particular application of an unpiloted spline coupling might be the connection between the power turbine shaft and transmission input shaft in a helicopter power train. For this case, the female coupling half is supported on bearings while the male half is integral with the turbine shaft which is only supported on bearings at its far end. Since the coupling is not solidly locked together, relative motion along several axes may occur between coupling halves. The forces generated by the friction between moving surfaces give rise to forces within the coupling which tend to destabilize the rotor system and can indeed cause instability if certain "favorable" conditions (for example, insufficient external damping) exist.

This problem has occurred in the past and is the subject of a paper by Williams and Trent (Reference 12), who explored the effects of asymmetry and nonlinearity in the supporting structure on spline-coupling-induced instability. Their study, however, assumed a rigid rotor and used an analog computer to simulate the rotor bearing system.

This report documents an analysis of unpiloted spline couplings. The coupling model thus derived can be incorporated into a rotor dynamics computer program to determine the stability of a rotor-bearing-spline coupling system.

In this report, the spline coupling is modeled as a section of the shaft system having internal damping. (For a further discussion of internal damping and its effects on stability, see Reference 13.) This model may then be incorporated as one portion of a rotor-bearing system model. The system stability may then be studied by computing the complex eigenvalues or damped natural frequencies of the system. Each damped natural frequency is a complex number wherein the imaginary part represents a frequency of oscillation of the system and the real part indicates stability. Positive or negative values for a real part indicate that the system will be unstable or stable, respectively, in that mode. A stability map (plot of real part against some parameter such as speed) or a Nyquist plot (real against imaginary part for various conditions) can then be drawn up covering the modes and operating conditions of interest. An overall picture of the stability of the system can thus be generated.

---

12 Williams, R., and Trent, R., "The Effect of Non-Linear Asymmetric Supports on Turbine Engine Rotor Stability," SAE 700320.

13 Lund, J. W., "Stability and Damped Critical Speeds of a Flexible Rotor in Fluid Film Bearings," Journal of Engineering for Industry, Trans. ASME, Series B, Vol. 96, No. 2, May 1974, pp. 509-517.

For each point in the analysis, the spline coupling model requires four coefficients: two stiffness and two damping terms. These coefficients are derived in Sections V.A.2.a and V.A.2.b, respectively, and are functions of spline geometry and coefficient of friction. Section V.A.2.c suggests an approach for stability calculation and offers guidance on the selection of coefficient of friction.

2. Method of Solution

a. Spline Coupling Stiffness

The stiffness of an unpiloted spline coupling may be calculated by first finding the stiffness of the individual coupling teeth for various loading conditions. The overall coupling stiffnesses in the lateral and angular directions are then found by properly combining the individual tooth stiffnesses. For this analysis, the following assumptions will be made:

- Except for a small localized area about the base of each tooth, the material on which the teeth are mounted is rigid. This implies that the deflection of the coupling results entirely from deflection of the teeth in rigid supports.

- All deflections are very small and all deflecting parts behave elastically.

- Where a given stiffness is nonlinear (nonproportional to deflection), it will be linearized about its value under steady-state operating conditions.

- Errors in tooth location and profile are small. Each tooth is in line contact with its mate, and all carry about the same load.

- The forces on the coupling teeth are due predominantly to the transmitted torque and forces arising from the misalignment itself (such as elastic restoring forces). Other forces, such as those resulting from friction-induced moments, are small.

The analysis for the individual tooth stiffness is similar to that in Reference 14, except for the Hertzian contact deflection term, which may be found in Reference 15.

Spline Tooth Stiffness — Tangential Direction

The stiffness of a spline tooth may be found by computing the deflection δ under load of a single tooth as the result of each of four mechanisms:

δ_B = displacement due to bending as a cantilever beam

δ_S = displacement due to shear deformation as a cantilever beam

δ_R = displacement due to tooth rotation as a rigid body in the supporting structure at its base

δ_C = displacement due to Hertzian contact deformation of the tooth surface

14 Laskin, I., et al., "Analysis of Noise Generated by UH-1 Helicopter Transmission," USAAVLABS Technical Report 68-41, June 1968, Available through Clearinghouse, Springfield, Va. 22151, Report No. AD 675458.

15 Walowit, J. A., and Anno, J. N., "Modern Developments in Lubrication Mechanics," Applied Science Publishers, Ltd. London, 1975.

Displacement due to transverse shear of the supporting structure and radial compression of the tooth are neglected (the latter for tangential stiffness only). The displacements will then be used to find tooth compliance resulting from each mechanism. The individual compliances are then simply added and the result is inverted to yield the tooth stiffness.

To calculate δ_B and δ_S, the spline tooth will be treated as a sequence of transverse sections, each of uniform rectangular cross section. The depth of each segment is the average of the depths at the ends of the segment, as shown in Figure 51. In this figure, y_k represents the distance from the tooth surface to its centerline at radius r_k, r_p is the pitch radius, P is the applied load, and ψ is the angle from the horizontal of the applied load.
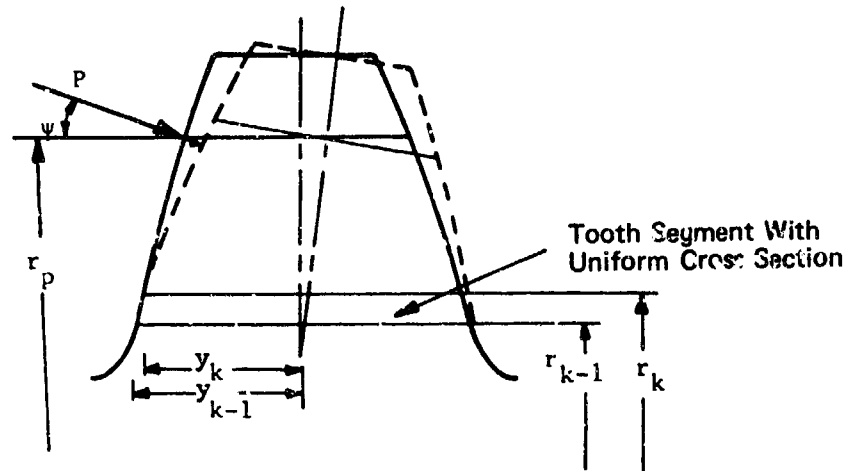
Figure 51. Deflection of a Spline Tooth

Deflection Due to Bending

The second moment of area of a tooth cross section at radius r_k is expressed as:

$$I_k = \frac{1}{12}\ l(2\ y_k)^3 = \frac{2}{3}\ l\ y_k^3 \tag{28}$$

where l is the length of the tooth face. At radius r_{k-1}, at the other end of the tooth segment, the second moment of area is

$$I_{k-1} = \frac{2}{3}\ l\ y_{k-1}^3 \tag{29}$$

For the assumed cross section, the mean of the two second moments of area will be used:

$$I_k = \frac{I_k + I_{k-1}}{2} \tag{30a}$$

or

$$I_k = \frac{l}{3}\ (y_k^3 + y_{k-1}^3) \tag{30b}$$

The average area $\bar{A}_k$ of the segment can be found in a similar manner, resulting in

$$\bar{A}_k = l \, (y_k + y_{k-1}) \tag{31}$$

The height of segment k may be found from the radius at either end of the segment:

$$h_k = r_k - r_{k-1} \tag{32}$$

Each of the above equations, (30b) (31), and (32), is applied to every segment on the tooth, both on the involute curve and at the tooth root.

The distance of the kth segment, at its outer end, from the point of load application is found to be

$$S_k = r_p - r_k \tag{33}$$

where the face width of the spline is large compared with the tooth thickness; the extra width contributes an added stiffening effect to the teeth. This may be incorporated into the bending deflection equation through use of the factor $(1-\nu^2)$, where ν is Poisson's ratio. Normally, this appears in the numerator while the modulus of elasticity E appears in the denominator. For convenience, the $(1-\nu^2)$ factor will be applied as a correction to the modulus E to yield a corrected value E_ν, which is defined as follows:

$$E_\nu = \frac{E}{1-\nu^2} \tag{34}$$

Should the spline teeth be relatively narrow compared with their thickness, the correction factor should be dropped.

In Figure 51, the load, P, acts in two ways to load the cantilevered spline tooth:

1. A concentrated load equal to the transverse component of the applied load, $P \cos \Psi$.

2. A moment load equal to the radial component of the applied load times one-half the thickness of the tooth at the point of load application, $Py_p \sin \Psi$.

In tooth bending, each of these load conditions causes a transverse displacement and rotation of the tooth centerline under the point of load application. These two displacements will be evaluated for each of the two load conditions and then combined.

Figure 52 portrays, in its simplest form, a tooth segment subjected to a transverse load applied some distance away. The rest of the tooth serves as a rigid support or a rigid extension.

72
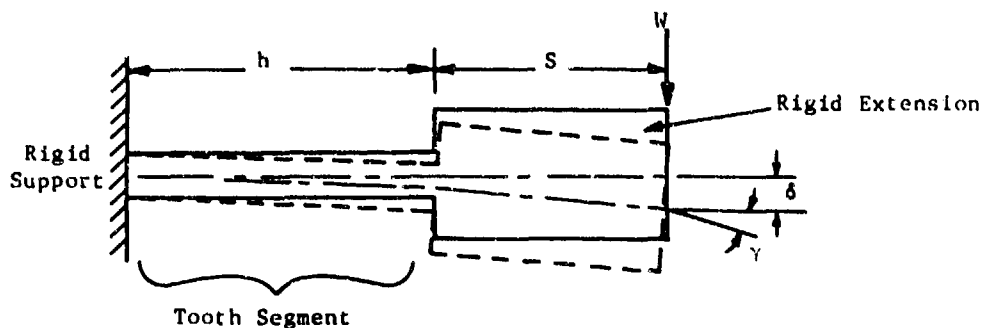
Figure 52. Bending of a Tooth Segment Subjected to a Transverse Load

From standard beam deflection analysis, the transverse deflection δ_1 and centerline rotation γ_1 at the load are

$$\delta_1 = \frac{Wh}{3\ EI}\ (h^2 + 3Sh + 3S^2) \tag{35}$$

$$\gamma_1 = \frac{Wh}{2\ EI}\ (h + 2S) \tag{36}$$

The two equations can be rewritten using the terminology of the main analysis, so that for a segment k,

$$(\delta_{Bk})_1 = \frac{Ph_k\ \cos\Psi}{3\ E_\nu\ I_k}\ (h_k^2 + 3\ S_k\ h_k + 3\ S_k^2) \tag{37}$$

$$(\gamma_{Bk})_1 = \frac{Ph_k\ \cos\Psi}{2\ E_\nu\ I_k}\ (h_k + 2\ S_k) \tag{38}$$

The other case in tooth bending, shown in Figure 53, considers a tooth segment subjected to a moment load applied some distance away, with the rest of the tooth serving as a rigid support or extension.
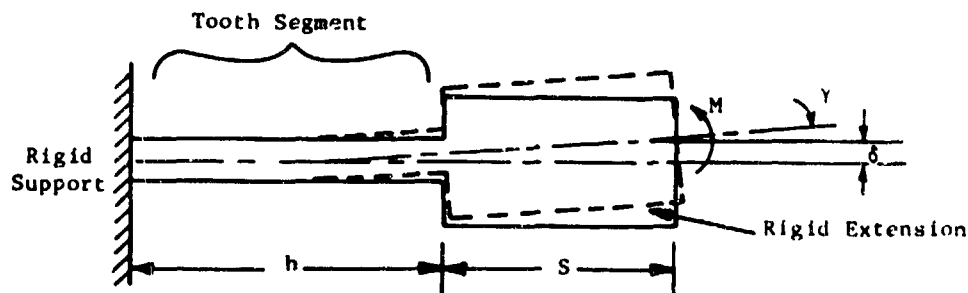
Figure 53. Bending of a Tooth Segment Subjected to a Movement

73

Again, from beam deflection analysis, the transverse deflection δ_2 and centerline rotation γ_2 at the load are

$$\delta_2 = -\frac{Mh}{2\,EI}\,(h + 2S) \tag{39}$$

$$\gamma_2 = -\frac{Mh}{EI} \tag{40}$$

The minus sign is applied because, with a moment applied in the direction shown, the deflections are opposite those described in the previous case. Again, Equations (39) and (40) may be rewritten using the main terminology and thus become

$$(\delta_{Bk})_2 = \frac{-Py_p\,h_k\,\sin\Psi}{2E_\nu\,I_k}\,(h_k + 2\,S_k) \tag{41}$$

$$(\gamma_{Bk})_2 = \frac{-Py_p\,h_k\,\cos\Psi}{E_\nu\,I_k} \tag{42}$$

The deflections for each tooth segment are next summed by rewriting Equations (37), (38), (41), and (42) with the summation covering all segments from the base of the tooth to the point of the applied load.

$$(\delta_B)_1 = \frac{P\cos\Psi}{2\,E_\nu}\sum_k \frac{h_k}{I_k}\,(h_k^2 + 3\,S_k\,h_k + 3\,S_k^2) \tag{43}$$

$$(\gamma_B)_1 = \frac{P\cos\Psi}{2\,E_\nu}\sum_k \frac{h_k}{I_k}\,(h_k + 2\,S_k) \tag{44}$$

$$(\delta_B)_2 = \frac{-Py_p\,\sin\Psi}{2E_\nu}\sum_k \frac{h_k}{I_k}\,(h_k + 2\,S_k) \tag{45}$$

$$(\gamma_B)_2 = \frac{-Py_p\,\sin\Psi}{2E_\nu}\sum_k \frac{h_k}{I_k} \tag{46}$$

These displacements are combined by considering each load condition separately. The results will then yield the total displacement in bending. Figure 54 shows the geometry from which the relationships between the various displacements may be found.

From Figure 54 we see that

$$\overline{JD} = \overline{JC} - \overline{DG} \tag{47}$$

Hence,

$$\overline{JD} = \frac{\overline{JJ}}{\cos\Psi} = \frac{\delta_J}{\cos\Psi} \tag{48}$$

74

where δ_j is the displacement of the tooth outline in the direction of the applied force. Next we see that

$$\overline{JG} = \overline{CC'} = \delta_y \tag{49}$$

where δ_y is the transverse displacement described above. Vector DG can be found by the relations

$$\overline{DG} = \overline{GG'} \tan \Psi \tag{50}$$

$$\overline{GG'} = \overline{GC'} (\angle GC'G') \tag{51}$$

$$\overline{GC'} = \overline{JC'} = y_p \tag{52}$$

where y_p is half the tooth thickness at the pitch radius and angular rotation ($\angle GC'G'$) is found to be

$$\gamma = (\angle GC'G') \tag{53}$$

which is described by Equations (44) and (46). Combination of Equations (47) through (53) yields

$$\frac{\delta_B}{\cos \Psi} = \delta_y - y_p \, \gamma \tan \Psi \tag{54}$$

where δ_B is the total motion of point J along the line of force due to bending of the tooth. Equation (54) can be simplified by multiplying through with $\cos \psi$.

$$\delta_B = \delta_y \cos \Psi - y_p \, \gamma \sin \Psi \tag{55}$$
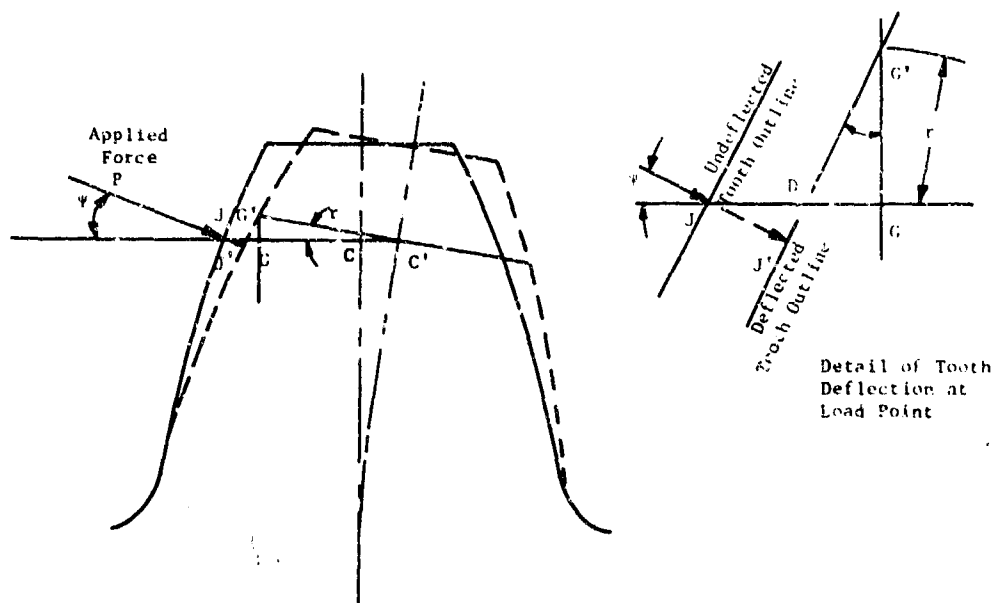
Figure 54. Tooth Bending Geometry

76

Equation (55) may now be used to combine the individual displacements. For the concentrated load condition, Equations (43) (44), and (55) are combined to get

$$(\delta_B)_1 = \frac{P}{E_\nu} \left[\frac{\cos^2 \Psi}{3} \sum_k \frac{h_k}{I_k}(h_k^2 + 3 S_k h_k + 3 S_k^2) \right.$$

$$\left. - \frac{\cos \Psi \sin \Psi}{2} y_p \sum_k \frac{h_k}{I_k} (h_k + 2 S_k) \right] \tag{56}$$

Similarly, for the moment load condition, Equations (45), (46), and (47) are combined to yield

$$(\delta_B)_2 = \frac{P}{E_\nu} \left[- \frac{\cos \Psi \sin \Psi}{2} y_p \sum_k \frac{h_k}{I_k} (h_k + 2 S_k) \right. \tag{57}$$

$$\left. + y_p \sin^2 \Psi \sum_k \frac{h_k}{I_k} \right]$$

Lastly, the two can be combined to give the total deflection due to bending:

$$\delta_B = (\delta_B)_1 + (\delta_B)_2 \tag{58}$$

Deflection Due to Shear

The shear deflection of the spline tooth as a cantilever beam is caused by the same transverse component of the applied load, namely $P \cos \Psi$. Deflection of this type simply offsets the centerline without rotating any transverse section. The total deflection then becomes the sum of the deflections for each of the previously defined tooth segments. Figure 55 represents a flexible segment subjected to shear, with the remainder of the tooth serving as a rigid support or extension.
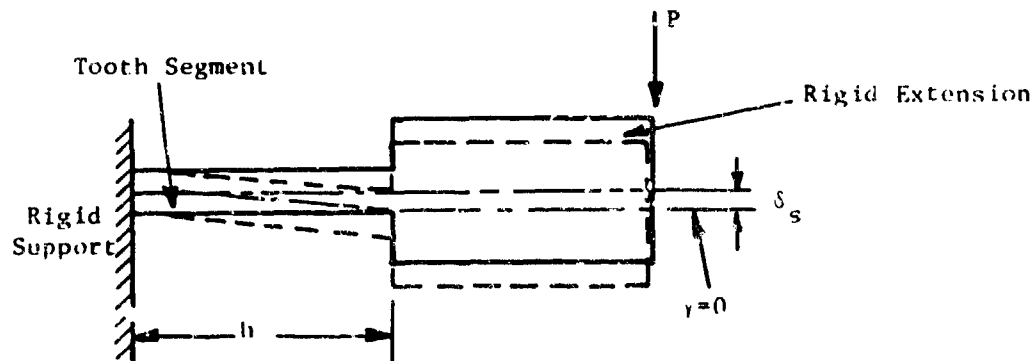
Figure 55. Shear Deflection of Tooth Segment

Using standard analytical methods, the transverse deflection for a segment with a rectangular cross section is

$$\delta = \frac{1.2\ Ph}{GA} \tag{59}$$

where h is the segment length, G is the shear modulus, A is the area, and 1.2 is a shear form factor for a rectangular cross section. As noted previously, the centerline rotation at the load is

$$\gamma = 0 \tag{60}$$

When the above equations are rewritten using the proper terminology, the result is

$$(\delta)_k = \frac{1.2\ Ph_k\ \cos\Psi}{G\ \bar{A}_k} \tag{61}$$

$$(\gamma_s)_k = 0 \tag{62}$$

Equation (61) is then summed over all segments k to find the deflection for the entire tooth in shear:

$$(\delta_s) = \frac{1.2\ P\ \cos\Psi}{G}\ \sum_k\ \frac{h_k}{\bar{A}_k} \tag{63}$$

To obtain the displacement in the direction of the load, Equation (63) is substituted into (64):

$$\delta_s = \frac{1.2\ P\ \cos^2\Psi}{G}\ \sum_k\ \frac{h_k}{\bar{A}_k} \tag{64}$$

Deflection Due to Rotation in Elastic Support

Rotation of a spline tooth as a rigid body in its elastic supporting structure is a third contributor to the overall deflection. The moment M causing the rotation results from multiplication of the transverse component of the applied load by the moment arm S_p:

$$M = P\ S_p\ \cos\Psi \tag{65}$$

where S_p is the distance from the applied load to the base of the tooth. Figure 56 shows the loading and its resultant deflection in schematic form

According to Reference 16, the equation for rotation at the load is

$$\gamma = \frac{1.327\ M}{E\ y_d^2\ l} \tag{66}$$

which means that the displacement at the load is

$$\delta = \gamma\ S = \frac{1.327\ M\ S}{E\ y_d^2\ l} \tag{67}$$

16 O'Donnel, W. J., "Stress and Deflection in Built-In Beams," ASME Paper No. 62-WA-16, 1962.

Replacing the variables in Equation (67) with those of the main analysis, we get

$$(\delta_R) = \frac{1.327\ P\ (S_p \cos \Psi - y_p \sin \Psi)\ S_p}{E_\nu\ y_R^3\ \ell} \tag{68}$$

where y_R is the half-width of the tooth at its root and M has become

$$M = P\ (S_p \cos \Psi - y_p \sin \Psi) \tag{69}$$

Likewise for the rotation:

$$(\gamma_R)_1 = \frac{1.327\ P\ (S_p \cos \Psi - y_p \sin \Psi)}{E_\nu\ y_R^3\ \ell} \tag{70}$$

The resulting displacement of the tooth outline in the direction of the load is found by substituting Equations (68) and (70) into (55):

$$\delta_R = \frac{1.327\ (S_p \cos \Psi - y_p \sin \Psi)^2}{E_\nu\ y_R^3\ \ell} \tag{71}$$
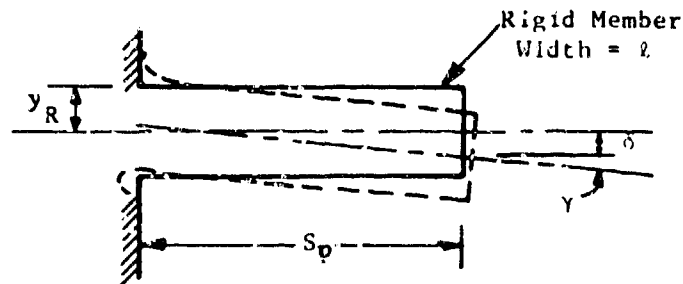
Figure 56. *Tooth Displacement Due to Rotation at Base*

The above equations have been derived with the external spline tooth in mind. However, the same equations apply for the internal spline tooth as long as the values for h and S are kept positive and as long as the summation of the k segments proceeds between the base of the tooth and the load point.

Conversion to Compliance

Equations (58), (64), and (71) may be rewritten to express a compliance, or deflection per unit load, which is defined as

$$Q = \frac{\delta}{P} \tag{72}$$

Thus, for the bending case, Equation (58) becomes

$$Q_B = \frac{1}{E_P} \left[\frac{\cos^2\Psi}{3} \sum_k \frac{h_k}{I_k} (h_k^2 + 3 S_k h_k + 3 S_k^2) \right.$$

$$\left. - y_p \cos\Psi \sin\Psi \sum_k \frac{h_k}{I_k} (h_k + 2 S_k) + y_p^2 \sin^2\Psi \sum_k \frac{h_k}{I_k} \right] \quad (73)$$

For shear, Equation (64) becomes

$$Q_s = \frac{1.2 \cos^2\Psi}{G} \sum_k \frac{h_k}{A_k} \quad (74)$$

and for rotation in the support, Equation (71) becomes

$$Q_R = \frac{1.327 (S_p \cos\Psi - y_p \sin\Psi)^2}{E_p y_R^3} \quad (75)$$

The total compliance of the tooth acting as a beam is simply the sum of the above compliances:

$$Q_{Beam} = Q_B + Q_s + Q_R \quad (76)$$

The above holds true for the total compliance of the mating tooth, which may be found independently.

Hertzian Contact Deformation

The last displacement to be considered in the tangential direction will be that due to contact deformation. If the surface radii of the mating teeth are different enough from each other, such that the width of the contact zone is much smaller than the depth of the tooth, the contact displacement can be considered Hertzian. If the radii are close or the same, such that after initial "run in" contact is expected to occur over a wide area of the tooth, then the deformation is no longer Hertzian and will be treated after the Hertzian case. For cases where contact deformation is due to Hertzian contact deformation, the treatment used in this analysis is based on Reference 15 for cylindrical surfaces in "line contact." Figure 57 shows two infinitely long cylindrical surfaces in the unloaded and loaded conditions.

The two surfaces are assumed to have radii of curvature R_1 and R_2. Unfortunately, the solution for the absolute deformation of two infinitely long cylinders in line contact is unstable. However, a solution does exist for the change in length from the surface to a point in each cylinder remote from the surface. If the distances from the undeformed surfaces of cylinders 1 and 2 to remote interior points are d_1 and d_2, the contractions of d_1 and d_2 as load is applied are defined to be δ_{H1} and δ_{H2} (Figure 57), which must be much smaller than d_1 and d_2, respectively. Additionally, d_1 and d_2 must be much larger than the contact patch width b. If P is defined as the load per unit of axial length, the contraction δ_{H1} of each surface is given by

$$\delta_{H1} = \frac{2P}{\pi} \frac{1-\nu_1}{E_1} \left(\ln \left[\frac{2 d_1}{b} \right] - \frac{1}{2} \cdot \frac{\nu_1}{(1-\nu_1)} \right) \quad (77)$$

where the contact patch width b is given by

$$b = 2 \sqrt{\frac{PR}{\pi} \left[\frac{1-\nu_1^2}{E_1} + \frac{1-\nu_2^2}{E_2} \right]} \qquad (78)$$

and the equivalent radius R is

$$R = \frac{R_1 R_2}{R_1 + R_2} \qquad (79)$$

Substitution of Equation (64) into (78) simplifies it to

$$b = 2 \sqrt{\frac{PR}{\pi} \left[\frac{1}{E_{\nu 1}} + \frac{1}{E_{\nu 2}} \right]} \qquad (80)$$

Equation (77) may be converted to a compliance by dividing both sides by the force P and substituting Equation (34):

$$Q_{H1} = \frac{2}{\pi E_{\nu i}} \left(\ln \left[\frac{2d_i}{b} \right] - \frac{1}{2} \frac{\nu_1}{1-\nu_1} \right) \qquad (81)$$

The above equation shows that the compliance is not constant but is somewhat dependent on the applied load and the location from which the contraction δ_i is measured. It will be assumed for this analysis that distance d_i can be set equal to the half-width y_{pi} of the tooth at the pitch line. Since the dependence of compliance on load is not large, an average tooth load will be found and then assumed to be constant as long as changes in displacement are not too great.
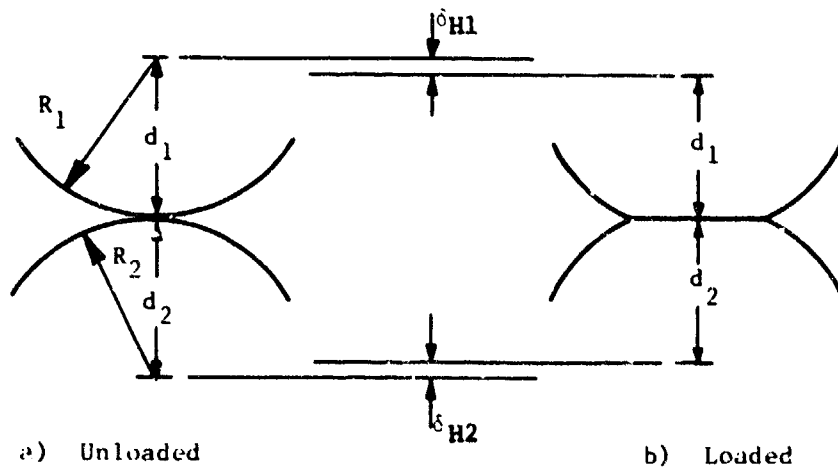
Figure 57. Hertzian Contact Deflection of Two Cylindrical Surfaces

For cases where the deformation cannot be considered Heitzian, the deflection due to contact pressure will be approximated by testing the tooth as a member in compression. The classical equation describing the deflections of a rod in compression is

$$\delta = \frac{P\ell}{AE} \tag{82}$$

where P is the applied force, ℓ is the length of the rod, and A and E are the area and the elastic modulus, respectively. The compliance Q is then

$$Q = \frac{\delta}{p} = \frac{\ell}{AE} \tag{83}$$

For our case, ℓ will be taken to be the half depth y_p of the tooth at the pitch diameter, the modulus becomes E_ν to take account of plane strain, and the area is approximated by length ℓ of the tooth face times the width w_c of the contact patch. Hence, for one tooth, i of a pair, L

$$Q_{H1} = \frac{y_p}{w_c \ell E_\nu} \tag{84}$$

The subscript for Q will be the same as for the Hertzian case, as the two cases are mutually exclusive.

In summary, the elastic compliance of a pair of mating teeth due to a load acting through the tooth flanks is the sum of the individual compliances:

$$Q_T = Q_{B1} + Q_{S1} + Q_{R1} + Q_{H1} + Q_{B2} + Q_{S2} + Q_{R2} + Q_{H2} \tag{85}$$

The stiffness of the pair of teeth is then the inverse of the compliance:

$$k_T = \frac{1}{Q_T} \tag{86}$$

Spline Tooth Stiffness — Radial Direction

The deflection of a spline tooth in the radially inward direction may be found by again splitting the tooth into segments, finding the deflection of each segment to a given force and summing them over the height of the tooth. Figure 58 shows the geometry of a spline coupling tooth loaded radially in compression.

The equation for the deflection of the kth segment having thickness h_k and area A_k (see Equations (31) and (32)) is

$$(\delta_c)_k = \frac{Ph_k}{A_k E_\nu} \tag{87}$$

which is found using standard analytical methods. The deflection for the entire tooth is then simply the sum of the deflection of each individual segment:

$$\delta_c = \frac{P}{E_\nu} \sum_k \frac{h_k}{A_k} \tag{88a}$$

81
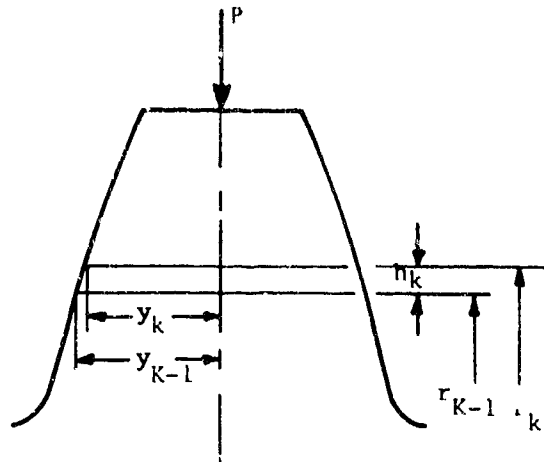
Figure 58. Individual Tooth Loaded in Compression

The compliance Q_c is then found to be

$$Q_c = \frac{\delta_c}{P} = \frac{1}{E_\nu} \sum_k \frac{h_k}{A_k} \tag{88b}$$

Since the tooth for this mode of deflection is in direct contact with the material at the root of the mating tooth, the compliance due to Hertzian contact deformation must be included. Equations (79), (52), (80), (53), and (81) may be used for this purpose. Since the assumed contracting cylinders are now concentric, the larger of the two radii in Equation (79) and (52) must be negated to yield a correct equivalent radius term, and distances d_i are set equal to the tooth height and half the depth of its mating piece. As before, some average value will be assumed for load P in Equation (81). The total radial compliance is thus

$$Q_{Radial} = \frac{1}{E_\nu} \sum_k \frac{h_k}{A_k} + \frac{2}{\pi} \sum_{i=1}^{2} \frac{1}{E_{\nu i}}$$

$$\left(\ln\left[\frac{2d_i}{b} \right] - \frac{i}{1-\nu_i} \right) \tag{89}$$

As before, if the radii of the two mating pieces are the same, the Hertzian term of Equation (89) is dropped.

The stiffness k_R is simply the inverse of Equation (89):

$$k_R = \frac{1}{Q_{Radial}} \tag{90}$$

Spline Coupling Stiffness

Computation of the stiffness of a spline coupling involves both lateral and angular stiffness. The lateral stiffness term refers to stiffness along a radial direction passing through the shaft centerline, while the angular stiffness term refers to rotational stiffness about an axis perpendicular to the centerline, not to torsional stiffness. In addition, the stiffnesses are different for each of the two types of couplings considered in this analysis, namely diameter fit and side fit unpiloted splines, as shown in Figure 59.
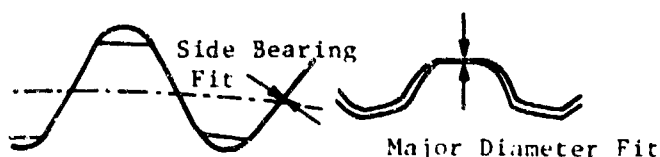
Figure 59. Two Types of Spline Couplings

Both types of couplings rely on close tolerances, either on tooth width (side fit) or on the major diameter for radial and angular locations. Since location is not provided for any other means (a pilot, for example), the lateral and angular stiffnesses may be found from a knowledge of the spline coupling geometry and the tooth stiffnesses. The latter have already been derived, while for the former the basic method employed will be to consider each tooth as an individual spring and subject the teeth to some defined displacement as shown in Figure 60.
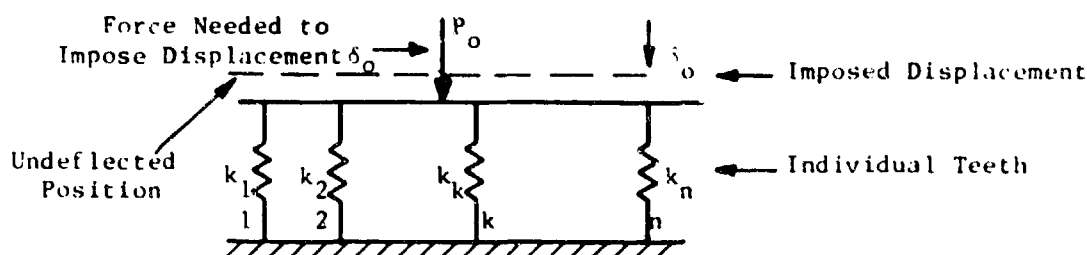
Figure 60. Model of Spline to Determine Overall Stiffness

The force exerted by the individual teeth in the direction of the load may then be calculated and, hence, the overall stiffness found. Using this method, the variation in tooth stiffness with applied load can be accommodated, either by computing the force separately for each tooth by iteration or using an approximate applied force.

Radial Stiffness — Major Diameter Fit

For teeth loaded on their outer edge, the displacement of the teeth radially inward will be found by using the model shown in Figure 61.
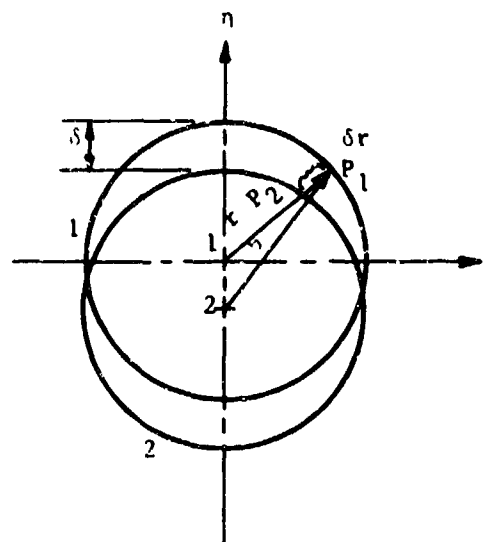
Figure 61. Model to Determine Tooth Displacement

Consider the outer edges of the external (or male) spline teeth as describing a circle of radius r. This is circle number 1 of Figure 61. Circle number 2 coincides with the major diameter of the internal (female) spline, that is, the diameter at the roots of the spline teeth. The two circles are initially coincident, so that the external spline tooth tips just touch the internal spline tooth roots (Figure 59). Circle number 2 is next given a downward displacement δ. Since, except for Hertzian deformation of the contact zone, the external and internal spline members are assumed rigid, each of the teeth will be compressed inward by some amount, depending on its location.

The distance δr represents the radial compression inward of a tooth at angle θ on the periphery of circle number 1. For small values of displacement, δr can be closely approximated by the equation

$$\delta_r \cong \delta \sin \theta \qquad\qquad 0 \leq \theta \leq \pi \qquad\qquad (91)$$

The normal force generated by the tooth is the product of tooth stiffness k_R and the displacement δr:

$$P_R = k_R \delta_r \qquad\qquad (92)$$

where stiffness k_R is found from Equation (90). The contribution to the force parallel to the η axis (i.e., in line with the original displacement) is then

$$P_\eta = P_R \sin \theta \qquad\qquad (93)$$

84

In order to find the total force along the η axis we must sum all the individual tooth forces P_n. If there are n teeth in the region $0 < \theta < \pi$, then the total force P resulting from an imposed deflection δ is

$$P = \sum_{i=1}^{n} P_{\eta, i} \tag{94}$$

which, when Equations (91), (92), and (93) are substituted into it, becomes

$$P = \delta \sum_{i=1}^{n} k_{Ri} \sin^2 \theta_i \qquad 0 \leq \theta \leq \pi \tag{95}$$

The resultant lateral stiffness $k_{L,M}$ for a major diameter fit spline is then

$$k_{L,M} = \sum_{i=1}^{n} k_{Ri} \sin^2 \theta_i \tag{96}$$

Since the individual tooth stiffness $k_{R,i}$ can be a weak function of applied load, an approximation of this applied load may be found by computing the radial load on each tooth using a modification of Equation (86):

$$P_i = \frac{\delta_{ri} E_y}{\ell \sum_{k} \frac{h_k}{A_k}} \tag{97}$$

P_i may then be inserted into Equation (80) as an average force per unit axial length (hence the appearance of ℓ in the denominator of Equation (97)).

To reiterate, the normal radial force on each tooth is first computed using only the term for axial compression of the body of the tooth. These normal forces are then inserted into the Hertzian terms for the stiffness of the individual teeth. The lateral stiffness is then calculated using these modified stiffness values.

Lateral Stiffness — Side Fit

The approach for computing the lateral stiffness will be basically similar to that used for the major diameter fit type. A downward deflection will be assumed for the internal or female spline and the force contribution of each tooth in the direction of the imposed displacement will be found and then summed over all teeth. Figure 62 shows a typical pair of teeth in contact. This will be defined as the ith contact point.

The contact point is at the pitch radius and determines angle θ. The angle ϕ is the contact angle and is determined by tooth geometry. With the geometry established, the outer member is given a small downward deflection δ which results in a normal force P_{ni} generated at the interface as the result of a total displacement δ_{ni} in the direction of the normal force. As before, displacement δ is small enough such that the original geometry is not significantly distorted. The angle Ψ normal to the plane of contact may be defined as

$$\Psi = \theta + \phi \tag{98}$$

where ϕ may be positive or negative depending on whether, for this geometry, the face is torque-loaded or not. If the leading or torque load carrying face of the male tooth is also loaded by P_{ni}, then ϕ is negative. The actual deflection of the mating teeth normal to their contact faces is

$$\delta_{ni} = \delta \left| \cos \Psi_i \right| \tag{99}$$

a) Tooth Geometry   b) Forces and Displacements
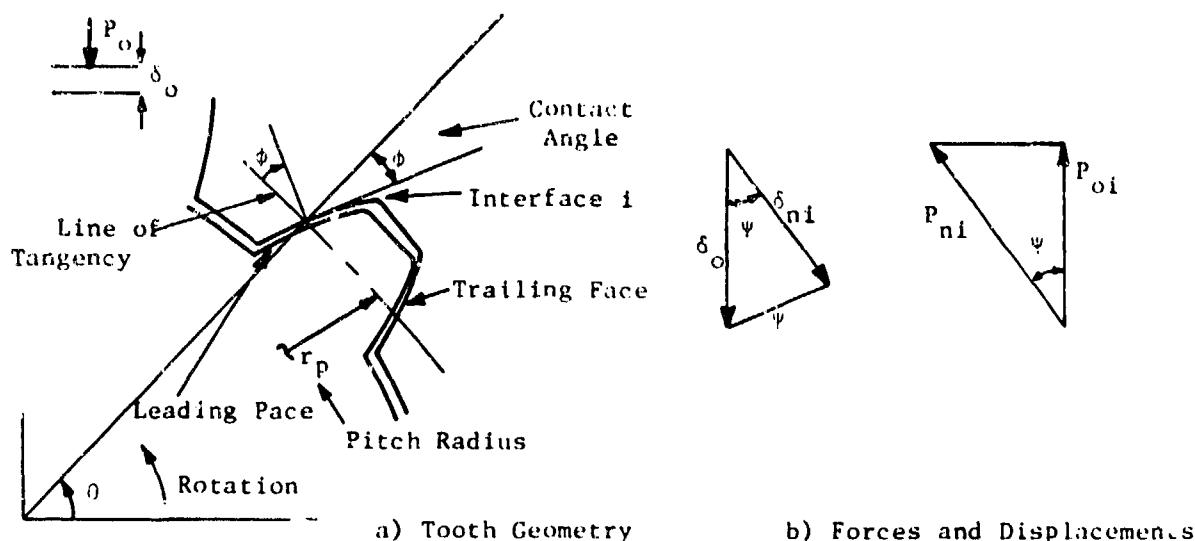
Figure 62. Model of Spline Teeth in Contact

The stiffness of the mating teeth, k_T, was given in Equation (86). It will be relabeled k_{Ti} because it may be different for each tooth due to the Hertzian term nonlinearity. The normal force P_{ni} is then

$$P_{ni} = k_{Ti} \, \delta_{i,i} \tag{100}$$

The resulting force along the line of δ is then P_i for each tooth, which can be seen from Figure 62 to be

$$P_i = P_{ni} \left| \cos \Psi_i \right| \tag{101}$$

From Equations (99) and (100) it is evident that

$$P_{ni} = k_{Ti} \, \delta \left| \cos \Psi_i \right| \tag{102}$$

and from Equations (101) and (102) we see that

$$P_i = k_{Ti} \, \delta \cos^2 \Psi_i \tag{103}$$

The average normal force is found, as described before, for each tooth by the equation

$$P_{AVG,i} = k'_{Ti} \, \delta \, | \cos \, \Psi_i |$$ (104)

where, referring to Equation (62),

$$k'_T = \frac{1}{Q_{B1} + Q_{S1} + Q_{R1} + Q_{B2} + Q_{S2} + Q_{R2}}$$ (105)

In addition, since the leading flanks of the male teeth carry a torque load, $P_{AVG,i}$ must be modified to reflect this factor:

$$P_{AVG,i} = k'_{Ti} \, \delta \, | \cos \, \Psi_i | \pm \frac{T}{2nr_p}$$ (106)

where T is the transmitted torque, r_p is the pitch radius, and 2n is the total number of spline teeth. The sign of the last term of Equation (106) is defined as follows:

+ for $- \pi/2 < \theta < \pi/2$

− for $\pi/2 < \theta < -\pi/2$

The total lateral stiffness $k_{L,s}$ for the side fit coupling is then found by summing Equation (103) over n teeth resisting the deflection and dividing through by that deflection.

$$k_{L,s} = \sum_{i-1}^{n} k_{Ti} \cos^2 \Psi$$ (107)

Angular Stiffness

The angular stiffness for a spline coupling will be a function of lateral stiffness and spline geometry. Figure 63 shows the right half of such a coupling, where the y axis runs down the coupling vertical centerline.

The bodies of the internal and external spline halves are assumed to be rigid so that the deformation of the teeth alone supplies the restoring moment. As shown in Figure 63, we shall look at one half of a coupling rotated about its left end plane (the center of the entire coupling) by a small angle ϵ. Further, a small amount of radial clearance c is permitted. Since the bodies of both coupling halves are assumed to be rigid, for the male half to rotate through angle ϵ it must deform the tooth material, starting at a distance c from the undeflected position. If a small section in the deformed portion is studied, it would appear as in Figure 64.

87
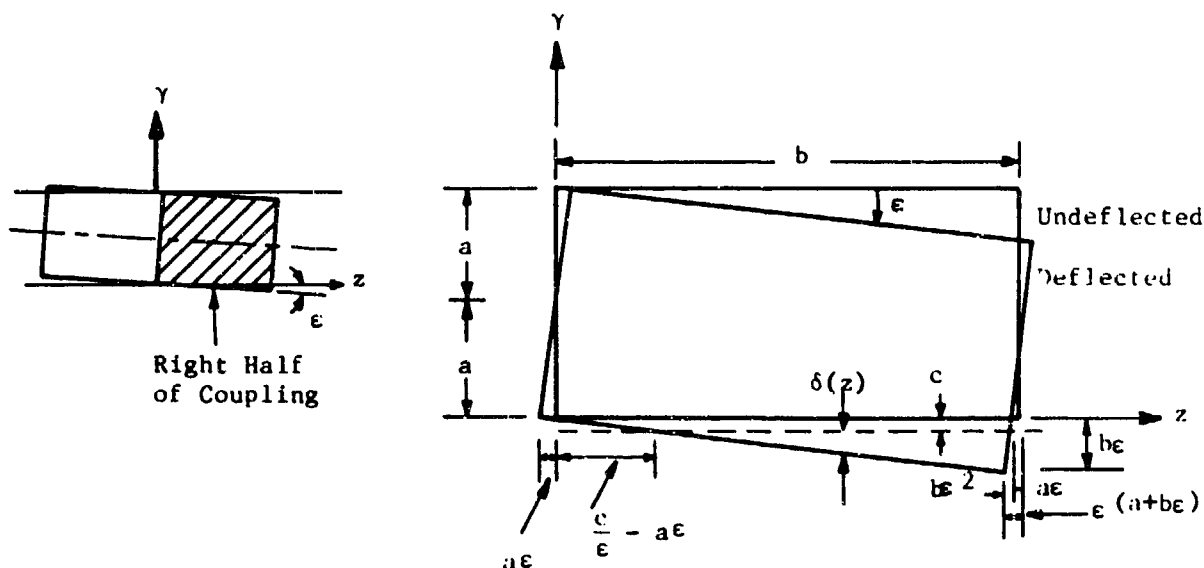
Figure 63. Geometry for Calculation of Angular Stiffness
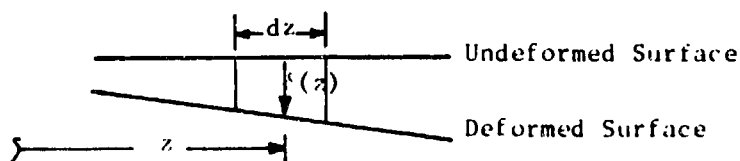
Figure 64. Enlargement of Small Section of Contact Zone

The stiffness contribution of a small segment of length dz is

$$k_{seg} = \frac{k_L}{2b} \, dz \tag{108}$$

where k_L is the overall lateral stiffness of the coupling and 2b is the length of coupling engagement. The deflection $\delta(Z)$ is found from Figure 63 to be

$$\delta(Z) = \epsilon \, (z + a\epsilon) - c \tag{109}$$

and the force generated in the differential segment is the product of Equations (108) and (109):

$$F(Z) = \frac{k_L}{2b} \left[\epsilon \, (z + a\epsilon) - c \right] \, dz \tag{110}$$

The moment resulting from this force is

$$M(Z) = ZF(Z) = \frac{k_L}{2b} z \left[\epsilon \, (z + a\epsilon) - c \right] \, dz \tag{111}$$

The moment is next multiplied by 2 and integrated over the length of contact.

$$M(Z) = \frac{k_L}{b} \int_d^e z \left[\epsilon (z + a\epsilon) - c \right] dz \qquad (112)$$

where the limits of integration d and e are the boundaries of the contact area:

$$d = \frac{c}{\epsilon} - a\epsilon \qquad (113)$$

$$e = b - \epsilon(a + b\epsilon) \qquad (114)$$

When the integration is performed and the result evaluated at the limits, we get

$$M = \frac{k_L}{b} \left\{ \frac{\epsilon}{3} (e^3 - d^3) + \frac{(a\epsilon^2 - c)}{2} (e^2 - d^2) \right\} \qquad (115)$$

The angular stiffness k_A is then

$$k_A = \frac{M}{\epsilon} = \frac{k_L}{b} \left\{ \frac{(e^3 - d^3)}{3} + \frac{(a\epsilon^2 - c)(e^2 - d^2)}{2\epsilon} \right\} \qquad (116)$$

Because the k_L term may be nonlinear due to Hertzian deflection, an average deflection may need to be assumed in order to obtain an average force. (Refer to the previous stiffness analysis for major diameter and side fit couplings.) This will be handled by finding an "average" deflection δ_{AVG} for use in calculating the average force used in the Hertzian term. The equation for this deflection is Equation (109) evaluated at the average of the two end-points, Equations (113) and (114).

$$\delta_{AVG} = \frac{1}{2} (b\epsilon - \epsilon^2 - C) \qquad (117)$$

For the case of major diameter fit couplings, lateral stiffness k_L is given by Equation (96). Clearance c is assumed to be zero and the resulting calculation is straightforward. For side fit spline couplings, there is a finite clearance between the major diameters of the internal and external splines, which is the clearance c in Figure 63. If ϵ is small enough ($b\epsilon < c$), the contact is only on the tooth flanks and Equation (108) may be used to describe the lateral stiffness, with c = 0. If, however, the angle is large enough to cause contact at the major diameter, then Equation (116) must be applied a second time, using Equation (96) for radial stiffness and with c being set equal to the major diameter clearance.

b. Spline Coupling Damping Coefficients

Damping coefficients for a spline coupling are found by assuming the damping to consist primarily of Coulomb damping. The energy dissipated per cycle by this mechanism will be computed and used to find an equivalent viscous damping coefficient for use in the stability calculation. Figure 65 shows an elementary spring-mass-damper system where the damping is provided by a rigidly connected Coulomb damper.
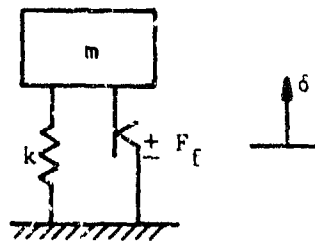
Figure 65. E l e m e n t a r y Spring — Mass — Coulomb Damper System

The differential equation of motion for this system is

$$m\ddot{\delta} + k\delta \pm F_f = 0 \tag{118}$$

where the frictional force F_f is constant in magnitude and always in a direction opposed to the velocity. An approximate solution to this equation is based on the equivalence of energy dissipation between this and a viscous damped system. The energy E_c dissipated per cycle for a Coulomb damped system is simply

$$E_c = 4F_f \delta_o \tag{119}$$

where δ is the maximum zero-to-peak amplitude of the system. For a viscous damped system, the energy dissipated per cycle E_v is

$$E_v = \pi C \omega \delta_o^2 \tag{120}$$

where C is the damping coefficient, ω is the angular frequency, and δ_o is as previously defined. If we wish to define a viscous damped system equivalent to the one in Figure 65, Equations (119) and (120) are equated and solved for C_{eq}, the equivalent viscous damping coefficient:

$$C_{eq} = \frac{E_c}{\pi \omega \delta_o} \tag{121}$$

A coefficient has thus been found which, for a specified oscillation amplitude and frequency, causes the same energy to be withdrawn using a viscous mechanism as the original system did using sliding friction. The two systems would then be expected to exhibit similar behavior under these conditions.

The spline coupling damping coefficients will be treated in the above manner, where δ_o will be the relative lateral or angular displacement of the coupling pieces and F_f the total frictional force or moment resulting from δ_o. Since instability is expected to occur at the first natural frequency, ω is the difference between the running speed (or speed of interest) and the first natural frequency where the former is assumed always greater than the latter.

The friction force may be computed using the equation

$$F_f = f F_n \tag{122}$$

where f is the coefficient of friction and F_n the normal force. The overall coupling friction force will be found by computing the normal force on each pair of sliding surfaces, applying an assumed or computed coefficient of friction, and summing the friction force components for all the interfaces.

If the coupling teeth are evenly spaced, the force in the circumferential direction F_T due to applied torque T is

$$F_T = \frac{T}{r_p n} \tag{123}$$

where n is the number of teeth and r_p is the pitch radius. Figure 66 illustrates the geometry for computation of the normal force $F_{n,T}$ for a single tooth. From the figure, it can be seen that

$$F_{n,T} = \frac{F_T}{\cos\phi} \tag{124}$$

Hence, the normal force on the tooth flank due to torque is found from Equations (123) and (124) to be

$$F_{n,T} = \frac{T}{r_p n \cos\phi} \tag{125}$$
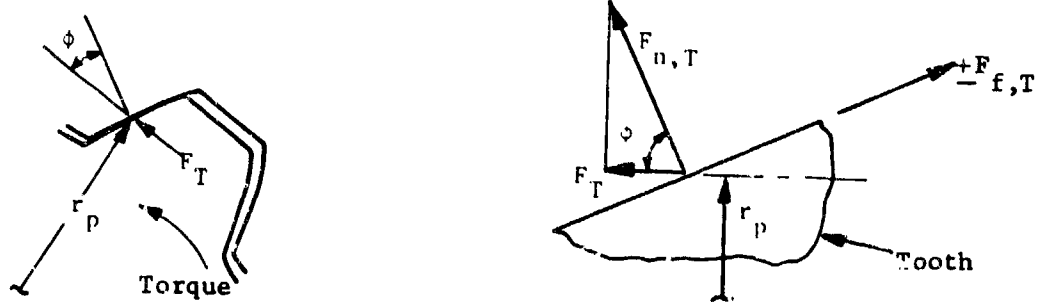
Figure 66. Geometry for Normal Force on Tooth

The friction force for that tooth may be found from Equations (122) and (125) to be

$$F_{n,T} = \frac{fT}{r_p n \cos\phi} \tag{126}$$

The energy dissipated per cycle for the spline coupling will now be computed. Since the oscillation caused by an instability will not be laterally planar but will rather be a whirl phenomenon, all contacting interfaces are fully cycled for each cycle of spline motion. The energy dissipated per cycle is then the energy dissipated at one interface for a completed cycle, multiplied by the number of such interfaces. This method, of course, assumes circular nonsynchronous whirl.

If a radial displacement δ_o exists, then the interface moves a distance δ_i such that

$$\delta_i = \frac{\delta_o}{\cos\phi} \tag{127}$$

Equation (119) describes the energy dissipated per cycle for a general friction damped system. When Equations (126) and (127) are substituted into (119), the result is

$$E_{c,i} = \frac{4fT\delta_o}{r_p n \cos^2\phi} \tag{128}$$

which is the energy dissipated by one interface over a full cycle. For n interfaces, the energy dissipated $E_{c,R}$ in radial motion per cycle is

$$E_{c,R} = \frac{4fT\delta_o}{r_p \cos^2\phi} \tag{129}$$

Note that there is no dependence on the number of spline teeth in contact (using this particular model).

For angular motion, the energy for ¼ cycle is found by assuming an angular displacement of α_o, as shown in Figure 67.
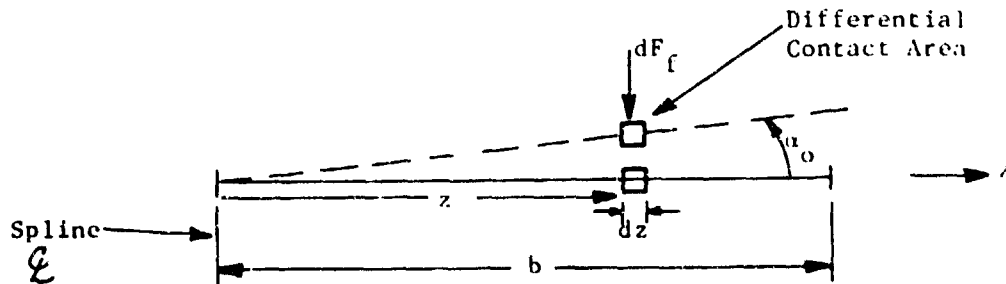
Figure 67. Geometry for Frictional Moment

The friction force dF_f for a small section of the contact area is

$$dF_f = \frac{F_{i,T}}{2b} dz \tag{130}$$

where 2b is the length of the spline and dz is the width of the contact area.

The distance through which this force moves is $z\alpha_o/\cos\phi$. The energy dissipated by one interface is then

$$E = 2 \int_o^b \frac{F_{i,T}}{2b} \frac{\alpha_o z}{\cos\phi} dz \tag{131}$$

where the factor of 2 accounts for the other half of the interface (negative z). The energy dissipated per cycle is the above integral, evaluated at its limits, and multiplied by a factor of four:

$$E_{c,i} = \frac{2F_t \alpha_o b}{\cos\phi} \tag{132}$$

When Equation (126) is substituted into (132) and the result multipled by the number of interfaces, the energy dissipated by the spline per cycle of angular motion (conical) results:

$$E_{c,A} = \frac{2f\,Tb\alpha_o}{r_p\,\cos\phi} \tag{133}$$

Equivalent viscous damping coefficients, b and β, for lateral and angular motion, respectively, can be found using Equation (121). Since b and β are for one axis only, Equations (129) and (133), which cover complete motion, must be divided by a factor of two before being substituted into Equation (121). The net results of these substitutions are

$$b = \frac{2fT}{r_p \pi \omega \delta_o \, \cos^2\phi} \tag{134}$$

$$\beta = \frac{fTb}{r_p \pi \omega \alpha_o \, \cos^2\phi} \tag{135}$$

The two values above may be used directly as the equivalent viscous coefficients which simulate for given conditions the friction damping present in the coupling.

A description of the complete computer program (Report No. FR-10601) was provided to the Applied Technology Laboratory in October 1978. A User's Manual for this program appears in Appendix B.

c. Strategy for Stability Calculations

The following is a suggestion for the strategy to be used in performing a stability calculation for a particular rotor-bearing-coupling system:

1. Model the rotor-bearing system using standard procedures. Define the spline coupling geometry and torque.

2. Assume a running speed and vertical and lateral whirl amplitudes. Since amplitude appears in the equivalent viscous damper expression as a denominator, the damping becomes undefined for zero whirl amplitude. The following two procedures for estimating the amplitude are suggested:

   a. If the misalignment is small, the coupling may lock up for small whirl amplitudes, accommodating small displacements through tooth deflection. The maximum friction force at a tooth interface is given by Equation (126), where f is now the coefficient of static friction. This represents the largest force transmittable by a pair of teeth in contact with only elastic tooth deflection. The deflection of the mating

teeth along the line of force is given by the sum of Equations (58), (64) and (71) for each tooth. If the amplitude is assumed to be slightly larger, it cannot be accommodated by elastic deflection, sliding occurs with the accompanying internal friction, and instability is a possible result if external damping is not large enough. We have thus established a "floor" for our assumed amplitude.

b. When misalignment is large, sliding must already occur in order for the coupling to accommodate it. The coupling, therefore, cannot lock up, and it is possible for any whirl amplitude to generate internal sliding friction. For this case, it appears best to assume a whirl amplitude for the shaft system in the first mode, as it is this mode which is expected to be excited. The coupling lateral and angular amplitude may be easily formed from the assumed deflection and the mode shape.

3. Using the methods outlined in Sections V.A.2.a and V.A.2.b, calculate coupling stiffnesses k and H and damping coefficients b and β. The coefficient of friction must be estimated in order to find the latter two coefficients. It is assumed that the coupling is lubricated and, furthermore, enough lubricant gets between the contacting faces to prevent metal-to-metal contact. The relatively low sliding velocities (a few tens of centimeters per second), the high loads, and the oscillatory motion suggest that boundary lubrication (as opposed to hydrodynamic or elastohydrodynamic) occurs. This suggests that friction coefficients will generally be not too far below those seen in metal-to-metal contact and certainly greater than those resulting from a film generated at higher velocities or through a rolling/sliding mechanism. Reference 17 contains a plot of coefficient of friction against sliding speed for "surfaces capable of hydrodynamic lubrication." In the boundary lubrication region, the coefficient of friction lies in the approximate range from 0.08 to 0.10. Reference 18 gives an empirical equation for coefficient of friction for the rolling-sliding case, derived from roller test data:

$$f = 0.0127 \log_{10} \left[\frac{3.17 \times 10^8}{\frac{\mu_0 V_s}{\omega} \quad V_T{}^2} \right] \tag{136}$$

where μ_0 is the lubricant viscosity (cp), ω is the load (lb/in. of face width), and V_s and V_T are sliding and sum velocities (in./sec) of the two surfaces, respectively. Realizing that we have pure sliding and assuming $V_s V_T{}^2$ can be

17 Rabinowitz, E., "Frictional and Wear Materials," John Wiley and Sons, New York, 1965.

18 Benedict, G. H., and Kelly, B. W., "Instantaneous Coefficients of Gear Tooth Friction," ASLE Transactions 4, 59-70, 1961.

94

replaced with the cube of the sliding velocity $V_s{}^3$, we can obtain an equation for further guidance on the value of the friction coefficient:

$$f = 0.0127 \log_{10}\left[\frac{3.17 \times 10^8}{\frac{\mu_0}{\omega} \, V_s{}^3}\right] \tag{137}$$

which is valid for values of the friction coefficient from about 0.005 to 0.08.

Boylan (Reference 19) performed tests on gear couplings and measured coefficients of friction as a result of misalignment (replotted in Reference 20 vs sliding velocity). Coefficients of friction ranged from 0.15 to 0.25 for low velocity to a low of 0.05 to 0.10 at about 60 cm/sec sliding velocity and rose above that velocity. These tests were done on a test rig capable of rotational speeds to 9000 rpm, and the friction was apparently very difficult to pin down.

The velocity may be calculated for lateral motion by the equation

$$V_{MAX,L} = \delta\Omega \tag{138}$$

and for angular motion the "average" maximum velocity, that is the maximum velocity at a point halfway between the center and edge, is

$$V_{MAX,A} = \frac{\alpha b}{2}\, \Omega \tag{139}$$

An average velocity for both cases would then be the maximum divided by $\sqrt{2}$:

$$V_{AVG,L} = \frac{\delta}{\sqrt{2}}\, \Omega \tag{140}$$

$$V_{AVG,A} = \frac{\alpha b}{\delta\sqrt{2}}\, \Omega \tag{141}$$

Since angular and lateral misalignment probably will occur along the same plane, velocity totals would be the sums of Equations (138) and (139) or (140) and (141). Equations (138) and (139) would be used for the friction-correlation of References 19 and 20, while Equations (140) and (141) appear to apply for the cases of References 17 and 18.

4. Having all necessary coefficients in hand, the damped eigenvalues of the system can now be computed. This should be done for several speeds, loads, and misalignments in the operating range to obtain a clear stability map (plot of the eigenfrequencies versus the varied parameters) of the system being studied.

19 Boyland, W.,"Marine Application of Dental Couplings,"Soc. Nav. Arch. and Nav. Engrs. Marine Power Plant Symposium, Paper 26, May 1966.

20 Crease, A. B.,"Design Principles and Lubrication of Gear Couplings,"International Conference on Flexible Couplings for High Powers and Speeds, University of Sussex, England, June 28 to July 1, 1977, Paper B1.

B. EXPERIMENTAL RIG DESIGN

The nonsynchronous rig configuration is shown in Figures 68 and 69. It consists of a damped thrust bearing simulator rig, which includes a turbine shaft supported on two bearings. The rear end of the shaft is supported on a duplex pair ball bearing and a squeeze film damper through a flexible bearing support. The front of the shaft has been modified to accommodate the interchangeable test splines which are supported by a separate set of duplex ball bearings. The rig was driven by a turbine which is attached at the rear of the existing rotor dynamics rig shaft. High pressure steam flowed through the turbine to develop the torque necessary to produce nonsynchronous whirl. The torque was transmitted through the spline and absorbed via a water brake. The transmitted torque was measured at the water brake with a torque arm mounted on a force scale.

The turbine end ball bearings are axially preloaded against a second pair of bearings through a connecting rod to prevent bearing skid. The test spline stub shaft is also supported on preloaded duplex bearings as shown in Figure 70. To allow for independent control of the spline lubrication, a separate supply line is provided to the spline area (item 1 in Figure 70). In addition, a seal cup is provided so that the bearing oil will not lubricate the spline teeth during the "dry" spline portion of the test (item 2 in Figure 70). The entire rig lubrication schematic is shown in Figure 71.

Figures 72 and 73 are photographs of the rig as installed in the test stand. The former shows an overall view of the turbine end of the rig and the thrust bearing housing. The latter shows an overall view of the water brake end of the rig and the test spline housing.

C. RIG TEST

1. Test Plan

The objective of the nonsynchronous response rig test was to generate experimental data to verify the analytical predictions of the nonsynchronous whirl phenomenon induced by spline friction. Parameters such as damper oil supply, type of spline, spline clearance fit, amount and type of spline lubricant, and their effects on spline induced vibration was studied. The test data was correlated with the prediction of the spline friction analytical model developed in Section V.A.

The instrumentation is depicted in Figure 74. Shaft response was monitored by means of vertical and horizontal accelerometers located at the turbine end bearing support. In addition, two proximity probes at the midspan of the shaft measured midspan shaft deflection. The signals from the vertical accelerometer and proximity probe were processed through a real-time analyzer for on-line data evaluation. This provided continuous monitoring of all nonsynchronous rotor vibrations. In addition to the real-time analyzer, the vertical and horizontal proximity signals were fed through a tracking filter. The filtered and unfiltered signals were plotted to isolate the nonsynchronous vibration components. All signals were recorded on magnetic tape. A photograph of the test stand instrumentation setup is presented in Figure 75.

The test program is outlined in Figure 76. The test hardware consisted of four different splines: side fit and major diameter fit with two different clearances each (designed according to ANSI spec B92.1 - 1970).
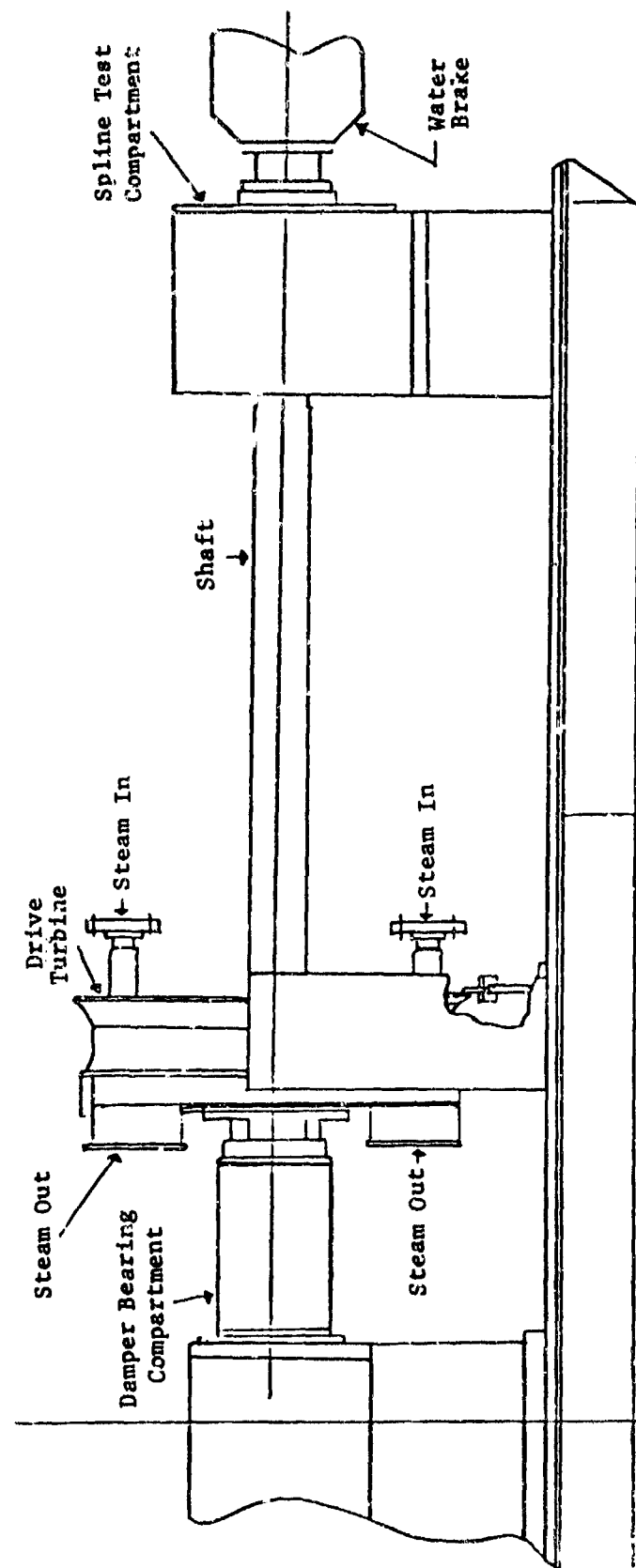
Figure 68. Nonsynchronous Rig

Spline Test Compartment

Water Brake

Shaft

Drive Turbine

Steam In

Steam In

Steam Out

Steam Out

Damper Bearing Compartment

97
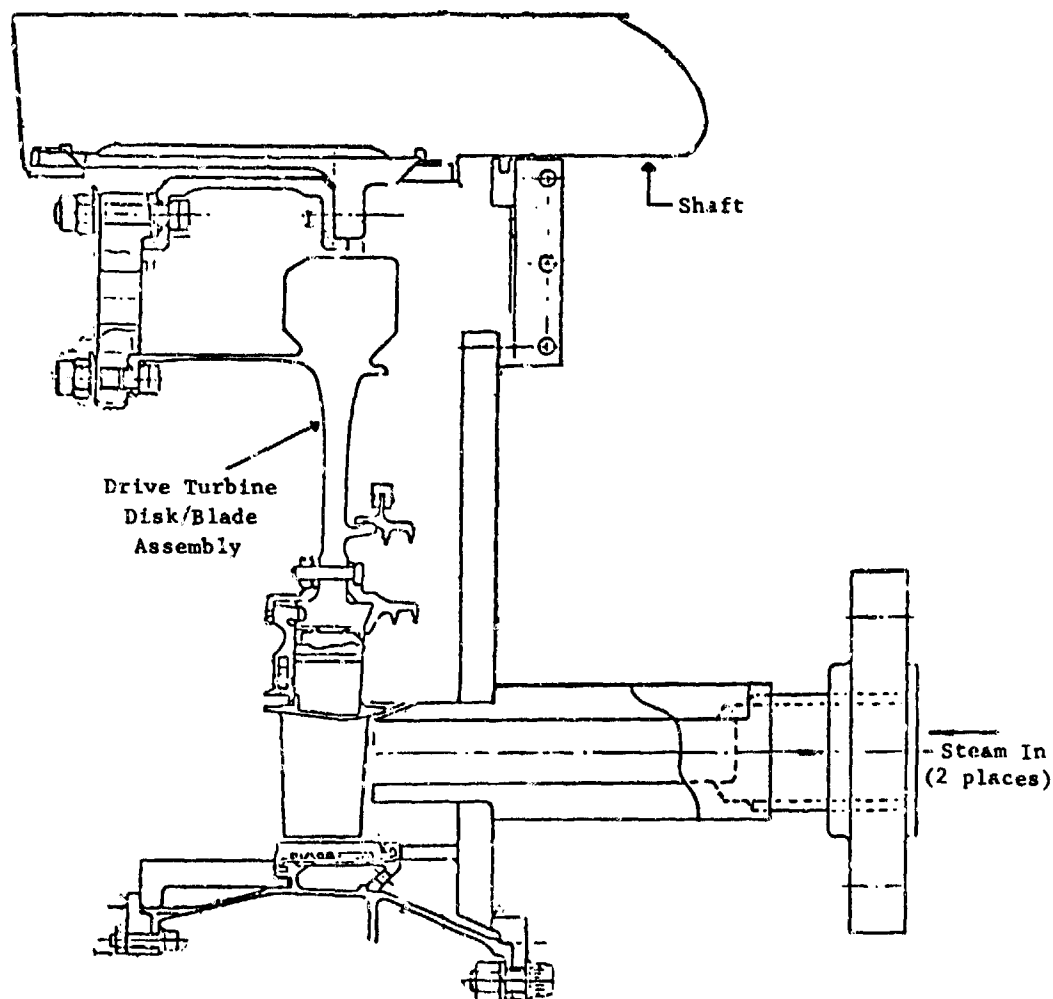
Figure 69. Detail of Drive Turbine Assembly

The test program called for six baseline runs. Each run consisted of a slow acceleration through the rig operating speed range with a "dry" spline and damper as a baseline. Once a threshold of instability was established, spline lubricant was allowed to flow at three different rates. The effect of each flow rate on the instability speed was recorded. Once the threshold had been reached at each spline flow rate, damper lubricant was allowed to flow to the squeeze film damper. The damper was utilized to suppress spline-induced instabilities throughout the rig speed range.
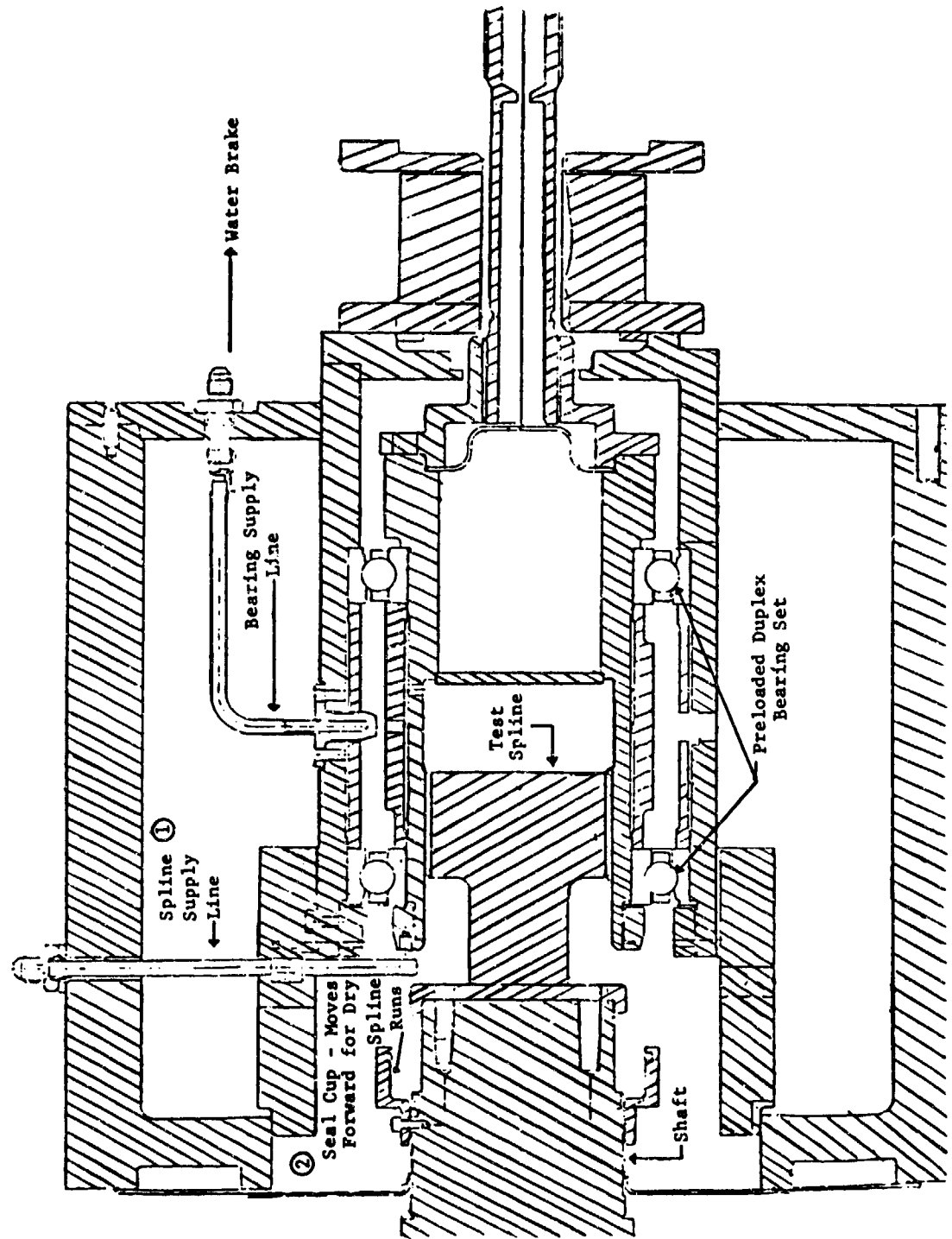
Figure 70. Detail of Spline Test Compartment

99
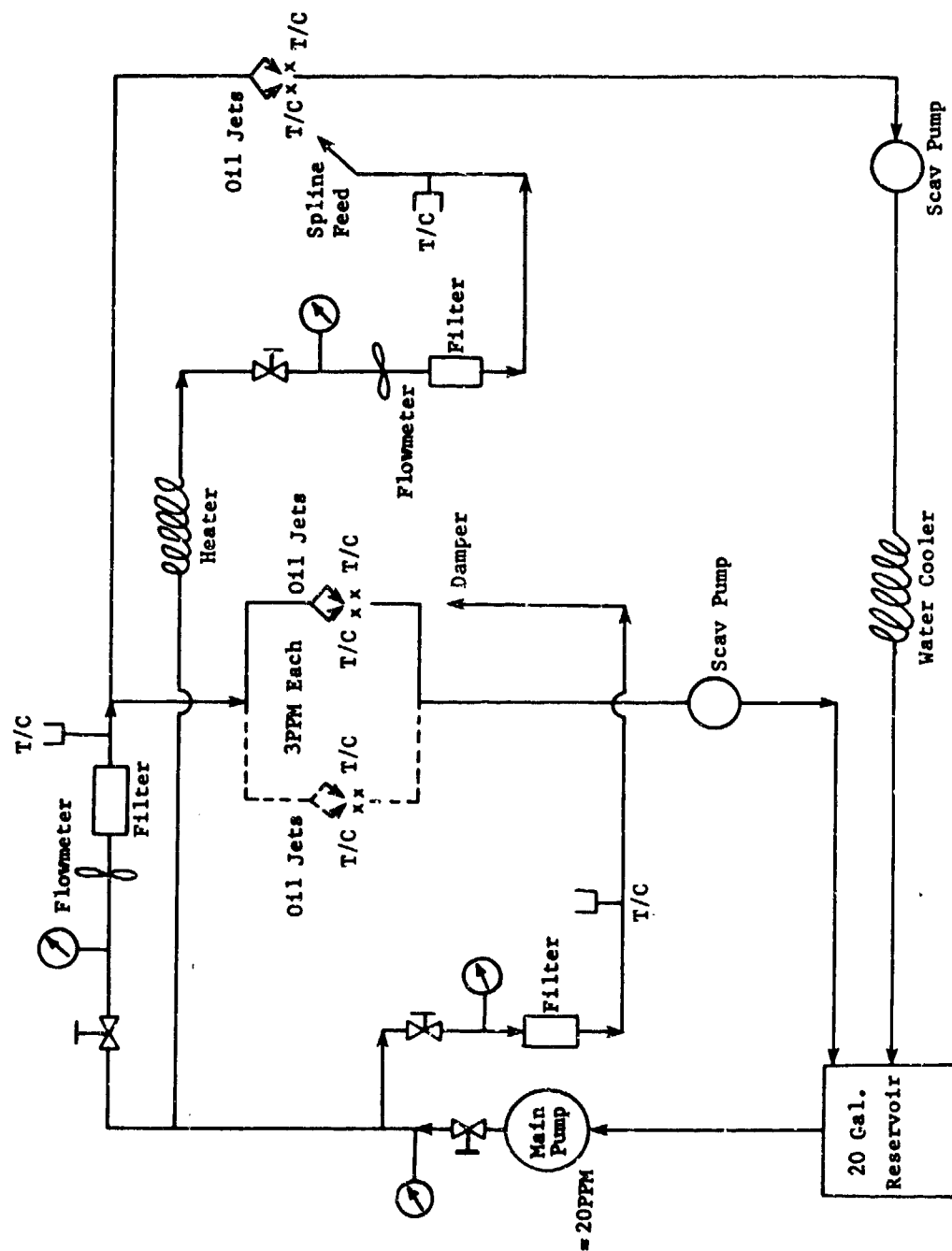
Figure 71. Lubrication System

Figure 72. Nonsynchronous Rotor Dynamics Rig D-8 Stand,Overall View,Right Rear

Figure 73. *Nonsynchronous Rotor Dynamics Rig D-8 Stand, Overall View, Front*

Figure 74. Nonsynchronous Rig Instrumentation Schematic Diagram

Figure 75. Nonsynchronous Rotor Dynamics Rig D-8 Stand Instrumentation Setup

Spline ANSI B92-1 1970 Run Mode	Side Fit		Major Diameter Fit	
	CL 1* 0.0036 0.0015	CL2 0.0065 0.0035	CL 1* 0.0036 0.0026	CL 2 0.0012 0.0002
Dry Spline Baseline	✕	✕	✕	✕
Spline A 0.15 ppm	✕	✕	✕	✕
Lubricant B 0.20 ppm	✕	✕	✕	✕
Flow rate C 0.25 ppm	✕	✕	✕	✕
Active Damper	✕	✕	✕	✕

*These Columns Were Repeated for Type III Lubricant
Max Rig Speed 7000 rpm
Max Rig Torque 4500 in.-lb

Figure 76. Nonsynchronous Test Program

104

2. Test Results

The nonsynchronous whirl test rig results are summarized in Figure 77. Shown in the same form as the test program (Figure 76), this figure illustrates which of the test rig configurations experienced spline-friction-induced rotor instabilities. The side fit spline was unstable for both the loose and tight tooth clearance configuration when unlubricated. In all test runs (both side fit and major diameter fit splines), when spline lubrication was allowed the rotor instability was suppressed. The major diameter fit splines were always stable; even when unlubricated the spline lubricant flow rate had no effect on stability. To determine the effect of squeeze film damping on rotor instability, the tight clearance side fit spline was run unlubricated with the rig squeeze film damper activated. The result was that the damper also acted to suppress the unstable nonsynchronous whirl.

Spline Configuration Run Mode	Side Fit		Major Diameter Fit	
	Loose	Tight	Loose	Tight
"Dry" Spline	U	U	S	S
"Wet" Spline	S	S	S	S
"Dry" Spline "Activated" Damper		S		

U = Unstable Rotor Vibrations (Nonsynchronous)

S = Stable Rotor Vibrations (Synchronous)

Figure 77. Summary of Nonsynchronous Rig Test Results

The unfiltered midshaft vibration levels for the tight clearance side fit spline are presented in Figure 78. The response plot shows a rotor bounce resonance at about 2400 rpm, and at about 4200 rpm the overall vibration level climbs very rapidly for the unlubricated spline, but there is no increase for the lubricated spline. Rotor instability occurred at that point, and this is verified by the frequency response plot of Figure 79. Here, the frequency components of the 4200 rpm are shown. Note that the largest component of response is at 64% of the shaft speed (0.64E). Also, a small 2E vibration, which can be associated with a slight coupling misalignment, can be observed.

For comparison, Figure 80 shows the frequency response plot of lubricated side fit spline test at 7000 rpm. Note that no subsynchronous frequencies are present and only a small 2E component can be observed. All of the runs summarized in Figure 77 had the same response characteristics as those shown.
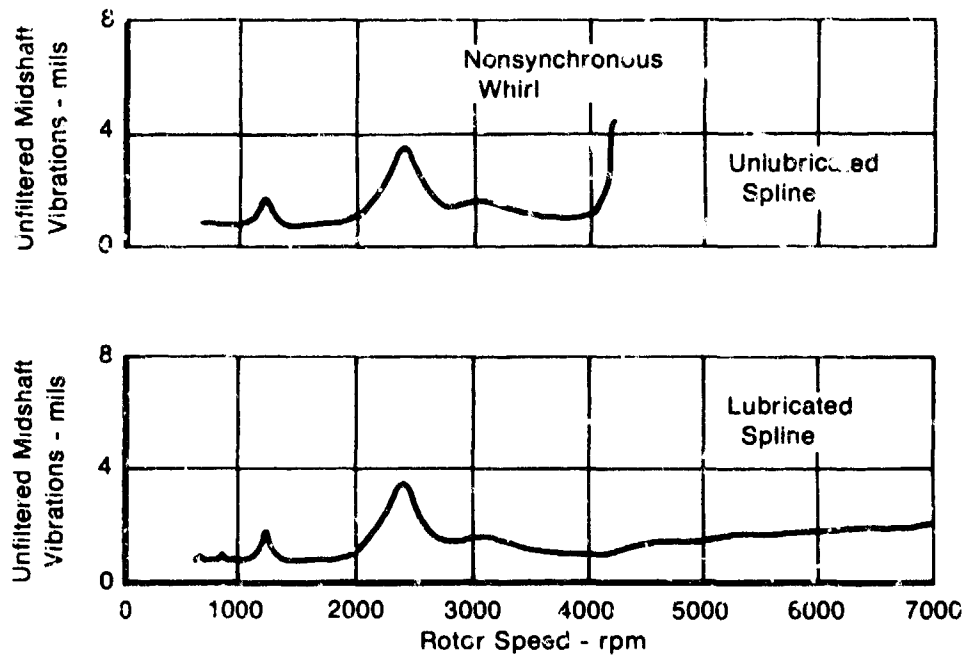
Figure 78. Tight Clearance Side Fit Spline Rotor Response (Lubricated and Unlubricated)
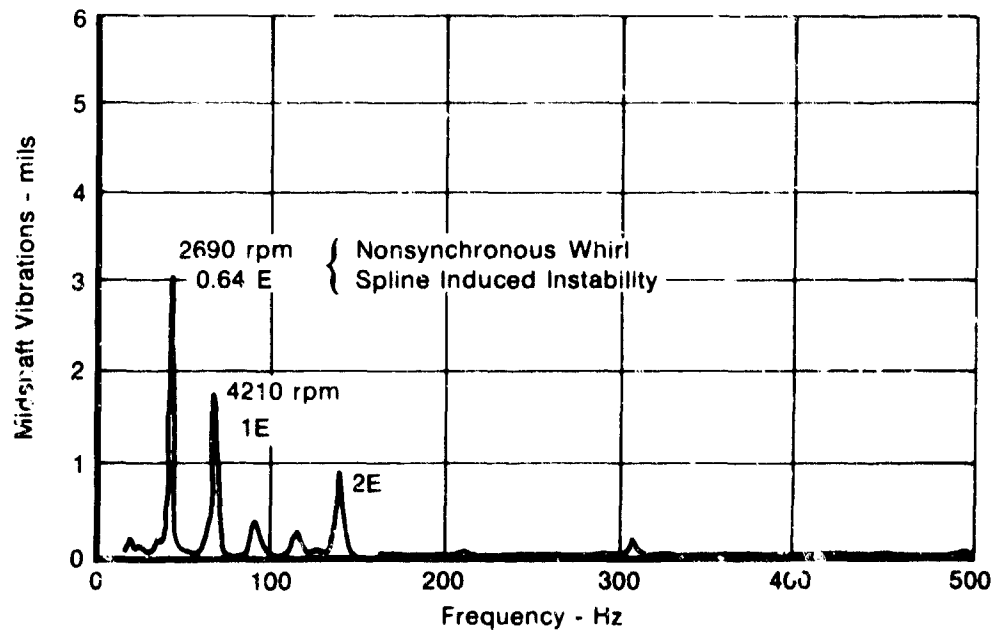
Figure 79. Response Amplitude vs Frequency at 4210 rpm (Unlubricated Side Fit Spline)

106
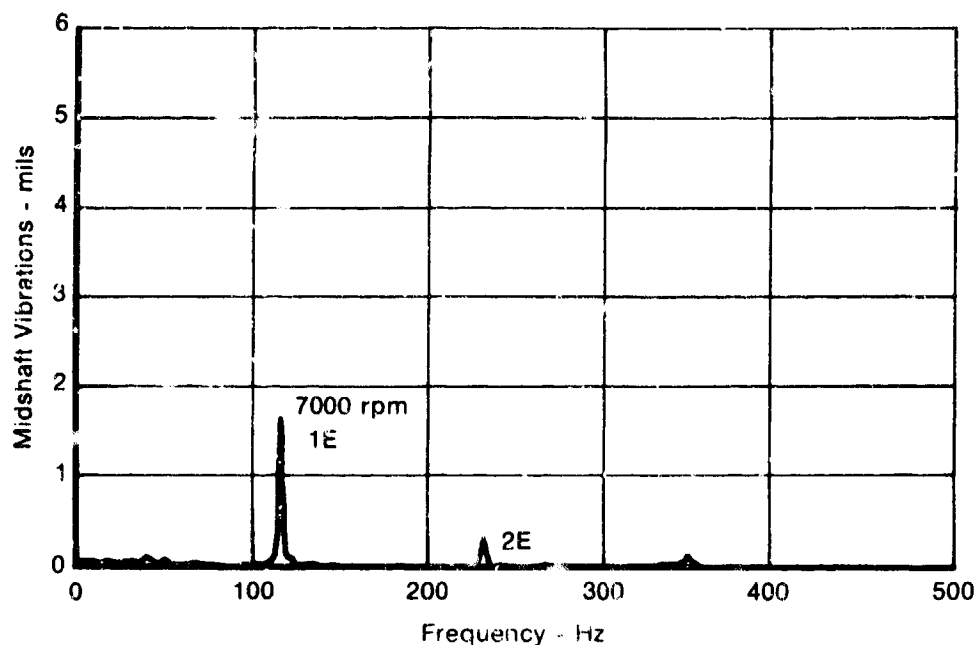
Figure 80. Response Amplitude vs Frequency at 7000 rpm (Lubricated Side Fit Spline)

In addition to the planned tests, one run was made to verify the effectiveness of the rig's squeeze film damper to reduce the steady-state unbalance response amplitude. With very low water brake load, the rig shaft speed was increased from 0 to 7000 rpm. Figure 81 shows the midshaft vibration response with and without the squeeze film damper activated. Note that at least a 50% reduction in rotor response occurred when the rig was damped. The increase in damper oil supply pressure had very little effect on rig response.

D. DATA CORRELATION WITH ANALYTICAL MODEL

The analytical model used to predict the stability characteristics of the nonsynchronous whirl rig was the spline coupling friction model developed in Task VIII of this program and used with a rotor system stability model similar to that of Reference 13. The rotor and spline physical dimensions were input to the stability model, and the output was complex eigenvalues and eigenvectors. The imaginary part of the eigenvalue gives the frequency of vibration and the real part gives the exponential growth factor. If positive, the vibration is unstable; if negative, it is stable. The eigenvectors give the mode shape of the whirling shaft. A parametric study was performed to find the effects of changing various rig and coupling parameters on the rig stability characteristics.

The rig was modeled for use in the rotor dynamics programs with a 12-station, 11-section breakup. The model was run to determine its undamped critical speeds with the assumption that the spline coupling is very stiff. The first four undamped critical speeds were found to occur at 2376, 5092, 9354, and 14,885 rpm. The mode shapes for the first two speeds are shown in Figures 82 and 83.
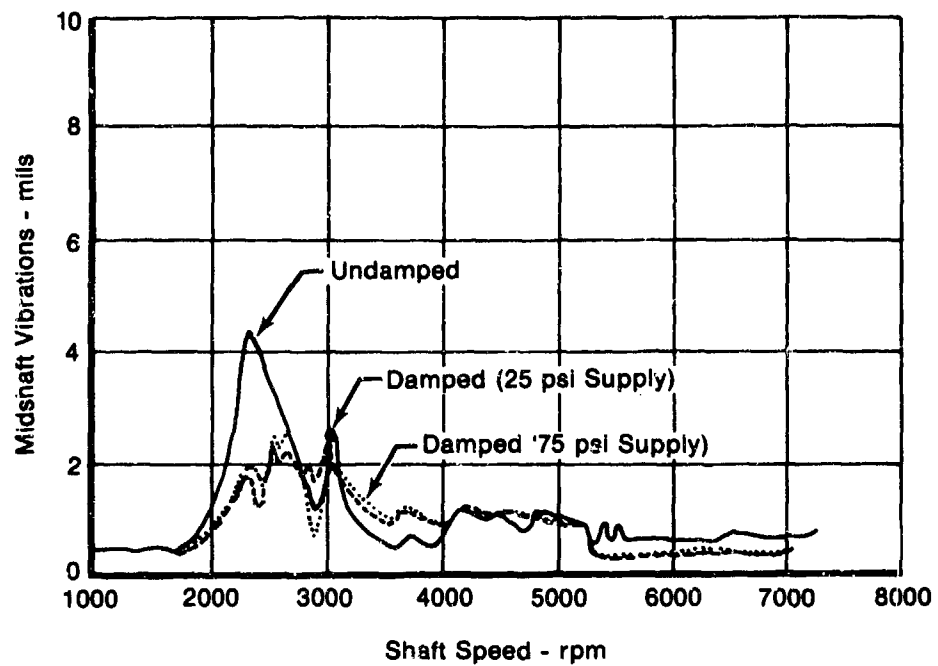
Figure 81. Damper Effectiveness Demonstrated
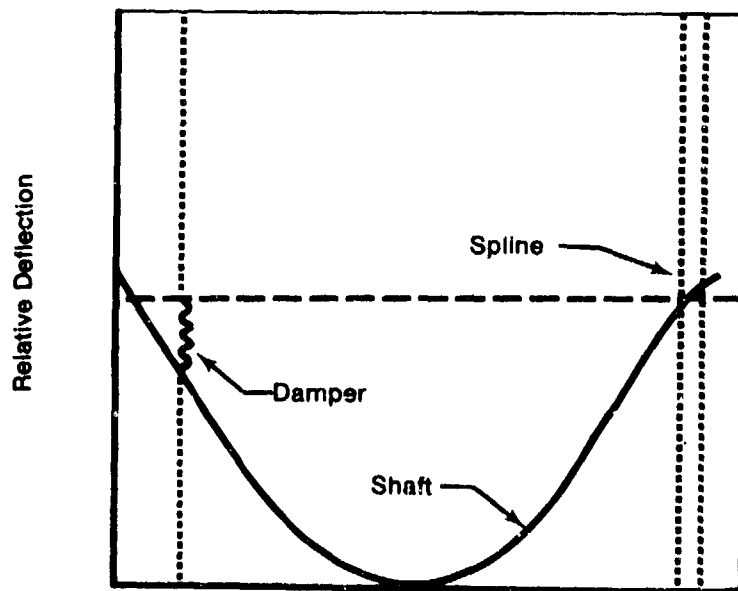
Critical Speed = 2376 rpm

Figure 82. First Critical Speed Nonsynchronous Rig

108
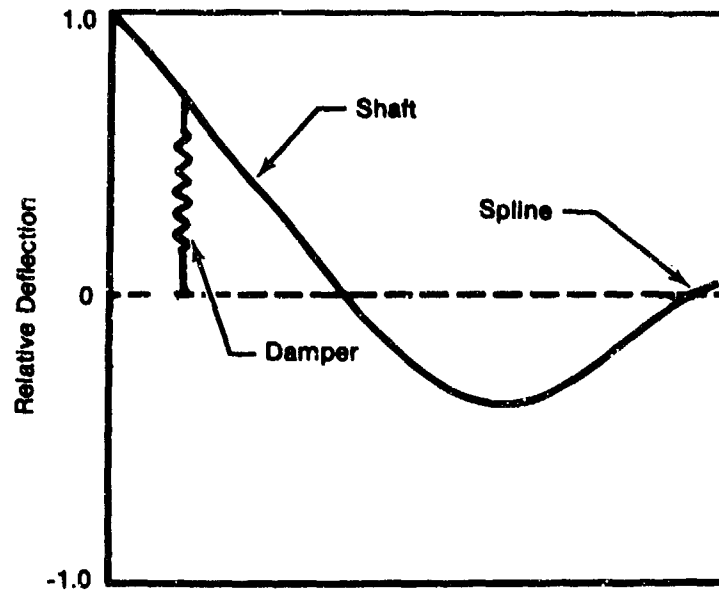
Critical Speed = 5092 rpm

Figure 83. Second Critical Speed Nonsynchronous Rig

For subsequent stability runs, the model was modified by inserting the spline coupling stiffness and damping coefficients at the spline end of the shaft and inserting the damper bearing coefficient of damping at the squeeze film damper location. Basically, the model describes the spline coupling in terms of four coefficients:

1. Radial stiffness, k (lb/in.)
2. Angular stiffness, κ (lb/in.radian)
3. Radial damping, b (lb-sec/in.)
4. Angular damping, β (in.-lb-sec/radian)

These values are then used with the rotor model as input to the rotor-bearing system stability program.

The angular stiffness of the coupling varies with the angular whirl amplit... the mplitude of the external spline coupling half within the internal half). The two dampin   ...   .ents are sensitive to the following quantities:

● Running speed
● Coupling angular whirl amplitude (external spline relative to internal)
● Rotor system first critical speed (at which instability is expected to occur)
● Coupling radial whirl amplitude (external spline relative to internal)
● Coefficient of friction of spline coupling
● Transmitted torque.

109

Because the Coulomb friction damping actually present in the coupling has been modeled with equivalent viscous damping coefficients, the resulting coefficients b and β vary with amplitude, relative speed (running speed minus first critical speed), pressure angle at the pitch diameter (a function of spline geometry), and all the parameters previously listed. A spline analysis using this method therefore takes the form of a parametric study.

The spline coupling model was run with the following assumptions:

1. The coefficient of friction is 0.15.

2. The transmitted torque is 2000 in.-lb, which is about half of the full load torque of 4052 in.-lb.

3. The radial amplitude is equal to the radial clearance plus a lateral deflection of 2×10^{-6} in.

4. The angular amplitude is equal to the angle e defined by the radial clearance and the coupling length plus a nominal coupling angular deflection.

$$e \geq \tan^{-1} \frac{2C}{l}$$

where C is the clearance and l is the coupling length. The coupling angular deflection was taken to be 0.0076 deg. Values for both lateral and angular deflections were found by estimating the intercoupling forces and, for calculated stiffnesses, finding the resulting deflections.

5. The first critical was taken from the undamped analysis to be 2400 rpm.

6. The rotor was running 2500 rpm above its first critical speed, giving an operating speed of 4900 rpm.

7. The given fillet radius of 0.027 in. does not define a fillet which extends uniformly from the root of the tooth to the form diameter. The smallest value for this radius, assuming a circular fillet, is 0.040 in., and that was used.

The final models for the four test splines are given in Table 4. These served directly as input to the spline coupling computer program.

The analysis of the test rig was performed by choosing and analyzing a nominal coupling configuration and then analyzing perturbations of this case. For this study, the loose, side fit spline coupling was defined as the nominal case, which is described in the third column in Table 4. Perturbations of this case consisted of changes to the spline coupling coefficients and changes to the test rig geometry or operating conditions.

110

TABLE 4
MATHEMATICAL MODELS OF FOUR TEST RIG SPLINE COUPLINGS

	Loose Major Diameter Fit	Tight Major Diameter Fit	Loose Side Fit	Tight Side Fit
Operating Speed (rpm)	4900	4900	4900	4900
Number of Tooth Pairs	36	36	36	36
Number of Segments, Ext.	10	10	10	10
Number of Segments, Int.	10	10	10	10
Pressure Angle (deg)	30	30	30	30
Face Width (in.)	1.75	1.75	1.75	1.75
Young's Modulus (lb/in.^{2})	30×10^6	30×10^6	30×10^6	30×10^6
Poisson's Ratio	0.3	0.3	0.3	0.3
Contact Patch Width (in.)	0.1	0.1	0.1	0.1
Angle of Tilt (deg)	0.1025	0.0239	0.3448	0.2446
First Critical (rpm)	2400	2400	2400	2400
Radial Amplitude (in.)	1.522×10^{-4}	3.52×10^{-4}	5.252×10^{-5}	3.752×10^{-4}
Coefficient of Friction	0.15	0.15	0.15	0.15
Torque (in.-lb)	2000	2000	2000	2000
Radial Clearance (in.)	1.55×10^{-4}	3.5×10^{-4}	5.25×10^{-4}	3.75×10^{-4}
Shear Modulus (lb/in.^{2})	11.58×10^6	11.58×10^6	11.58×10^6	11.58×10^6
Space Width (in.)	0.1344	0.1344	0.1344	0.1344
Tooth Thickness, Ext. (in.)	0.1258	0.1258	0.1239	0.1239
Pitch Diameter	3.0	3.0	3.0	3.0
Minor Diameter, Ext. (in.)	2.871	2.871	2.83	2.83
Form Diameter, Ext. (in.)	2.910	2.910	2.91	2.91
Fillet Radius, Ext. (in.)	0.040	0.040	0.040	0.040
Major Diameter, Int. (in.)	3.084	3.084	3.170	3.170
Form Diameter, Int. (in.)	3.069	3.069	3.090	3.090
Fillet Radius, Int. (in.)	0.040	0.040	0.040	0.040

In addition to varying coupling parameters, changes in the test rig were explored for their effect on stability. The parameters which were varied, including those of both coupling and rig, are:

- Angular stiffness (κ) of the spline coupling

- Damping coefficients (b, β) of the coupling, varied together

- Stiffness of the damper bearing

- Damping coefficient of the damper bearing

- Running speed

- Diameter of the spline coupling "neck" (the reduced diameter transition piece from the main shaft to the external spline coupling half).

111

The results of this parametric study are presented in Table 5. The table shows, for each run of the stability program, which parameter was varied, the new value, and the resulting damped natural frequency and logarithmic decrement. Changes in the coupling stiffness and damping are given as the factor used for multiplying or dividing the nominal value; the others give the actual number used in place of the nominal. These nominal values are given for reference in Table 6.

Results of the computer runs made to describe spline coupling coefficients and stability analysis results are given in Tables 4 and 5. These results of the parametric study are also presented graphically in Figures 84 through 88. Figure 84 shows the variation of system log decrement with the damping coefficient of the damper bearing and illustrates just how small, for the otherwise nominal rig configuration, the damping must get to bring about instability. Figure 85 shows the variation in log dec with changes in the angular stiffness of the spline coupling. For this plot the bearing has been hard-mounted and damping reduced to a value of 2 lb-sec/in. Note that reducing the angular stiffness has a significant effect on stability. Stiffness could be reduced by shortening the length of engagement or crowning the coupling. The variation of system log dec with spline coupling damping coefficient is shown in Figure 86. The log dec is very insensitive to coupling damping until unrealistically high damping values are reached. Figure 87 shows that, for a low value of bearing damping and the spline damping increased by a factor of 100, increasing the damper bearing support stiffness causes the rig to go marginally unstable. Finally, Figure 88 shows the change in the natural frequency with spline angular stiffness for a lightly damped, stiff damper bearing.

The predicted first critical speed of the nonsynchronous whirl rig was 2376 rpm and, as shown in Figure 89, this calculated value is in very close agreement with the observed critical speed. Under nominal operating conditions the test rig was predicted to be marginally unstable if very low damping was present at the bearing supports. The experimental results showed that the rotor was slightly unstable with the side fit spline unlubricated, but by reducing the spline friction forces with lubricating oil the instability was suppressed. Also, as predicted with the rotor stability model, squeeze film damping the rig's thrust bearing eliminated the nonsynchronous whirl. Overall, there was close agreement between the predicted and measured response of the nonsynchronous whirl rig. A further description of the spline friction stability analysis can be found in References 21 and 22.

21 Tecza, J. A., "Stability Model and Analysis for Spline Coupling Induced Nonsynchronous Rotor Vibrations," Mechanical Technology Incorporated Report: MTI-78TR9, October 1977.

22 Tecza, J. A. "Stability Analysis of a Spline Coupling Test Pig," Mechanical Technology Incorporated Report: MTI-78TR78, May 1973.

TABLE 5
PARAMETRIC STUDY RESULTS
FOR SPLINE COUPLING TEST RIG

| | | Parameters Varied* | | | | | | Results | |
Run Number	Spline Angular Stiffness (From Nominal)	Spline Damping (From Nominal)	Bearing Stiffness (lb/in.)	Bearing Damping (lb-sec/in.)	Running Speed (rpm)	Spline Neck Diameter (in.)	Real Part of Eigenvalue (sec⁻¹)	Natural Frequency (cpm)	Log Dec
1							-4.155	2450	0.1017
2		÷100		0			3.496×10^{-4}	2444	-8.581×10^{-8}
3		×2		0			3.496×10^{-4}	2445	-8.581×10^{-8}
4		×10					-4.15	2450	0.1017
5		×100					-4.15	2450	0.1017
6		×300					-4.12	2450	0.1009
7						2.75	-4.05	2451	0.09917
8					4430		-4.34	2490	0.1046
9					3900		-4.10	2447	0.1005
10				0.25	4400		-4.04	2443	0.09922
11		×100		0.25	3900		0.0102	2441	-2.50×10^{-4}
12		×100		2			5.64×10^{-8}	2437	-1.388×10^{-4}
13		×100	750,000	0.25			0.0362	2660	-8.165×10^{-4}
14		×10		0.25			-0.02077	2444	5.098×10^{-4}
15		×30		0.25			-0.0176	2445	4.326×10^{-4}
16		×100		0.25			-0.0106	2445	2.610×10^{-4}
17		×100		2			0.0138	2445	-3.318×10^{-4}
18		×100		2			-0.134	2445	3.290×10^{-4}
19		×100	256,900	2			0.0198	2610	-4.552×10^{-4}
20			750,000	2			-1.46×10^{-8}	2660	3.29×10^{-4}
21	÷1.5		750,000	2			-1.03×10^{-8}	2655	2.33×10^{-4}
22	÷2.0		750,000				-3.80×10^{4}	2650	8.60×10^{-4}

*Spaces left blank indicate that the nominal value is retained.

113

TABLE 6
NOMINAL VALUES FOR PARAMETERS

Parameter	Nominal Value
Spline Angular Stiffness	3.3119×10^7 lb-in./radian
Spline Damping, Radial	123.47 lb-sec/in.
Spline Damping, Angular	47.143 in.-lb-sec/radian
Damper Bearing Stiffness	85,000 lb/in.
Damper Bearing Damping	50 lb-sec/in.
Running Speed	4900 rpm
Spline Neck Diameter	1.78 in.
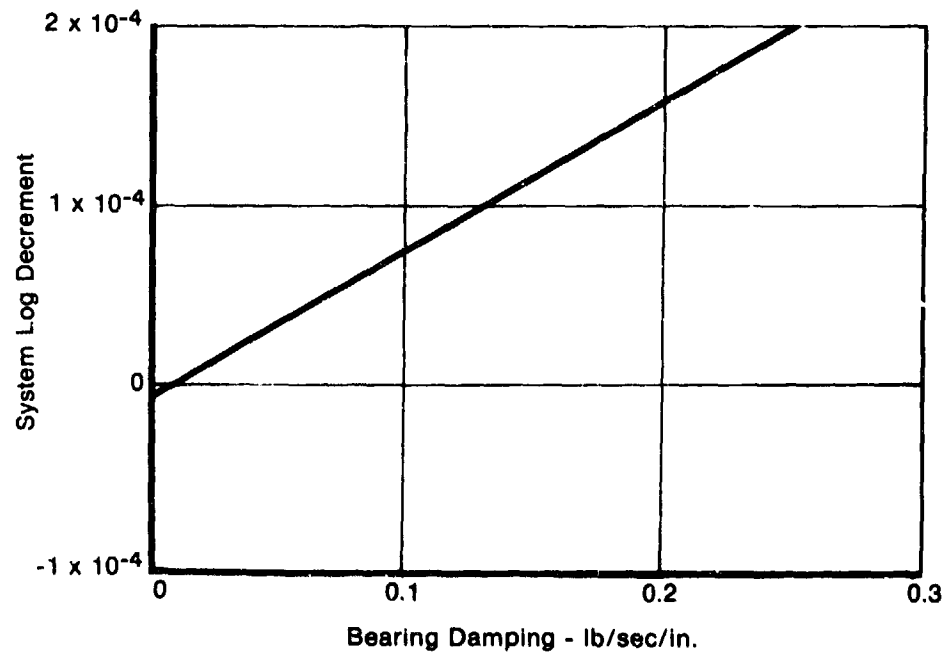
Figure 84. Variation of System Log Decrement With Bearing Damping
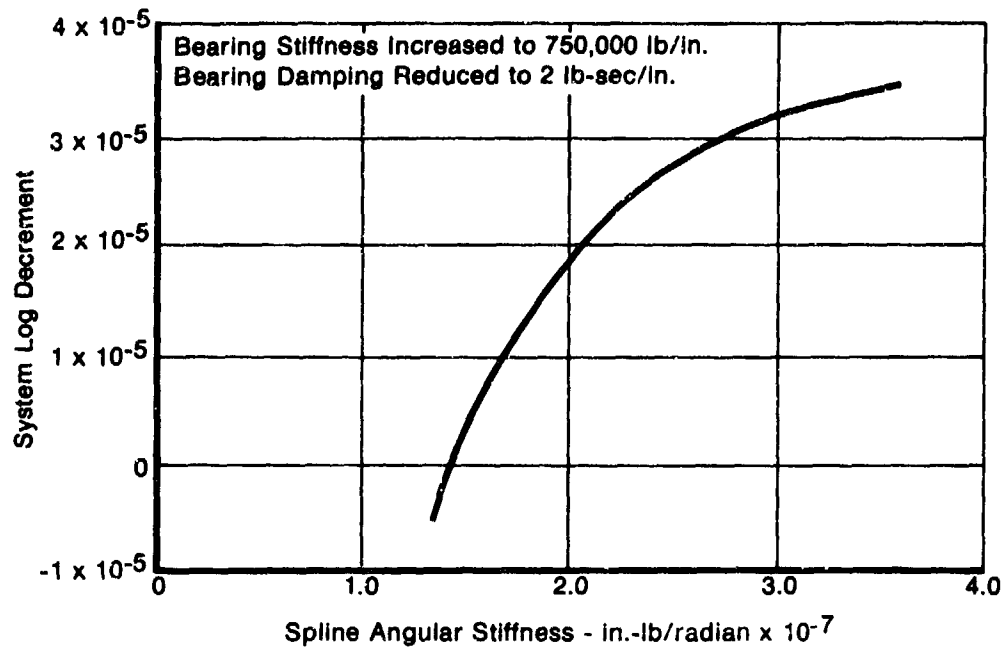
Figure 85. *Variation of System Log Decrement With Spline Angular Stiffness*
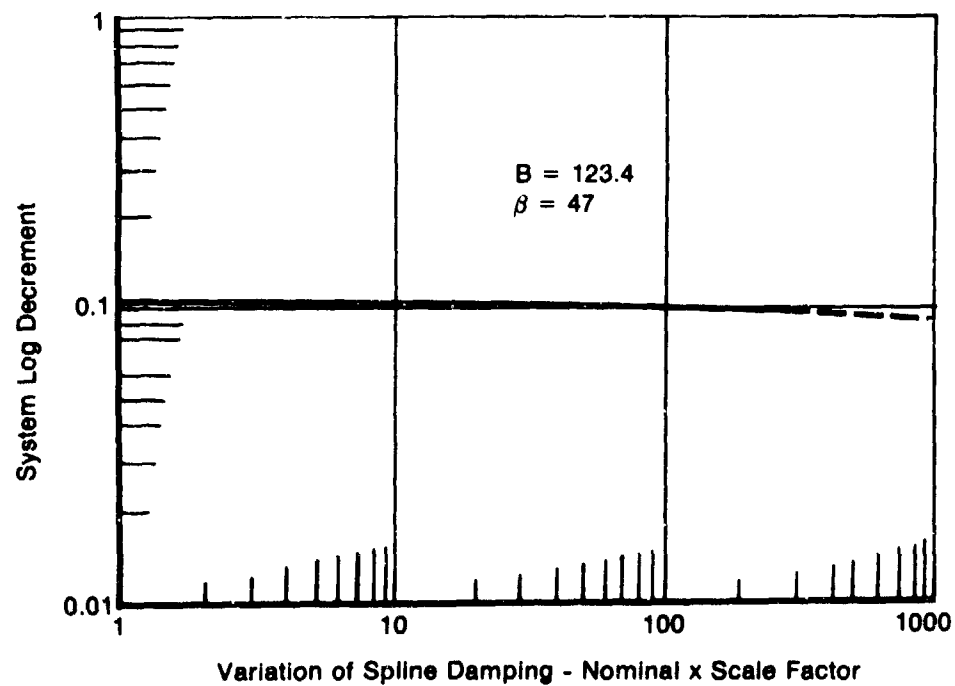
Figure 86. *Variation of System Log Decrement With Spline Damping*
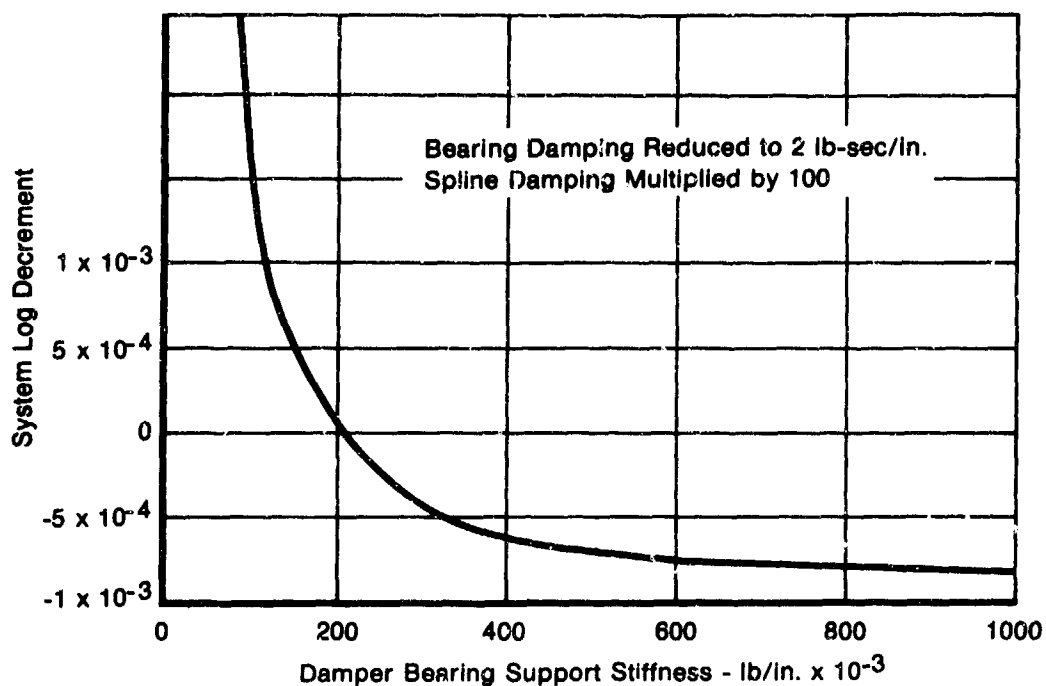
Figure 87. Variation of System Log Decrement With Bearing Stiffness
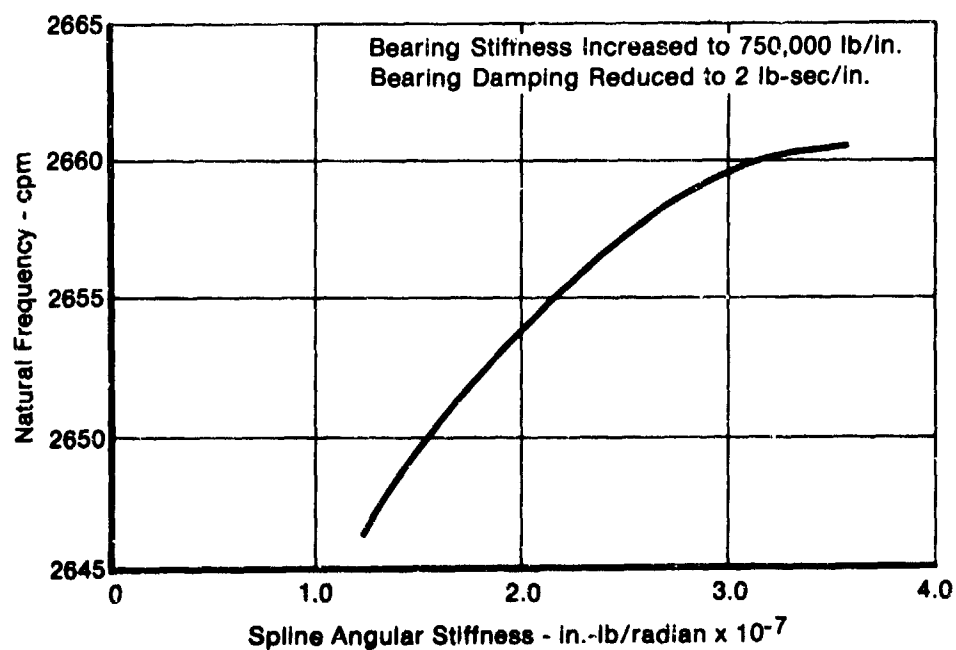
Figure 88. Variation of Natural Frequency With Spline Angular Stiffness

116
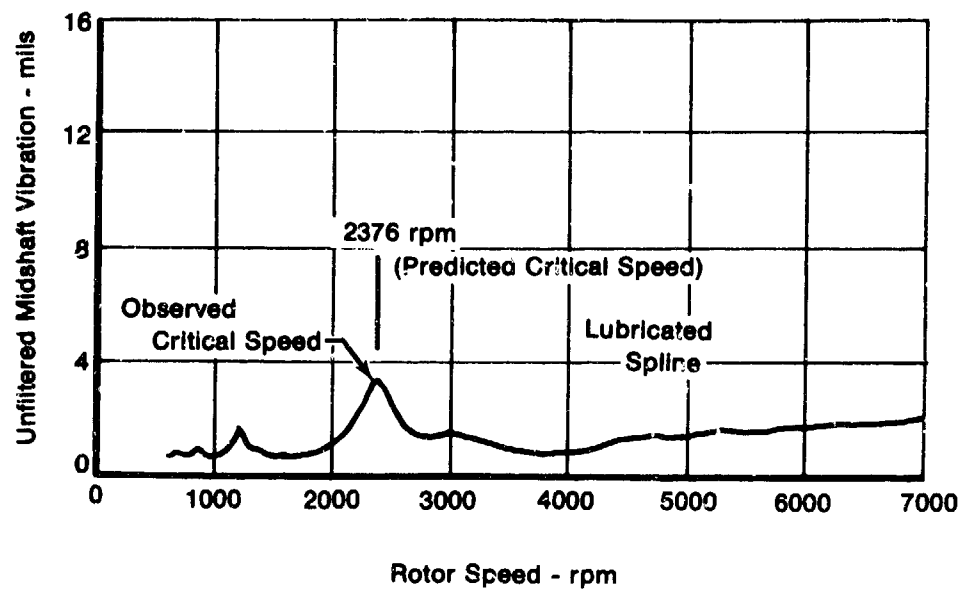
Figure 89. Nonsynchronous Whirl Rig Critical Speed Observed and Predicted

SECTION VI

ROTOR DESIGN OPTIMIZATION (TASK X)

At the conclusion of Tasks VI through IX the effects of five fundamental design variables (support stiffness, support damping, bumper clearance, spline geometry, and spline lubrication) on the dynamic characteristics of damped flexible rotor systems had been evaluated. Experimentally verified analytical methods had been developed and refined as a result. The dependent parameters which have been evaluated can be summarized under four general headings: performance, durability, stability, and survivability. The five design variables and the four dependent variables are most strongly interrelated, as shown in the matrix of Figure 90.

| | Response Variables | | | |
Design Variables	Performance (Aerodynamic Efficiency)	Durability (Bearing Life)	Rotor Stability (Internal Friction)	Survivability (Peak Transient Loads and Deflections)
a) Support System				
Stiffness	XX	XX	X	
Damping	X	X	XX	X
Bumper Clearance			X	X
b) Rotor				
Spline Geometry			XX	
Spline Lubrication			XX	

Figure 90. Pertinent Design Factors and Their Relevance to System Response

It is obvious that no single combination of design variables can produce the best response in all critical areas simultaneously. For example, the flexible support which is introduced to decrease dynamic bearing loads may dictate increased rotor/shroud clearance and consequent performance losses. Thus, the "best" design involves determining the most beneficial overall compromise. It is also obvious that the qualities that are most desirable are unique to each engine or rig because of its specific mission or function.

It is evident from Figure 90 that an efficient coordinated design system is required to determine the "best trade" design. This system was developed in Task X, and its organization is shown in Figure 91. Inherent in this system is the recognition that the term "optimization" applies to bearing life and aerodynamic efficiency effects. It is also recognized that these requirements are necessary but other considerations such as survivability are required for a truly optimized design.
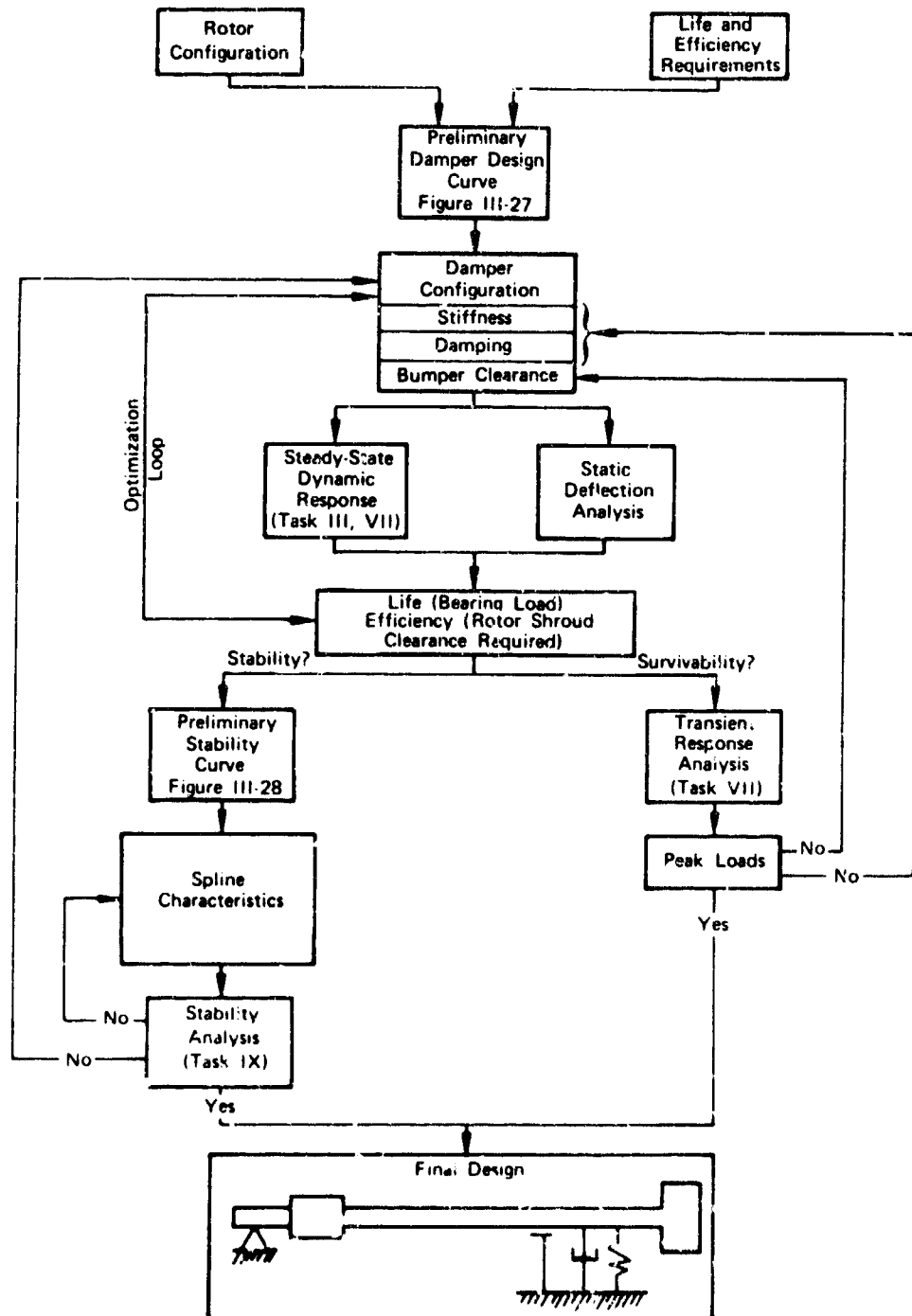
Figure 91. Design Optimization Method

The optimization procedure defined in Figure 91 can be separated into three tasks: (1) selection of preliminary bearing support damping and spline characteristics, (2) optimization of

damped support parameters to achieve maximum bearing life and to minimize rotor/shroud clearance using the damper analysis developed in Task I in conjunction with steady-state dynamic response and static deflection analyses, and (3) verification of stability using the Task IX spline analysis, and verification of survivability using a transient response analysis.

To establish a starting point for the optimized configuration, the following procedure is used. The rotor dynamic system consisting of rotor, bearings and bearing supports can be reduced to an approximate single mass rotor for analysis in the vicinity of the first shaft bending critical speed (Reference 23). This is accomplished by calculating the rigid support critical speeds of the rotor and estimating the equivalent rotor stiffness as follows:

$$K_z = M \, \omega_{cr}^2 \tag{142}$$

where M is the mass inertia of the rigid rotor and ω_{cr} is the first rigid support critical speed.

Assuming that the only damping in the system comes from the squeeze film damper, the equations of motion for the equivalent single mass system in a flexible damped bearing shown in Figure 92 are

$$M\ddot{X}_2 + K_z(X_2 - X_1) = Me\omega^2 e^{i\omega t} \tag{143}$$

$$C_1\dot{X}_1 + K_1X_1 + K_z (X_1 - X_2) = 0 \tag{144}$$

Figure 92. Equivalent Single Mass Rotor System

23 Barrett, L. E., E. J. Gunter, Allaire, "Optimum Bearing and Support Damping for Unbalance Response and Stability of Rotating Machinery," ASME Paper No. 77-GT-27.

Equations (143) and (144) are combined to form a single equation describing the dynamic motion of the mass:

$$M\ddot{X}_2 + C_{2e}\,\dot{X}_2 + K_{2e}\,X_2 = Me\omega^2 e^{i\omega t} \tag{145}$$

C_{2e} and K_{2e} are the effective damping and stiffness acting on the rotor mass. The expressions for effective damping and stiffness are as follows:

$$C_{2e} = \frac{K_2{}^2 C_1}{(K_1+K_2)^2 + (\omega C_1)^2} \tag{146}$$

$$K_{2e} = K_2 \left[\frac{K_1(K_1+K_2) + (\omega C_1)^2}{(K_1+K_2)^2 + (\omega C_1)^2} \right] \tag{147}$$

Equations (145), (146), and (147) can be nondimensionalized with respect to the following parameters:

$$\omega_{cr} = \sqrt{\frac{K_2}{M}}$$

$$\hat{\omega} = \sqrt{\frac{K_{2e}}{M}}$$

$$K = \frac{K_1}{K_2}$$

$$\xi_1 = \frac{C_1}{2M\omega_{cr}}$$

$$\xi_{2e} = \frac{C_{2e}}{2M\omega_{cr}}$$

$$f = \frac{\omega}{\omega_{cr}}$$

In dimensionless form, Equations (145), (146), (147) become

$$\ddot{X}_2 + 2\,\omega_{cr}\,\xi_{2e}\,\dot{X}_2 + \hat{\omega}^2\,X_2 = e_u\,\omega^2\,e^{i\omega t} \tag{148}$$

$$\xi_{2e} = \frac{\xi_1}{(1 + K)^2 + (2f\xi_1)^2} \tag{149}$$

$$\hat{\omega}^2 = \omega_{cr}^2 \left[\frac{K(1 + K) + (2f\xi_1)^2}{(1 + K)^2 + (2f\xi_1)^2} \right] \tag{150}$$

121

The optimum value of bearing damping ratio maximizes the effective damping ratio, ξ_{2e}, and the optimum bearing damping is given by

$$\xi_{1o} = \frac{(1 + K)}{2f} \tag{151}$$

and the maximum effective damping ratio is given by

$$\xi_{2em} = \frac{1}{4f(1 + K)} \tag{152}$$

Since for supercritical speed flexible rotors the frequency ratio f is unity, the expression for optimum damping ratio is

$$\xi_{1o} = \frac{1 + K}{2} \tag{153}$$

and for maximum effective damping ratio is

$$\xi_{2em} = \frac{1}{4(1 + K)} \tag{154}$$

The optimum damping ratio is plotted in Figure 93 for determining preliminary optimum damping coefficients.
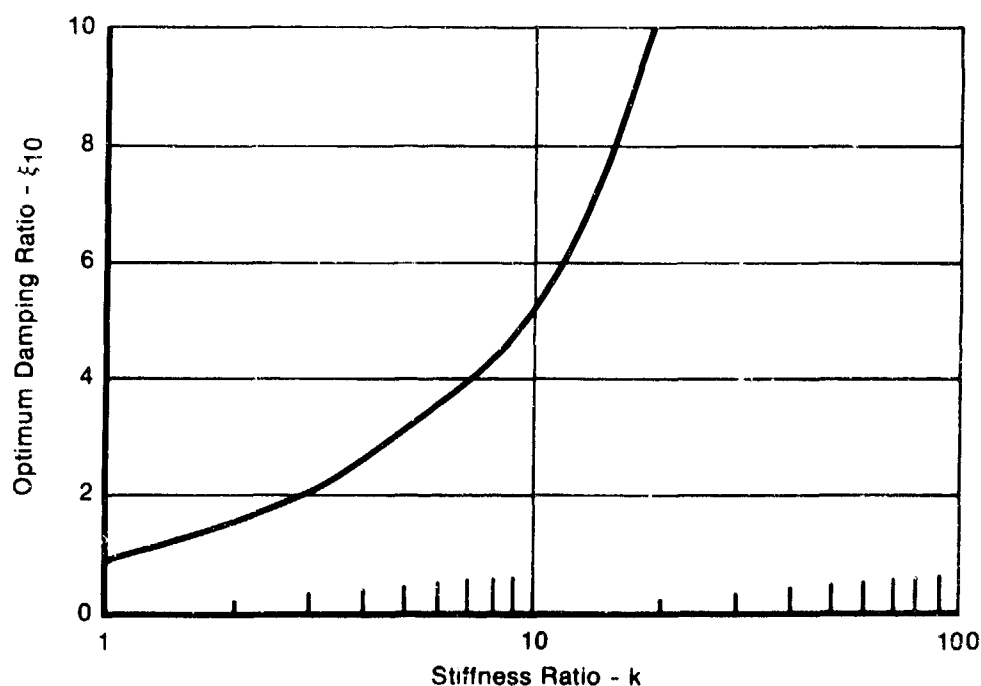
Figure 93. Preliminary Damper Design Curve

122

For free damped vibrations with internal viscous friction damping such as spline friction, Equation (148) becomes

$$\ddot{X}_2 + 2\omega_{cr}(\xi_{2oM} + \xi_a)\dot{X}_2 + (\hat{\omega}^2 - 2i\omega_{cr}\omega\,\xi_a)\,X = 0 \tag{155}$$

where ξ_a is the internal spline friction damping ratio, defined as

$$\xi_a = \frac{C_a}{2M\omega_{cr}} \tag{156}$$

C_a is the spline coupling damping coefficient, which can be calculated using the spline friction model developed in Task VIII.

The solution of the eigenvalues of Equation (155) reveals that the rotor system will only be stable if the operating speed, ω, is

$$\omega < \frac{\omega_{cr}}{(1+K)^2}\left[\frac{1+2K}{2}\right]^{1/2}\left[1 + \frac{K+1}{4\xi_a}\right] \tag{157}$$

The maximum stable speed ratio, ω/ω_{cr}, at which the rotor can operate with optimum support damping is plotted in Figure 94 for determining preliminary rotor stability.
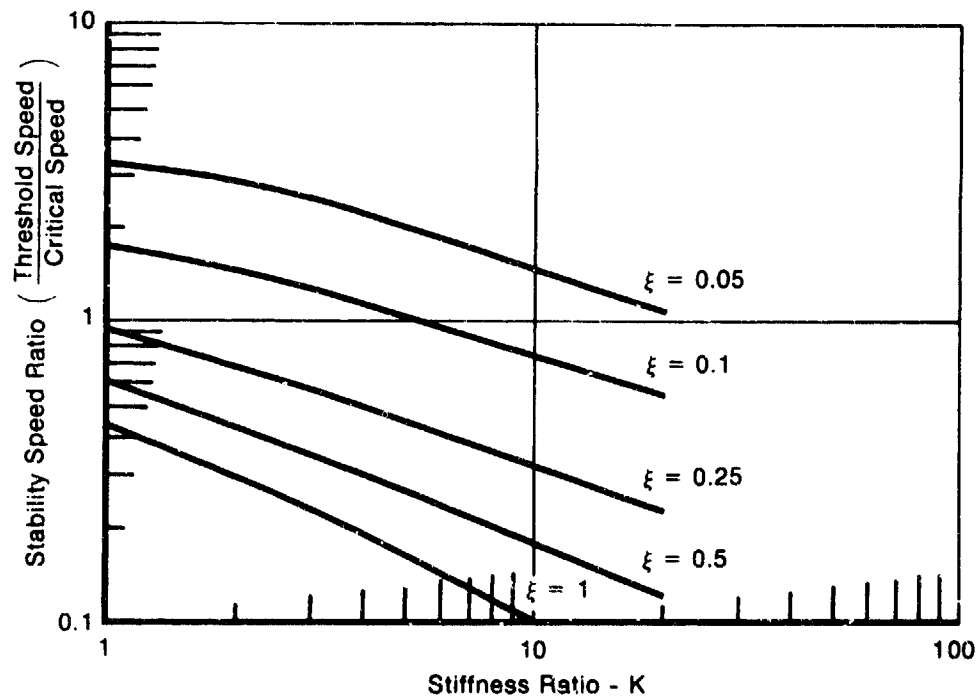
Figure 94. Preliminary Rotor Stability Curve

For transient blade loss excitation, Equation (148) can be separated into an x and y direction and the equations can be solved by the method of convolution as in Reference 24. Equation (148) becomes

$$\ddot{X}_s + 2\,\omega_{cr}\,\xi_{2e}\,\dot{X}_s + \hat{\omega}^2\ X_s = e_u\,\omega^2\cos\omega t \tag{158}$$

and

$$\ddot{Y}_s + 2\,\omega_{cr}\,\xi_{2e}\,\dot{Y}_s + \hat{\omega}^2\ Y_s = e_u\,\omega^2\sin\omega t \tag{159}$$

The maximum transient blade loss amplitude is predicted by calculating the maximum resultant x,y amplitude, R, by the use of the convolution integral:

$$R = \sqrt{X_s^2 + Y_s^2} \tag{160}$$

$$X_s = \frac{1}{\hat{\omega}}\int_0^t e_u\omega^2\cos(\omega\tau)e^{-\xi_{2e}\hat{\omega}(t-\tau)}\sin\hat{\omega}(t-\tau)d\tau \tag{161}$$

$$Y_s = \frac{1}{\hat{\omega}}\int_0^t e_u\omega^2\sin(\omega\tau)e^{-\xi_{2e}\hat{\omega}(t-\tau)}\sin\hat{\omega}(t-\tau)d\tau \tag{162}$$

The solutions to Equations (160), (161), and (162) are plotted in Figure 95 as the ratio of maximum transient amplitude to steady-state amplitude versus speed ratio. The curve will be used for determining the preliminary rotor transient response to a sudden blade loss unbalance.

The final result of using the preliminary design curves of Figures 93 through 95 and the design optimization method of Figure 91 will be the definition of a power turbine rotor dynamic system which (1) has the best possible combination of bearing life and aerodynamic efficiency, (2) is stable at all operating speeds, and (3) can absorb blade loss loads without damage to the engine.

24 Dimentberg, F. M.,"Flexural Vibrations of Rotating Shafts,"Pages 50-53, Butterworths, London, 1961.
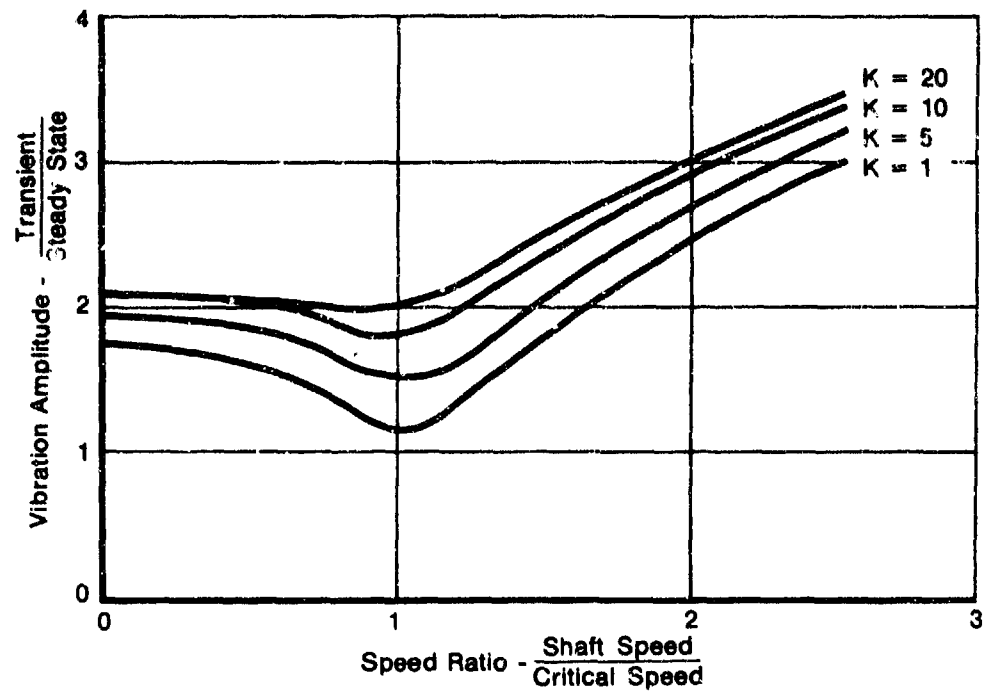
Figure 95. Preliminary Transient Response Curve

SECTION VII

CONCLUSIONS AND RECOMMENDATIONS

The engine rotor dynamics contract contained an aggressive analytical and complementary experimental program to develop the technology required for designing future high speed turboshaft engines with optimum rotor dynamic performancce. The design/prediction system which has been developed can be used to design future gas turbine engine rotors to have improved efficiency, durability, and survivability.

The squeeze film damper characteristics studied were analytically predicted and experimentally verified to be strongly dependent on damper end-seal leakage and inlet feedback. The damper mathematical model developed demonstrated the accuracy and versatility necessary to design an effective squeeze film damper with any combination of end seal and inlet configurations commonly used in gas turbine engines. However, to effectively use this damper model, additional damper test rig data is required which will quantify the leakage characeristics and parametrically determine the best type of end seal for gas turbine engine applications. Also, a faster solution procedure for the damper model should be pursued in order to improve computational efficiency for transient response analyses of squeeze film damped rotors.

Mechanical impedance testing of three types of flexible bearing supports revealed that satisfactory accuracy for estimating support stiffness can be accomplished with existing beam theory formulations. If a maximum error of 20% cannot be tolerated, then a more precise modeling technique such as a finite element method should be used.

The synchronous whirl studies verified that a properly designed, squeeze film damped, supercritical rotor can have acceptable imbalance sensitivity and can sustain transient blade loss imbalance loads without damage to the rotor system. The existing analytical models used to predict the steady-state and transient dynamic response of synchronous whirl rig gave marginally satisfactory results. It is recommended that improved computational procedures be investigated in order to reduce the numerical errors that exist in commonly used engine rotor dynamic models.

The nonsynchronous whirl studies verified that rotors which are coupled with nonlubricated spline couplings are prone to internal friction rotor instability. Lubricating the spline coupling or squeeze film damping the bearing supports has a stabilizing effect on the rotor. Furthermore, squeeze film damping can reduce the steady-state vibration amplitude at the critical speed by as much as 50%.

While it is felt that the analytical models developed under this program along with existing rotor dynamic models give satisfactory agreement with experimental rig data, the analytical prediction system can be further improved with additional calibration of the squeeze film damper with empirical damper seal leakage data from parametric rig tests of commonly used seals. Also, the computational precision of the commonly used steady-state and transient response rotor dynamic models for flexible rotor gas turbine engines should be modified to use improved numerical methods such as those discussed in References 25 and 26.

25 Horner, G. C., Pilkev "The Riccati Transfer Matrix Method," ASME Paper No. 77-DET-32, 1977.

26 Lund, J. W., "Model Response of a Flexible Rotor in Fluid-Film Bearings," ASME, Journal of Engineering for Industry, page 525, May 1974.

REFERENCES

1. Hori, Y., "A Theory of Oil Whip," Journal of Applied Mechanics, Trans. ASME, June 1959.

2. Tondl, A.,"Some Problems in Rotor Dynamics,"Chapman and Hall Limited, London, England, 1965, pp. 122-130.

3. Feder, E., Bansal P. N. and Blanco, A., "Investigation of Squeeze Film Damper Forces Produced by Circular Centered Orbits," presented at the Gas Turbine Conference, Philadelphia, Pa., March 27-31, 1977, ASME Paper No. 77-GT-27.

4. Vance, J. M., and Kirton, A. J. "Preliminary Investigation of the Dynamic Force Response Coefficients for Squeeze Film Bearing Dampers," U.S. Army Research Office, Grant Number DAHCO4-74-6-0048, November 1974.

5. Jones, M. G., "An Experimental Investigation of Squeeze Film Hydrodynamics," Report No. R. 320, National Gas Turbine Establishment, Ministry of Defense (England), January 1973.

6. King, H. H., "A Poisson Equation Solver for Rectangular or Annular Regions," International Journal for Numerical Methods in Engineering, Vol. 10, 1976, pp. 799-807.

7. Trumpler, P. R.,"Design of Film Bearings,"MacMillan Co., New York, 1966, p. 30.

8. Pinkus, O., and Sternlicht, B.,"Theory of Hydrodynamic Lubrication,"McGraw-Hill, Inc., New York, 1961, pp. 80-81.

9. Botman, M., "Experiments on Oil-Film Dampers for Turbomachinery," Journal of Engineering for Power, Trans. ASME, Series A, Vol. 98, July 1976, pp. 393-399.

10. Lund, J. W., and Orcutt, F. K., "Calculations and Experiments on the Unbalance Response of a Flexible Rotor," ASME Paper No. 67-Vibr-27.

11. Dennis, A. J., Eriksson, R. H., and Seitelman, L. H., "Transient Response Analysis of Damped Rotor Systems by the Normal Mode Method," ASME Paper No. 75-GT-58.

12. Williams, R., and Trent, R., "The Effect of Non-Linear Asymmetric Supports on Turbine Engine Rotor Stability," SAE 700320.

13. Lund, J. W., "Stability and Damped Critical Speeds of a Flexible Rotor in Fluid Film Bearings," Journal of Engineering for Industry, Trans. ASME, Series B, Vol. 96, No. 2, May 1974, pp. 509-517.

14. Laskin, I., et al., "Analysis of Noise Generated by UH-1 Helicopter Transmission," USAAVLABS Technical Report 68-41, June 1968, Available through Clearinghouse, Springfield, Va. 22151, Report No. AD 675458.

15. Walowit, J. A., and Anno, J. N., "Modern Developments in Lubrication Mechanics," Applied Science Publishers, Ltd. London, 1975.

16. O'Donnel, W. J., "Stress and Deflection in Built-In Beams," ASME Paper No. 62-WA-16, 1962.

REFERENCES (Continued)

17. Rabinowitz, E.,"Frictional and Wear Materials,"John Wiley and Sons, New York, 1965.

18. Benedict, G. H., and Kelly, B. W.,"Instantaneous Coefficients of Gear Tooth Friction,"ASLE Transactions 4, 59-70, 1961.

19. Boyland, W.,"Marine Application of Dental Couplings,"Soc. Nav. Arch. and Nav. Engrs. Marine Power Plant Symposium, Paper 26, May 1966.

20. Crease, A. B.,"Design Principles and Lubrication of Gear Couplings," International Conference on Flexible Couplings for High Powers and Speeds, University of Sussex, England, June 28 to July 1, 1977, Paper B1.

21. Tecza, J. A., "Stability Model and Analysis for Spline Coupling Induced Nonsynchronous Rotor Vibrations," Mechanical Technology Incorporated Report: MTI-78TR9, October 1977.

22. Tecza, J. A., "Stability Analysis of a Spline Coupling Test Rig," Mechanical Technology Incorporated Report: MTI-78TR78, May 1978.

23. Barrett, L. E., Gunter E. J., Allaire P., "Optimum Bearing and Support Damping for Unbalance Response and Stability of Rotating Machinery," ASME Paper No. 77-GT-27.

24. Dimentberg, F. M.,"Flexural Vibrations of Rotating Shafts,"Pages 50-53, Butterworths, London, 1961.

25. Horner, G. C., Pilkey, "The Riccati Transfer Matrix Method," ASME Paper No. 77-DET-32, 1977.

26. Lund, J. W., "Model Response of a Flexible Rotor in Fluid-Film Bearings," ASME, Journal of Engineering for Industry, page 525, May 1974.

APPENDIX A

DAMPER ANALYSIS BY NUMERICAL DIFFERENTIATION AND INTEGRATION

1.0 GENERAL INFORMATION

This document contains the operating instructions for the Damper Analysis by Numerical Differentiation and Integration (DANDI) Computer Program developed under Contract DAAJ02-76-C-0011, Engine Rotor Dynamics. Descriptions of input and output program data are provided along with flow diagrams.

> *Program:* Damper Analysis by Numerical Differentiation and Integration (DANDI)
>
> *Language:* FORTRAN IV/Level 221
>
> *Computer Configuration:* IBM 370/168
>
> *Operating System:* OS 370, Release 3.7VS
>
> *Estimated Running Time:* 0.2 sec CPU time
>
> *Program Author:* Ronald A. Marmol, Pratt & Whitney Aircraft Group, P. O. Box 2691, West Palm Beach, Florida 33402

2.0 INPUT DESCRIPTION

Figure A-1 is a sample data input form showing the data input format. Table A-1 lists the input data definition.

3.0 OUTPUT DESCRIPTION

Table A-2 lists the output data definition. Figure A-2 is a flow chart for the computer program and Figure A-3 is a logic flow diagram for choosing boundary condition subroutines.

Figure A-1. Data Input Format

130

Figure A-1. Data Input Format (Continued)

TABLE A-1
INPUT DATA DEFINITION

Card No.	Cols.	Type			Description
1.	1-80	A.N.			Any descriptive title information.
2.	1-10	F.P.	RB	=	Radius of bearing (in.).
	11-20	F.P.	C	=	Damper bearing clearance (in.).
	21-30	F.P.	EL	=	Damper bearing length (in.).
	31-40	F.P.	ELI	=	Axial dimension from the inlet plane to the closest end (in.). If the damper has symmetry, it must have the inlet centered between identical end conditions.
	41-44	Int.	NI	=	Type of inlet (right adjusted with no decimal point).
				=	0 or left blank for no inlet.
				=	1 for single inlet hole with backflow.
				=	2 for two inlet holes 180 deg apart.
					•
					•
					•
				≥	100 for circumferential groove.
	46	Int.	NS1	=	Type of end seal at $Z=0.0$ (right adjusted with no decimal point).
				=	1 for piston ring seal.
				=	2 for radial O-ring seal.
				=	3 for side O-ring seal.
				=	4 for no seal.
	48	Int.	NS2	=	Type of end seal at $Z=L$ (right adjusted with no decimal point). Same options as NS1 above.
	50	Int.	NSYMM	=	Symmetry option (right adjusted with no decimal point).
				=	0 or left blank for no symmetry.
				=	1 for inlet centered between two identical end seals (NI ≠ 0).
	52	Int.	ITERM	=	Simplified equation option (right adjusted with no decimal point).
				=	0 or left blank for complete equations to be used.
				=	1 for simplified equations to be used for F1, F3 and F4.
3.	1-15	F.P.	EMU	=	Lubricant viscosity (lb-sec/in.**2).
	16-30	F.P.	RPM	=	Shaft speed (rpm).
	31-45	F.P.	PSUPLY	=	Supply pressure (psi). Must be non-zero.
	46-60	F.P.	PEXIT	=	Exit pressure (psi).
	61-75	F.P.	PCAV	=	Cavitation pressure (psi).

Card No.	Cols.	Type		Description
4.	1-4	Int.	M =	Number of circumferential grid points. Right adjusted with no decimal point. Even Number — Maximum of 60.
	5-8	Int.	N =	Number of axial grid points. Right adjusted with no decimal point. Odd number. If NSYMM = 0, Use $5 \leq N \leq 15$. If NSYMM = 1, Use N = 9, 13, 17, 21, 25, or 29.
	9-12	Int.	IOP =	Solution option (right adjusted with no decimal point).
			=	1 for transient damper forces (FX and FY).
			=	2 for linearized squeeze film stiffness (K), squeeze film damping (C), and damper offset (EP).
			=	3 for Tondl coefficients (F1, F2, F3, and F4).
			=	4 for Lund damping coefficients (CXX, CXY, CYX, and CYY).
			=	5 for transient damper forces (FX and FY) and grid point pressures.

If IOP = 4, input the following card No. 5.

5.	1-15	F.P.	ϵX =	Dimensionless journal position (X/C).
	16-30	F.P.	ϵY =	Dimensionless journal position (Y/C).
	31-45	F.P.	$\Delta\epsilon X$ =	Dimensionless journal velocity (VX/WC).
	46-60	F.P.	$\Delta\epsilon Y$ =	Dimensionless journal velocity (VY/WC).
6.	1-15	F.P.	CP =	"Loss coefficient" for flow through the radial gap around the piston ring seal. $0.0 \leq CP \leq 1.0$
	16-30	F.P.	HS =	Radial gap around the piston ring seal (in.).
	31-45	F.P.	WP =	Width (axial dimension) of the piston ring (in.).
7.	1-15	F.P.	COR =	Flow coefficient for O-ring seal (in.**3/sec) / (psi-in).
	16-30	F.P.	HOR =	Radial thickness of O-ring as installed in groove (in.).
	31-45	F.P.	CKOR =	O-ring stiffness — axial defl. / psi. (in./psi).
8.	1-15	F.P.	CI =	Flow coefficient for one inlet hole (in.**3/sec) / psi.

133

TABLE A-2
OUTPUT DATA DEFINITION

Printout	Description
(Title)	Any descriptive title information.
Bearing Radius Inches	Radius of bearing (in.).
Damper Bearing Clearance Inches	Damper bearing clearance (in.).
Axial Dimension From Inlet Plane to Closest End Inches	Axial dimension from the inlet plane to the closest end (in.). If the damper has symmetry, it must have the inlet centered between identical end conditions.
Inlet Type	Type of inlet 0 or left blank for no inlet. 1 for single inlet hole with backflow. 2 for two inlet holes 180 deg apart. ● ● ● 100 for circumferential groove.
Z=0 End Seal Type	Type of end seal at Z=0.0 1 for piston ring seal. 2 for radial O-ring seal. 3 for side O-ring seal. 4 for no seal.
Z=L End Seal Type	Type of end seal at Z=L. Same options as NS1 above.
Symmetry Option	Symmetry option. 0 or left blank for no symmetry. 1 for inlet centered between two identical end seals ($NI \neq 0$).
Equation Option	Simplified equation option. 0 or left blank for complete equations to be used. 1 for simplified equations to be used for F1, F3 and F4.
Lubricant Viscosity lb-sec/in.**2	Lubricant viscosity (lb-sec/in.**2).
Shaft Speed rpm	Shaft speed (rpm).
Supply Pressure psi	Supply pressure (psi). Must be non-zero.

134

Printout	Description
Exit Pressure psi	Exit pressure (psi).
Cavitation Pressure psi	Cavitation pressure (psi).
Number of Circumferential Grid Points	Number of circumferential grid points. Even number — maximum of 60.
Number of Axial Grid Points	Number of axial grid points. Odd number. If NSYMM = 0, Use $5 \leq N \leq 15$. If NSYMM = 1, Use N = 9, 13, 17, 21 25, or 29.
Solution Option	1 for transient damper forces (FX and FY). 2 for linearized squeeze film stiffness (K), squeeze film damping (C), and damper offset (EP). 3 for Tondl coefficients (F1, F2, F3, and F4). 4 for Lund damping coefficents (CXX, CXY, CYX, and CYY). 5 for transient damper forces (FX and FY) and grid point pressures.

If Solution Option = 1 or 5

Journal Position

X	X position of the damper journal center (in.).
Y	Y position of the damper journal center (in.).

Journal Velocity (inches/sec)

VX	Velocity of the damper journal center in the X direction (in./sec).
VY	Velocity of the damper journal center in the Y direction (in./sec).

If Solution Option = 2

Damper Static Load lb	Damper static load (lb).
Whirl Eccentricity Inches	Whirl eccentricity (in.).
Mechanical Spring Stiffness lb/in.	Mechanical spring stiffness (lb/in.).

Printout	Description
	If Solution Option = 3
Radial Velocity Inches/sec	Radial velocity (in./sec).
Damper Eccentricity Inches	Damper eccentricity (in.).
	If Solution Option = 4
Dimensionless Journal Position	
Y/C	Dimensionless journal position (X/C).
Y/C	Dimensionless journal position (Y/C).
Dimensionless Journal Velocity	
VX/WC	Dimensionless journal velocity (VX/WC).
VY/WC	Dimensionless journal velocity (VY/WC).
	For Solution Option = 1, 2, 3, 4, or 5
Piston Ring Seal Loss Coefficient	'Loss coefficient' for flow through the radial gap around the piston ring seal. $0.0 \leq CP \leq 1.0$
Piston Ring Seal Radial Gap Inches	Radial gap around the piston ring seal (in.).
Piston Ring Width Inches	Width (axial dimension) of the piston ring (in.).
O-Ring Seal Flow Coefficient (in.**3/sec)/(psi·in.)	Flow coefficient for O-ring seal (in.**3/sec)/(psi-in.).

Printout	Description
O-Ring Radial Thickness Inches	Radial thickness of O-ring as installed in groove (in.).
O-Ring Stiffness in./psi	O-ring stiffness = axial defl./psi (in./psi).
Inlet Hole Flow Coefficient (in.**3/sec)/psi	Flow coefficient for one inlet hole (in.**3/sec)/psi.
EPS	(whirl eccentricity)/(damper bearing clearance)
PHI	Damper angular position in clearance circle (radians).
EDOT	Radial velocity of damper.
PHIDOT	Whirl velocity of damper.
DEPSDT	(Radial velocity of damper)/(bearing clearance × shaft angular velocity)
DPHIDT	(Whirl velocity of damper)/(shaft angular velocity)
PS	(Supply pressure)*C**2/(6.0 * RMU * OMEGA * RB **2)
PE	(Exit pressure)*C**2/(6.0 * EMU * OMEGA * RB **2)
OMEGA	(Shaft rpm) * π/30.

If Solution Option = 1

Printout	Description
FX	Resulting damper force in the horizontal direction.
FY	Resulting damper force in the vertical direction.

If Solution Option = 2

Printout	Description
Squeeze Film Stiffness lb/in.	Damper stiffness coefficient for circular whirl.
Squeeze Film Damp lb-sec/in.	Damper damping coefficient for circular whirl.
Damper Offset Inches	Damper offset from center of clearance circle due to static loading.

Printout	Description
	If Solution Option = 3
F1	Tondl coefficients as defined by Reference 2.
F2	
F3	
F4	
	If Solution Option = 4
CXX	Linear damping coefficients as defined by Lund.
CXY	
CYX	
CYY	
	If Solution Option = 5
	Finite difference grid point pressures are printed
FX	Resulting damper force in the horizontal direction.
FY	Resulting damper force in the vertical direction.

I.   Input   Data
$\omega\ \mu\ R_b,\ C,\ L,\ L_1,\ P_s,\ P_e,\ C_l$
M, w, X_J, Y_J, $\dot{X}_J$, $\dot{Y}_J$, C_p, h_s, C_{OR}, K_{OR}, h_{OR}
Inlet No. "NI", Seal No. NS1, NS2
NSYMM (Axial Symmetry)

II.   Calculate π Groups, Position, Motion, Digitize ψ (J), H(J)
$\epsilon,\ \dfrac{d}{dT},\ \phi,\ \dfrac{d\phi}{dT},\ \dfrac{C}{R_j},\ \dfrac{C}{R_b},\ \dfrac{R_j}{R_b}$

III.   Calculate All Matrix Elements (Except End Boundary Rows) from Reynold's Equation, A_{jk}, and Right Side Vector

Call Proper Subroutines   (See Logic Diagram)

IV.   Calculate Matrix Elements for Boundaries at Each End (Seals), and at Inlet

Return

V.   Print Out Matrix Elements A_{jk} and Solution Vector PJK

Figure A-2. Computer Program Flow Chart

139

```
┌─────────────────────────────────────────────────┐
│               Is NSYMN = 1?                      │
└─────────────────────────────────────────────────┘
    │                                    │
  ┌─────┐                             ┌─────┐
  │ Yes │                             │ No  │
  └─────┘                             └─────┘
    │                                    │
    ▼                                    ▼
┌───────────────┐                 ┌───────────────┐
│   Symmetry    │                 │  No Symmetry  │
└───────────────┘                 └───────────────┘
    │                                    │
    ▼                                    ▼
┌───────────────┐                 ┌─────────────────────┐
│ Disregard NS1 │                 │ NS1 Determines BₒCₒ │
│               │                 │ Subroutine for Z = 0│
└───────────────┘                 └─────────────────────┘
    │                                    │
    ▼                                    ▼
┌─────────────────────┐           ┌─────────────────────┐
│ NS2 Determines BₒCₒ │           │ NS2 Determines BₒCₒ │
│ Subroutine for Z = L│           │ Subroutine for Z = L│
└─────────────────────┘           └─────────────────────┘
    │                                    │
    ▼                                    ▼
┌─────────────────────┐           ┌─────────────────────┐
│      KI1 = 1        │           │      KI1 = N1       │
│ Puts Inlet at Z = 0 │           │ Puts Inlet at Z = L₁│
└─────────────────────┘           └─────────────────────┘
    │                                    │
    ▼                                    ▼
┌─────────────────────┐           ┌─────────────────────┐
│  NI Determines BₒCₒ │           │  Ni Determines BₒCₒ │
│      for Inlet      │           │      for Inlet      │
└─────────────────────┘           └─────────────────────┘
```
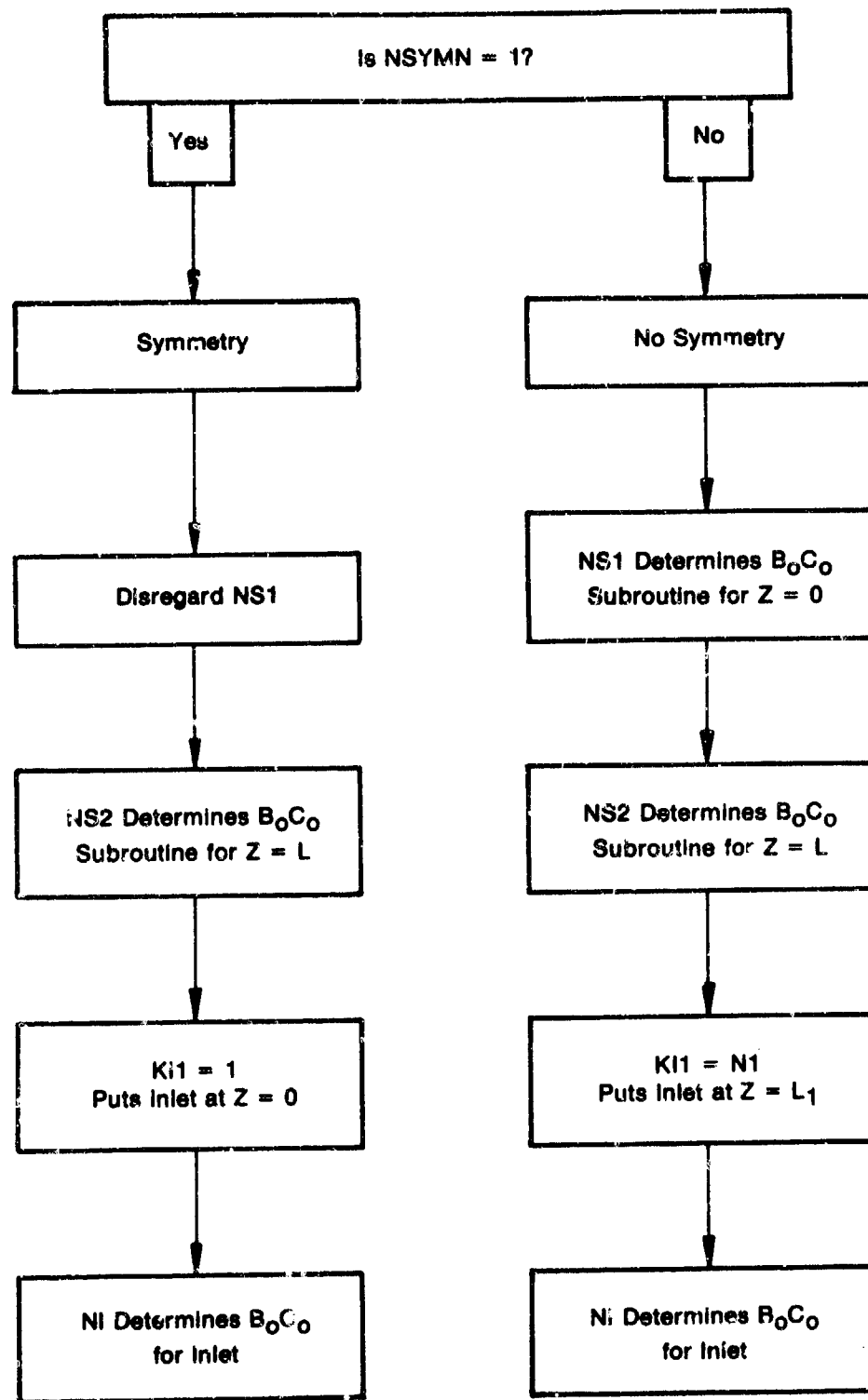
Figure A-3. Computer Flow Logic Diagram for Choice of Boundary Condition Subroutines

APPENDIX B
SPLINE COUPLING ANALYSIS PROGRAM

1.0 GENERAL INFORMATION

Program: Spline Coupling Analysis Program

Language: FORTRAN IV/Level 221
Computer Configuration: IBM 360/370
Operating System: SCOPE 3.4
Estimated Running Time: 0.5 sec CPU time
Program Author: Judith Hutchison, Joseph A. Tecza, Mechanical Technology Inc.
968 Albany Shaker Rd., Latham, N.Y. 12110

2.0 INPUT DESCRIPTION

The computer software developed for this project consists of a main program and five subroutines: SPLININ, SPLINE, SPLOUT, OUTLINE, and QB. The subroutines are designed to be inserted into a rotor dynamics program which is simulated by the short main program. The total input (exclusive of control cards) consists of seven cards — three read by the main program and the remaining four by subroutine SPLININ. These cards are described in the subsections which follow.

2.1 Main Program Input

Program MAIN, which calls SPLININ and SPLINE, requires three inputs, supplied by 3 cards. The quantities in parentheses indicate the card formats.

Card 1 — Title Card

TITLE (I), I=1,8   (8 A10)

Card 2 — Type of Fit

IFIT = 1 for major diameter fit   (16I5)
= 2 for side fit

Card 3 — Operating Speed

SPEED (rpm)   (8E10.3)

2.2 Subroutine SPLININ Input

Card 1 — Integer Controls   (16I5)

NT   — the number of tooth pairs in the coupling.

NK1   — the number of sections into which the external tooth is divided for analysis (must be ≤25; 10 recommended).

141

NK2 — the number of sections into which the internal tooth is divided for analysis (must be ≤25; 10 recommended).

Many of the dimensions referred to on the following cards are described in the standard *INVOLUTE SPLINES AND INSPECTION*, ANSI B92.1, 1970, English Version, Published by Society of Automotive Engineers, Inc., Two Pennsylvania Plaza, N.Y., N.Y. 10001.

Card 2 (8E10.3)

PSI — pressure angle at pitch radius (degrees).

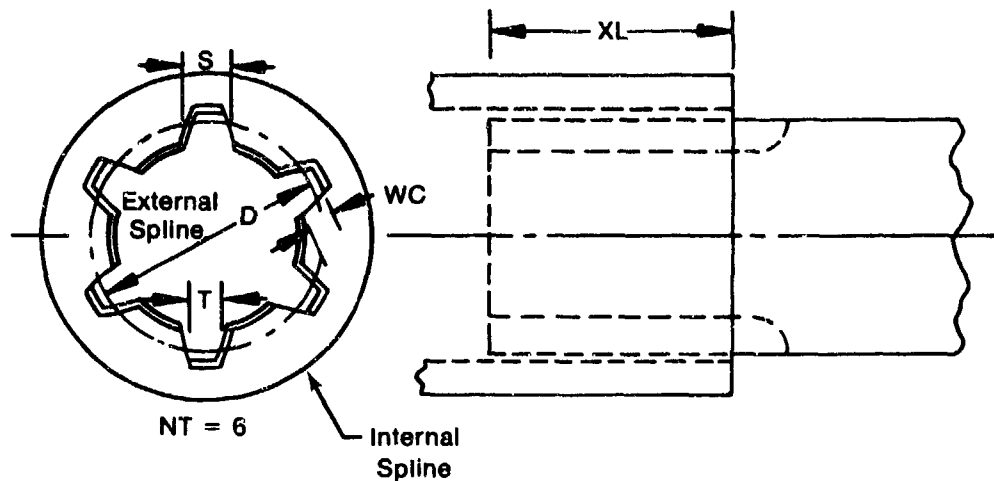XL — face width (inches). See figure B-1 for detail view.

Figure B-1. Views of Spline Coupling

EMOD — Young's modulus (lb/sq in.).

XNU — Poisson's ratio.

WC — width of contact patch (inches). This is the radial distance along which contact occurs between male and female teeth. For involute spline teeth it is the difference in form radii of the external and internal spline teeth.

EPS — assumed angular whirl amplitude of coupling (degrees). This is the relative angle between internal and external coupling halves of the coupling during unstable whirl. This value must be assumed and it is expected to be slightly larger than the angle defined by half the face width and the radial clearance.

$$EPS \geq \tan^{-1} \left[\frac{2 \times CLEAR}{XL} \right]$$

142

OMEGA1 — first natural frequency (rpm). Unstable whirl is expected to occur at the first natural frequency. OMEGA1 must be estimated and input to allow correct calculation of equivalent viscous damping coefficients.

DELTAO — assumed radial whirl amplitude (inches). This is the relative radial amplitude between internal and external spline members expected during unstable whirl. This assumed value is expected to be incrementally larger than the radial clearance.

Card 3   (8E10.3)

   XMU — coefficient of friction. This value may vary from approximately 0.05 to 0.25, depending on the type of lubrication and the relative sliding velocity.

   TORQ — transmitted torque (in.-lb)

   CLEAR — radial clearance (in.-lb)

   G — shear modulus (lb/sq in.)

   S — space width (in.)   These are described in
                                        ANSI B92.1 1970, the stan-
   T — tooth thickness (in.)   dard referred to earlier.

Card 4   (8E10.3)

All values on this card, except for the fillet radii, may be taken from ANSI B92.1 1970 and are shown schematically in figure B-2.

       D — pitch diameter (in.)
     DRE — minor diameter, external (in.)
     DFE — form diameter, external (in.)
   RFIL1 — fillet radius, external (in.)
     DRI — major diameter, internal (in.)
     DFI — form diameter, internal (in.)
   RFIL2 — fillet radius, internal (in.)

Figure B-3 shows a coding sheet which describes the location of each input quantity in the card deck.
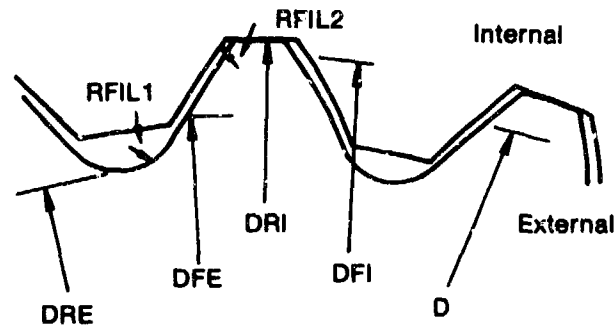
3.0 OUTPUT DESCRIPTION

Page 1 — Complete list of input parameters

      a.   Radial stiffness, angular stiffness, radial damping, angular damping

      b.   Contracted stiffness matrix

$$\left.\begin{array}{c}\\ \\ \\ \\ \\ \\ \end{array}\right\} \ (2\text{-}26)$$

      c.   Contracted damping matrix

      d.   Expanded stiffness matrix (2-28)

      e.   Expanded damping matrix (2-29)

Figures B-4 and B-5 contain flow charts of the main program and the spline coupling subroutine.

A. Major Diameter Fit

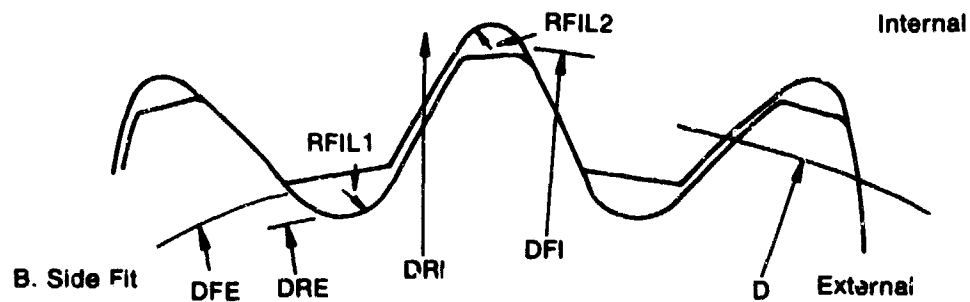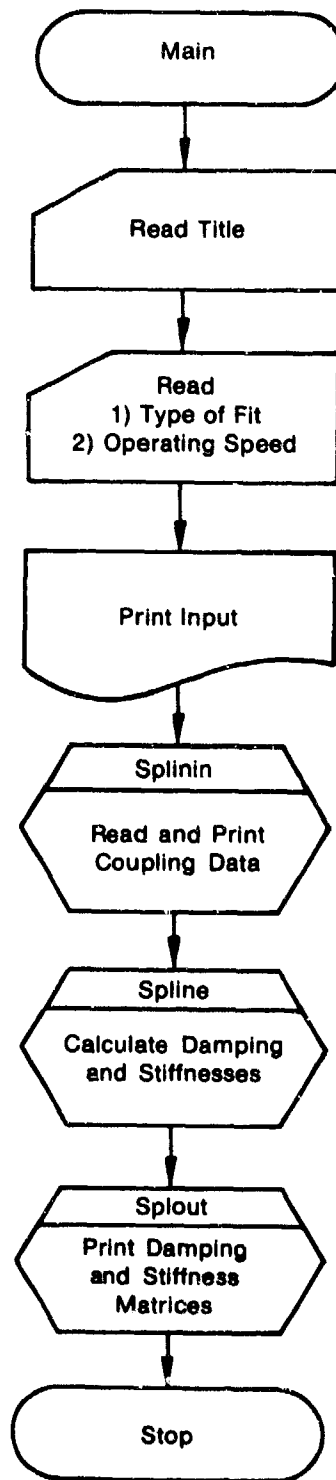B. Side Fit

Figure B-2. Input Values of Card 4

Program Title _____   Spline (Main, Splinin)

Program	Card								
Main	1			Title Card (8A10)					
			Title (i) i = 1.8 →						
Main	2	IFIT		Type of FIT (1615)					
Main	3	Speed		Operating Speed (8E10.3)					
Splinin	1	NT	NK1	NK2	Integer Controls (1615)				
Splinin	2	PSI	XL	EMOD	XNU	WC	EPS	Omega 1	Delta 0
				Coupling Data (8E10.3)					
Splinin	3	XM11	TORO	Clear	G	S	T		
Splinin	4	D	DRE	DGE	RFIL 1	DRI	DFI	RFI 12	

Figure B-3. Spline Program Coding Sheet
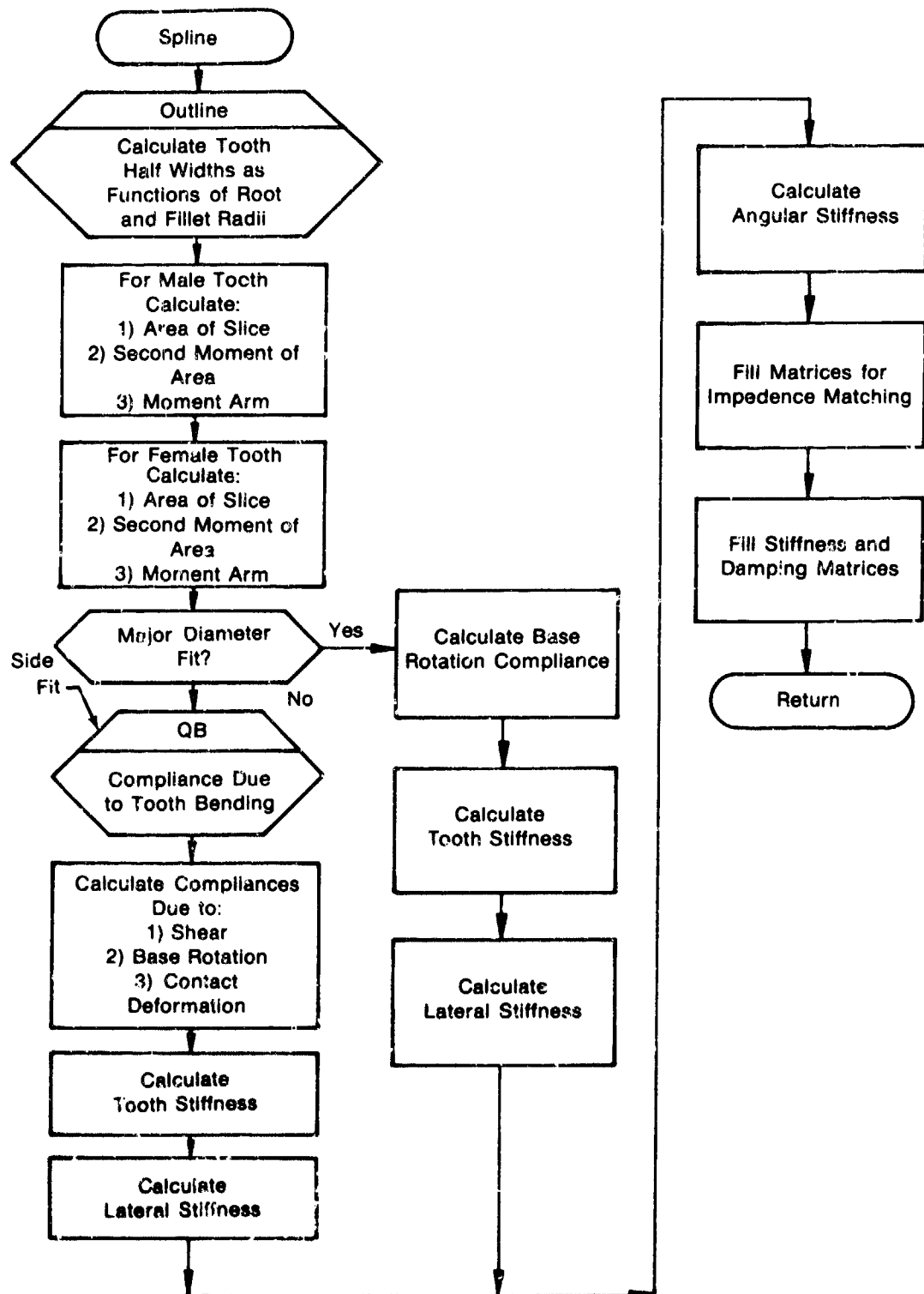
Figure B-4. Flow Chart of Main Program

146

Figure B-5. Flow Chart of Spline Subroutine

4.0 EXAMPLE CASES

Example cases have been run for one of each coupling type — major diameter fit and side fit. Table B-1 lists the input quantities for each of the two cases; the results for the example are given in table B-2.

Table B-1. Input Data for Two Example Cases

	Data For Major Diameter Fit Coupling	Data For Side Fit Coupling
Operating Speed (rpm)	4900	4900
No. of Tooth Pairs	36	36
No. of Segments, Ext.	10	10
No. of Segments, Int.	10	10
Pressure Angle (deg)	30	30
Face Width (in.)	1.75	1.75
Young's Modulus (lb/sq in.)	30×10^6	30×10^6
Poisson's Ratio	0.3	0.3
Contact Patch Width (in.)	0.1	0.1
Angle of Tilt (deg)	0.1025	0.3448
First Critical (rpm)	2400	2400
Radial Amplitude (in.)	1.552×10^{-3}	5.252×10^{-3}
Coefficient of Friction	0.15	0.15
Torque (in.-lb)	2000	2000
Radial Clearance (in.)	1.55×10^{-3}	5.25×10^{-3}
Shear Modulus (lb/sq in.)	11.58×10^6	11.58×10^{-6}
Space Width (in.)	0.1344	0.1344
Tooth Thickness (ext) (in.)	0.1258	0.1239
Pitch Dia. (in.)	3.0	3.0
Minor Dia. (ext) (in.)	2.871	2.83
Form Dia. (ext) (in.)	2.910	2.91
Fillet Radius (ext) (in.)	0.040	0.040
Major Dia. (int) (in.)	3.084	3.170
Form Dia. (int) (in.)	3.009	3.090
Fillet Radius (int) (in.)	0.040	0.040

Table B-2. Results for Two Example Cases

	Major Diameter Fit Output	Side Fit Output
Radial Stiffness (lb/in.)	1.2978×10^6	1.3181×10^6
Angular Stiffness (in. lb/radian)	3.2970×10^6	3.3119×10^7
Radial Damping (lb-sec/in.)	417.52	123.47
Angular Damping (in. lb-sec/radian)	156.58	47.143

148